FORSCHUNGSZENTRUM KARLSRUHE
Technik und Umwelt

Wissenschaftliche Berichte
FZKA 6396

THE WATER CHERENKOV DETECTOR IN THE AUGER EXPERIMENT

Performance of a Prototype Detector and the Cross-calibration of the Energy Determination by the Akeno Giant Air Shower Array and the Haverah Park Experiment

Thomas J. Kutter

Institut für Kernphysik

Forschungszentrum Karlsruhe GmbH, Karlsruhe
1999

Abstract

An array of 1600 water Cherenkov detectors (WCDs) will form the backbone of the Pierre Auger Observatory whose goal is to investigate the nature and origin of cosmic rays with primary energies above 10^{19} eV. The detection of extensive air showers (EAS) by means of Cherenkov light produced in water filled tanks is a technique established by the Haverah Park array for characterizing cosmic ray air showers and their primaries. The setup and operation of two water Cherenkov detectors (WCDs) within the Akeno Giant Air Shower Array (AGASA), a more conventional scintillator array is described. This work permits comparison of the two techniques and facilitates a study of detector characteristics in response to individual muons as well as EAS. Muon data are used to verify detector simulations which in turn serve as a tool to investigate the capacity of WCDs to accurately measure air shower parameters such as energy and muon content. These parameters in turn serve to characterize cosmic ray primaries. Based on a set of EAS, observed by the prototype WCDs and AGASA, an energy cross-calibration between AGASA and the Haverah Park experiment is performed. For primary cosmic ray energies in the range $10^{18.0}$ – $10^{18.6}$ eV, agreement to within 15% is found.

DIE WASSER CHERENKOV DETEKTOREN IM AUGER EXPERIMENT

Zusammenfassung

Eine regelmäßige Anordnung (Array) von 1600 Wasser Cherenkov Detektoren (WCD) wird das Rückgrat des Pierre Auger Observatoriums bilden, das den Nachweis kosmischer Strahlung im Energiebereich oberhalb von 10^{19} eV zum Ziel hat. Der Nachweis von bodennahen Teilchen ausgedehnter Luftschauer durch Cherenkov Licht, welches im Inneren von WCD erzeugt wird, erlaubt die zugehörige kosmische Primärstrahlung zu charakterisieren. Der Aufbau und Betrieb zweier WCD innerhalb des Akeno Giant Air Shower Arrays (AGASA) wird beschrieben und ermöglicht das Detektorverhalten sowohl in Antwort auf einzelne Myonen als auch auf ausgedehnte Luftschauer, zu studieren. Experimentelle Myonendaten dienen zur Überprüfung von Simulationen, welche dann wiederum als Hilfsmittel eingesetzt werden, um die Leistungsfähigkeit der WCD hinsichtlich einer genauen Bestimmung von Teilchenschauerparametern wie z.B. der Primärenergie und des Myonenanteils, zu untersuchen. Basierend auf einem Satz von Teilchenschauern, die von den Prototyp-Detektoren und AGASA in Koinzidenz beobachtet wurden, wird eine Energieeichung zwischen letzterem und dem Haverah Park Experiment, einem ehemaligen Wasser Cherenkov Detektor-Array, durchgeführt. Für Primärenergien im Bereich von $10^{18.0}$ – $10^{18.6}$ eV wurde eine 15 prozentige Übereinstimmung in den Energiemessungen gefunden.

Contents

Chapter 1

Introduction

Cosmic rays, a flux of charged and neutral particles, extend over an energy range of 10 orders of magnitude up to the highest observed per particle energies of a few times 10^{20} eV [1, 2]. In the early days of cosmic ray physics in the first half of this century much of the interest in cosmic rays stemmed from their utility as a means to study particle physics. The cosmic radiation and its secondary component, created in Earth's atmosphere in form of extensive air showers (EAS), were the principal source of elementary particles. Cosmic rays lead to the discovery of a number of theoretically postulated particles. In 1932, Anderson discovered the positron [3] and in 1937 Anderson and Neddermeyer identified the muon as a constituent of the secondary cosmic radiation [4]. In 1947, the pion was also first seen in the cosmic radiation by Occialini and Powell [5]. Despite the fact that the cosmic ray flux still bears information about elementary particle physics in domains which are inaccessible by any terrestrial accelerator, the advent of particle accelerators caused the main interest of cosmic ray physics to shift towards their astrophysical aspects. Major attention is now focused on issues concerning the origin of cosmic rays, acceleration mechanisms, cosmic ray propagation and resulting interactions with background radiation fields and the interstellar medium. The fundamental change in cosmic ray physics consists of directing the principal interest away from the secondary radiation, and directing it towards the primary radiation itself.

By means of direct and indirect measurements, that is above and below the atmosphere, cosmic rays have been explored in the energy range 10^9 – 10^{20} eV. The spectrum known to date is shown in figure 1.1, which displays the flux versus particle energy. The flux can be described by a simple power law with spectral index of ~ 2.7 up to energies of 10^{15} eV. At energies between 10^{15} and 10^{16} eV the spectrum steepens, a feature commonly referred to as knee, and then extends to about 10^{18} eV with a spectral index of ~ 3.2 [7]. At energies around 10^{19} eV a flattening of the

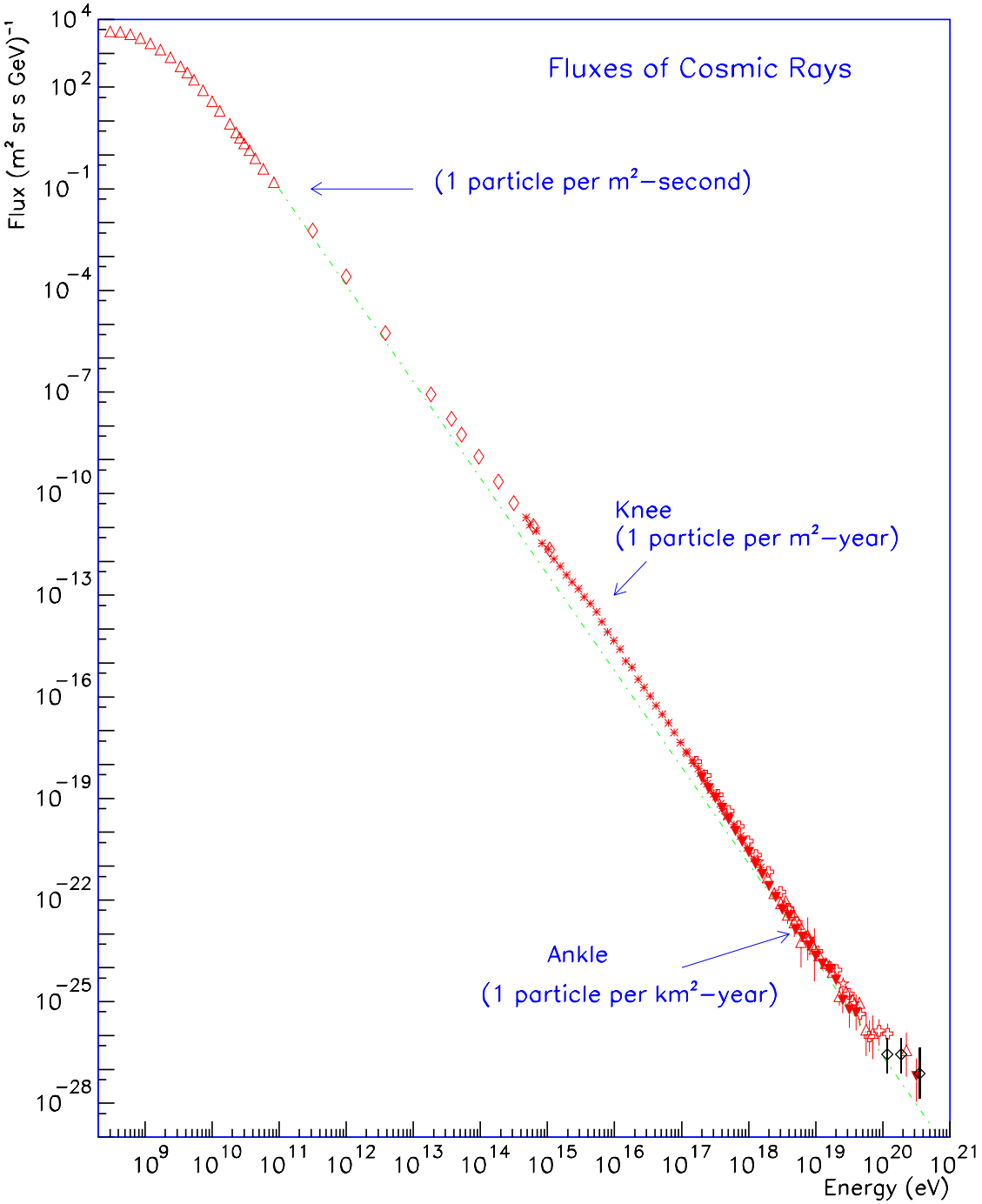

Figure 1.1: *Differential energy spectrum of cosmic rays as measured by various experiments ranging from satellite based observatories to ground based experiments. Indicated fluxes are per steradian. [6]*

spectrum ("ankle") can be observed and the slope is described by a spectral index of ~ 2.8 [8]. At the high energy end of the spectrum the cosmic ray flux amounts to about one particle per km^2 per century and as a consequence only 13 events with energies above 10^{20} eV have been observed since 1963, when Linsley observed the first 10^{20} eV event at Volcano Ranch in New Mexico [7, 8, 9, 10, 11, 12, 13]. The mere existence of these highest energy events represents a mystery because the cosmic microwave background (CMBR), detected in 1965 by Penzias and Wilson [14], was predicted to make the universe opaque to cosmic rays with energies exceeding the threshold for photo-pion production. Greisen [15] and independently Zatsepin and Kuz'min [16] pointed out that due to the interaction between cosmic rays and the CMBR the cosmic ray spectrum should exhibit a cutoff ("GZK-cutoff") at energies around 5×10^{19} eV unless cosmic rays originate from within a distance smaller than the attenuation length in the CMBR of ~ 50 Megaparsec. Particles with energies above 5×10^{19} eV have large magnetic rigidities and as a consequence deviations in galactic and extragalactic magnetic fields are thought to be negligible. If so, the arrival directions of these most energetic cosmic rays point back to their origin. However, to date, the statistics of events above 5×10^{19} eV is very limited and no sources have been identified!

Upcoming experiments such as the "Pierre Auger Observatories" [6, 17] and the high resolution Fly's Eye detector (HiRes) [18, 19] in collaboration with the Telescope Array (TA) [20, 21] intend to shed light on this unexplored domain of particle astronomy. The Auger Observatories will use a hybrid detection technique based on two detector components, a surface array and a fluorescence detector, to observe the entire sky. The surface array will consist of 1600 water Cherenkov detectors per observatory site. They detect secondary particles arriving at ground level by means of Cherenkov light created by the particles' passage through clear water contained inside the detector units. This detector component which operates at a duty cycle of 100%, forms the backbone of each observatory; it is complemented by a set of fluorescence telescopes which detect the nitrogen fluorescence light created along the shower trajectory.

The work in hand describes the setup and the operation of two water Cherenkov prototypes installed within the Akeno Giant Air Shower Array (AGASA) in Japan [22, 23], currently the largest operating array for the detection of extremely high energy cosmic rays (EHECRs). The goal of this work is to demonstrate WCD performance in response to individual muons and to extensive air showers. The latter are identified by AGASA whose signal is used to trigger the prototype detectors upon arrival of extensive air showers. Apart from the water Cherenkov detector research & development for the Auger Project, this work aims to relate the cosmic ray spectra as measured by AGASA, a conventional scintillator array and the Haverah

Park experiment [24, 25, 26]. The latter was a surface detector array composed of water Cherenkov detectors (WCDs) similar in design to the Auger prototype detectors. This similarity is reason why the observations made at AGASA may be closely related to results obtained from EAS measurements by the Haverah Park air shower array. Because of the strong link between the Haverah Park experiment and the prototype detectors on the one hand and the simultaneous observation of air showers by AGASA and the water Cherenkov prototype detectors on the other, the present data sample will be used to compare the primary energy estimates of the AGASA and Haverah Park air shower arrays. The goal is to examine the relative agreement between these independent air shower energy estimates and to discuss the results in the context of the primary energy spectra as published by the AGASA and Haverah Park groups. An accurate determination of primary energy and resulting cosmic ray spectrum is crucial to the understanding of cosmic rays, as spectral features may contain information about origin, e.g., galactic versus extragalactic, source distributions and acceleration mechanisms of cosmic rays.

The method presented permits identification of systematic biases in either of these experiments. Described in detail is how individual water Cherenkov detectors are used, in combination with parameterized results from the Haverah Park array, to perform the cross-calibration. Particular attention is paid to corrections which are necessary due to differences in the atmospheric height of the two arrays' locations. Furthermore, potential sources of error originating from the fact that only individual water Cherenkov signal density measurements are made, are considered.

These results should increase confidence in the measured cosmic ray spectra as well as aid in comparison of results from surface detector experiments which use these detector technologies.

Chapter 2

Astrophysics of the Highest Energy Cosmic Radiation

2.1 Potential sources of extremely high energy cosmic rays

The generally accepted view about the sources of cosmic rays is that they are active cosmological objects. This includes supernovae and their remnants, pulsars, active galactic nuclei (AGNs), quasars, radio- and Seyfert galaxies as well as x-ray binaries. Within our galaxy supernovae, pulsars and neutron stars and the nucleus of our galaxy, possibly a black hole, are potential candidates. Some of these objects, such as the crab nebula (pulsar) [27, 28, 29, 30] and the binary AE Aquarii [31, 32, 33], have been positively identified as strong gamma-ray emitters.
Extragalactic objects contained within the local super cluster are radio galaxies, N-galaxies and quasars. All these objects can be characterized by their active galactic nucleus. The nuclei are in a position to free large amounts of continuous radiation and high energy particles and are considered to be the principal source of cosmic radiation. The emission itself is not necessarily limited to the nuclei themselves and, particularly in the case of radio galaxies, can occur from "hot spots" at the exteriors of those galaxies. An example of an extragalactic source is the BL Lac object Mrk 421 (active galaxy) [34, 35]. At the high energy end of the spectrum knowledge about potential sources is much less certain due to a lack of data and severe constraints on source distances and acceleration regions which rule out most conventional astrophysical accelerators.
For the very highest energy cosmic rays there are three fundamentally different theoretical source models:

1) gradual acceleration in large objects (e.g., radio galaxies)

2) acceleration in catastrophic events (e.g., γ-ray bursts)

3) more exotic sources (e.g., topological defects, monopoles)

Gradual or statistical acceleration is characteristic of a slow energy accumulation process over a wide range of energies which allows for the natural creation of a power law spectrum. The prototype of statistical acceleration is the "Fermi acceleration" [36] which is associated with strong shock waves in plasma embedded magnetic fields which function as containment for charged particles and prevent them from immediate escape of the acceleration region. Upon a particle's encounter with the shock wave the average energy change ΔE per encounter is positive and amounts to $\Delta E = \alpha E$, where α indicates the fraction of the particle's initial energy. After k encounters with the shock front, the particle's energy is, on average, $E = E_0(1+\alpha)^k$, where E_0 is the initial particle energy. In the limit of strong shocks the spectral index γ of the energy spectrum is of the order of $\gamma \sim 1$. The observed spectrum is expected to be steeper than that at production due to energy dependent processes during transport to Earth. The experimentally observed integral spectrum varies between $E^{-1.1}$ and $E^{-2.1}$ in various energy regimes. Fermi acceleration produces a spectral index which conforms with observation and with assumptions about the propagation of cosmic rays. The maximum particle energy $E_{\rm max}$ is determined by the length of time over which particles of charge Z are able to interact with the plasma shock front. For example, in the case of super novae shock fronts the accelerating region itself exists for only a limited time and dissipates after about 1000 years. If the accelerating regions themselves exist for a much longer time, then the magnetic rigidity of the accelerated particles becomes the limiting factor to the maximum energy. This is the case for the highest energy cosmic rays and is expressed in the following equation:

$$E_{max} \approx \beta c \cdot Z \cdot e \cdot B \cdot L \cdot \epsilon_{\rm eff}\,, \tag{2.1}$$

where L is the size of the acceleration region, βc the shock velocity (≈ 0.01 for SN), B the magnetic field strength and $\epsilon_{\rm eff}$ (~ 0.1) the efficiency factor of the acceleration mechanism. Equation 2.1 essentially states that a particle's gyro radius $r_G = m \cdot \beta c / Z \cdot e \cdot B$ needs to be contained within the acceleration region L in order for the particle to experience further acceleration. The condition that particles with energies of the order of 10^{20} eV be confined by magnetic fields B to the size of the accelerating region L imposes strong constraints on potential physical sources of the highest energy cosmic rays. Figure 2.1 displays various astrophysical objects and possible sites of particle acceleration as function of their size and magnetic field strength [37]. Objects below the diagonal lines cannot accelerate particles to

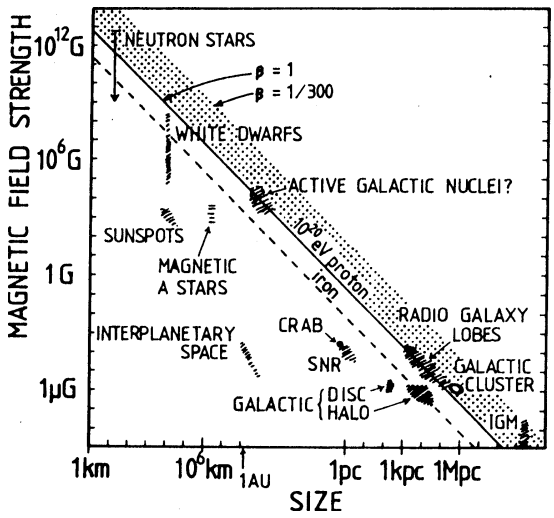

Figure 2.1: *Size and magnetic field strength of possible sites of particle acceleration [37]. Objects below the diagonal lines cannot accelerate particles to 10^{20} eV by shock acceleration. The dashed line is for iron nuclei, solid for protons, each with β=1. The top of the shaded region is for protons and β=1/300. IGM refers to the intergalactic medium; Galactic Cluster refers to accretion shocks in clusters.*

10^{20} eV by shock acceleration. The dashed and solid lines are for iron nuclei and protons, each with $\beta = 1$, respectively. The top of the shaded region is for protons and $\beta = 1/300$. IGM refers to the intergalactic medium; Galactic Cluster refers to accretion shocks in clusters. Figure 2.1 reveals that any cosmic ray observatory which aims to identify astrophysical sources of cosmic rays with energies above 10^{20} eV requires good energy resolution and high sensitivity to the mass of the cosmic ray primary. Furthermore, from potential sources fulfilling the B-L criterion it can be concluded that the most likely sources of the highest energy cosmic rays are extragalactic and associated with large scale structure. A large number of theoretical papers describes the acceleration of cosmic rays within large scale astrophysical structures such as

i) large scale structure formation [38]

ii) shocks in accretion flows in clusters of galaxies [39]

iii) collision of galaxies [40]

iv) shocks in lobes at the ends of high speed jets in powerful radio galaxies [41].

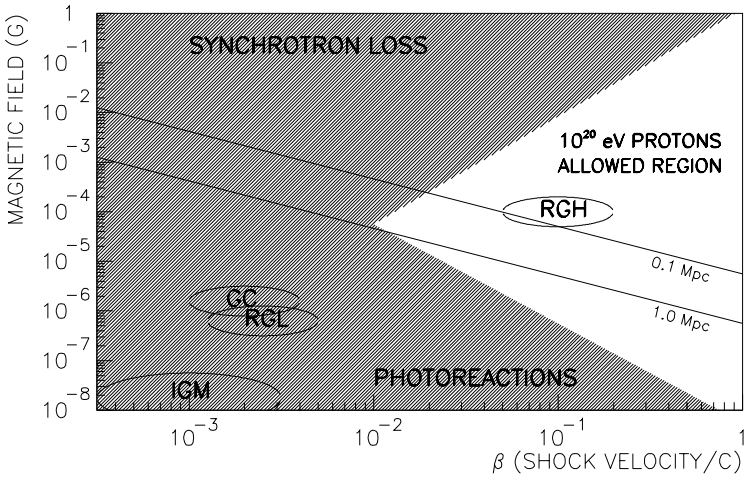

Figure 2.2: *Magnetic field strength and shock velocity of possible sites of acceleration ([37, 53]). GC is Galactic Cluster, RGL is Radio Galaxy Lobes and RGH represents hot-spots in radio-lobes. See text for further explanations.*

Potential sources are often associated with compact volumes of intense thermal radiation near the core region and with strong magnetic fields. These photon fields are the cause of an energy degradation of accelerated particles. The responsible interaction processes are synchrotron radiation in strong magnetic fields, the production of e^+/e^--pairs in background radiation fields and, more importantly, photoproduction interactions (e.g., $p\gamma \rightarrow \pi^+ n$). The particle acceleration ceases when the energy loss rate exceeds the energy gained through shock encounters. This condition further reduces the number of potential sources for the highest energy cosmic rays as certain combinations of shock velocity and magnetic field strength can prevent the acceleration process from achieving energies as high as 10^{20} eV. An estimate of this effect is given in figure 2.2 which shows magnetic field strength and shock velocities of potential acceleration sites. This estimation was based on an energy gain from shock acceleration and energy losses from synchrotron radiation and photoreactions on the CMBR [37, 53]. Candidate accelerators must lie above lines appropriate to their size and in the unshaded region in order to accelerate protons to 10^{20} eV. More intense radiation fields, e.g., near the core of AGNs, would cause even more severe energy losses.

Although some theoretical models may be further constrained by observational data at lower energies, that is, by the corresponding gamma-ray and neutrino fluxes, the lack of data at the high energy end of the spectrum leaves, at this time, too much

room for speculation. However, some hints on source identity exist: Correlations of two very energetic events (a 3×10^{20} eV event from Fly's Eye, and the 2×10^{20} eV from AGASA) with general locations of probably nearby FR-II galaxies were found in recent work [42]. The likelihood of a random association of the event directions with these type of objects is small because of the small number of FR-II galaxies within small distances. For cosmic rays with energies above 4×10^{19} eV some evidence of a directional clustering along the super-galactic plane has been found [43, 44, 45].

Conditions for acceleration in catastrophic events or so called "one-shot" acceleration mechanisms are given in gamma-ray bursts (GRB) [46, 47] or compact objects with very large magnetic and electric fields such as neutron stars or active galactic nuclei (AGNs) [48]. In the latter case a single traversal by a charged particle of a reconnection surface, associated with the twisted flux surfaces can lead to particle energies well above presently observed energies. However, energy loss processes in the vicinity of compact objects are likely to degrade the particles' energies significantly. Due to intense radiation fields accelerated protons and nuclei will loose energy by photo-pion production and photo-disintegration processes respectively. In particular in the vicinity of neutron stars curvature radiation further contributes to the energy degradation.

GRBs are likely to be indicators of catastrophic events during which cosmic ray particles could be shock-accelerated to extreme energies. It is interesting that the power needed to account for the energy flux of the highest energy cosmic rays is comparable to the average power (over volume and time) emitted by GRBs in the form of gamma-rays. The arrival directions of the most energetic Fly's Eye event mentioned earlier is, within error bars, consistent with that of one of the strongest bursts detected by BATSE [49]. The AGASA event of 2×10^{20} eV is within 5° of another strong GRB.

Among the more exotic source models are decaying X particles with GUT scale masses on the order of 10^{24} eV. These X particles may be radiated from topological defects (TDs) formed during phase transitions as the early universe cooled. They are a product of spontaneous symmetry breaking implicit in some Grand Unified Theories (see [50] for a detailed overview). It is assumed that the X particle itself produces jets of hadrons and photons with energies well above 10^{20} eV which then cascade down to lower energies.

The resulting spectra are expected to be considerably harder than acceleration spectra and therefore TD mechanisms could be the dominant contribution to the flux of cosmic rays above $\sim 10^{20}$ eV. The flux of cosmic rays above 10^{20} eV would be dominated by gamma-rays and protons; the latter comprise only a few percent of the total flux. In principle TD models can be discriminated by the gamma-ray flux

below 10^{14} eV and a substantial neutrino flux above 10^{18} eV. The fact that the predicted and observed spectral shapes are similar speaks in favor of TD models; in particular the observed "gap" in the differential CR energy spectrum around $5{\times}10^{19}$ eV is reproduced by TD scenarios. Acceleration models cannot account for this spectral feature.

2.2 The propagation of cosmic rays and the GZK-cutoff

As cosmic rays travel through space they are subject to various interactions and their trajectories may be curved by magnetic fields. Both interactions and magnetic deflections are energy dependent and cause an alteration of the initial energy spectrum and the arrival directions at Earth. If particle energies are sufficiently large, magnetic deflections are limited and the measured arrival directions of cosmic rays on Earth point back to their sources. Deflections will depend on the magnetic field strength, the distance traveled and the particle's energy and charge. The Larmor radius in kiloparsecs for a particle of charge Ze in a magnetic field B (in μG) is

$$R_{kpc} \approx \frac{E_0}{10^{18}} \cdot \frac{1}{ZB} \quad . \tag{2.2}$$

Since galactic magnetic fields are of the order of a few μG and the thickness of the disc is less than 1 kpc a clustering of 10^{19} eV cosmic ray arrival directions along the galactic plane is expected if sources can be associated with luminous matter. At present, no clustering of cosmic ray arrival directions along the galactic plane has been observed. This can be regarded as an argument in favor of cosmic rays with E$> 10^{19}$ eV being of extragalactic origin.
A recent publication [54] pointed out that the currently observed isotropical arrival direction distribution of cosmic rays with energies above 10^{20} eV favors more exotic sources located in the halo of our galaxy over conventional accelerating sources.
If cosmic rays are of extragalactic origin they must have survived a long time in order to reach Earth. Several processes can degrade the particle's energy while propagating through the cosmos. The most important of these processes is photo-pion production on the cosmic microwave background (CMBR) via the Δ^+-resonance according to $p\gamma \rightarrow \Delta^+ \rightarrow \pi^0 p$. If the proton energy is above 10^{20} eV the characteristic attenuation length is about 50 Mpc. A similar phenomenon of energy degradation also occurs for nuclei due to photodisintegration. The interaction with the CMBR has important consequences:

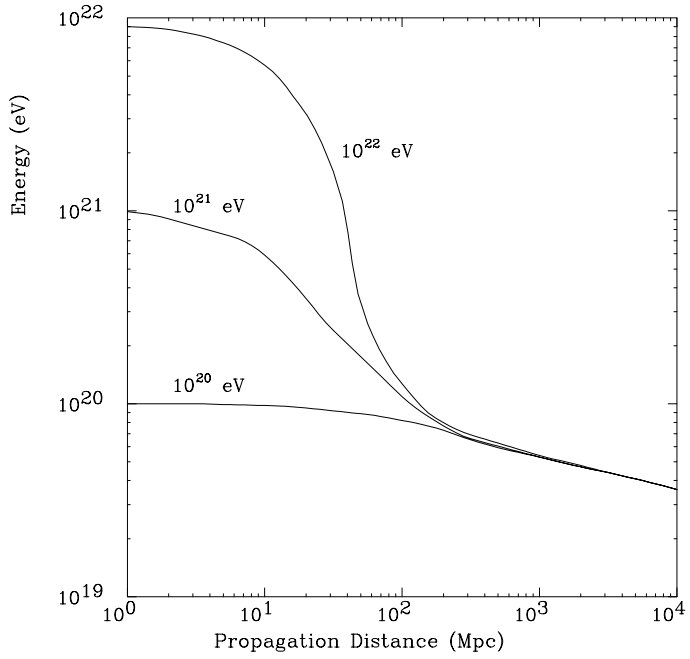

Figure 2.3: *Energy of a proton as a function of propagation distance through the 2.7 K cosmic background radiation for various initial energies [51, 52]*

1) If the highest energy cosmic rays are cosmological in origin, the observed energy spectrum should not extend beyond energies of about 5×10^{19} eV. This important phenomenon was first pointed out by Greisen [15] and independently by Zatsepin and Kuzmin [16] and is called the Greisen-Zatsepin-Kuzmin (GZK) cut-off.

2) Particles with energies above the GZK cut-off must come from nearby (≤ 100 Mpc) and hence show only little deviation due to magnetic fields. Their observed arrival directions point back to their origin and should help identify their sources, either known astrophysical objects invisible at lower energies or new sources.

Other energy loss processes are the production of electron-positron pairs in the background radiation, synchrotron losses in regions of extreme magnetic fields and the energy loss due to the general expansion of the universe over time. The interaction processes of EHECR with various background radiation fields impose limits on the maximum distance these extremely energetic particles almost independently of their initial energy. This phenomenon is shown in figure 2.3, which shows the energy degradation of protons due to photopion interactions as function of propagated

distance through the CMBR for three different initial energies [51, 52]. It is evident that the proton flux above 10^{20} eV is sharply reduced after a propagation length of about 100 Mpc.
The attenuation length of protons and nuclei in the CMBR depends strongly on energy. Features in the observable spectrum are therefore a combination of the initial spectral shape and characteristics introduced by the propagation of cosmic rays in the CMBR. As a result, the distribution of sources in time and space will have strong impact on the shape of the observable cosmic ray spectrum.

Chapter 3

Cosmic Ray Air Showers and Cascade Physics in the Atmosphere of the Earth

In 1938 Pierre Auger and his colleagues discovered the phenomenon of particle showers in the atmosphere of the Earth. By means of coincidence experiments with 3 or 4 partly lead-covered and separated scintillation counters they concluded that the particles they observed were of secondary nature. The point of origin of these secondary particles was estimated to be high up in the atmosphere [55, 56]. Furthermore, from the secondary particles' energies, as measured by the penetration of lead, and the particle number derived from their experimentally determined ground level density, Auger estimated the total energy of the most energetic showers observed, and consequently the primary particle giving birth to them, to be in the range 10^{12} – 10^{13} eV [57]. This is a very remarkable conclusion as these energies were several orders of magnitude beyond the highest per particle energy known to exist at the time.

Auger and his colleagues classified the secondary particles into two categories: a penetrating and an ultra-penetrating component, made out of electrons and a class of particles described as heavy electrons. Nowadays, it is known that the secondary particles, created in the interaction of a cosmic ray entering Earth's atmosphere and an nucleus of an air molecule, are of hadronic and electromagnetic nature. Depending on the identity of the primary cosmic ray, charged and neutral pions, muons, electron-positron pairs, and γ-quanta are created. These secondary particles, whose relative and absolute number depends on the nature and energy of the primary cosmic ray, interact themselves with the atmosphere and hence create a propagating particle cascade. Generally, a particle cascade in Earth's atmosphere, also known

as air shower, has a hadronic and an electromagnetic component. The occurring interaction processes and their strength depend strongly on type and energy of the cosmic particle. However, independent of the detailed characteristics of the primary, an air shower which is subject to fluctuations will be formed. Therefore any individual cascade can be atypical.

3.1 Electromagnetic cascades

Electromagnetic particle cascades can originate from high energy γ-quanta, electrons or positrons. The dominant interaction, in the case of a photon as seed particle, is the electron-positron pair creation in the vicinity of an atomic nucleus X:

$$\gamma + \mathrm{X} \rightarrow e^+ + e^- + \mathrm{X}.$$

The conversion length λ_{Ph} of high energy photons in air amounts to $\lambda_{\mathrm{Ph}} \approx 48\ g/cm^2$ and is mainly determined by this process. Contributions from the decay channels into a μ^+/μ^--pair and photo production are smaller than 3 parts per thousand and hence negligible. The created electron-positron pairs further contribute to the development of the cascade. The relevant process is the creation of bremsstrahlung, produced by acceleration of charged leptons in the field of a nucleus X.

$$e^\pm + \mathrm{X} \rightarrow e^\pm + \gamma + \mathrm{X}$$

The radiation length χ_0 (defined as the mean free path length) of electrons for this process amounts to about 37 g/cm^2 in air. The energy loss of the electrons occurring during this interaction process is proportional to their initial energy.
Only when the electron energy has decreased to below 84 MeV, the *critical energy* in air, do energy losses through ionization processes become dominant. The critical energy E_{crit} is defined as the energy for which the energy losses of an electron are caused in equal parts by ionization and bremsstrahlung. Ultimately, the ionization processes will cause the shower to die out since this process doesn't produce any high energy quanta. The maximum shower development occurs when the energy of a majority of electrons has decreased to the critical energy and the number of particles has reached its maximum value. The maximum particle number of an electromagnetic cascade depends on the energy of the primary γ-quantum.

3.2 Hadron induced particle cascades

Direct measurements of cosmic rays up to energies of 10^{15} eV, the "knee" of the cosmic ray energy spectrum, indicate a 50% proton content. The other portion is made up of α-particles ($\sim$25%) and heavier nuclei up to iron. At higher cosmic ray energies, where no direct measurements exist due to the low flux, the primary cosmic ray composition is unclear.
The following explanations will be tailored for protons but can easily be attributed to heavier nuclei after fragmentation. In contrast to the electromagnetic cascades, the hadron induced particle showers are less well understood. The reason is the multitude of competing processes and, at the highest energies well beyond man-made accelerator regimes, the unknown cross-sections for particle interactions. A proton entering the atmosphere and interacting with an air nucleus produces various particles such as mesons and hyperons as well as particle-antiparticle pairs. Equation 3.1 indicates potential interaction products which have various decay channels themselves.

$$\mathrm{p} + X \rightarrow \pi^0, \quad \pi^{\pm}, \quad (\mathrm{p} + \overline{\mathrm{p}}), \quad (\mathrm{n} + \overline{\mathrm{n}}), \quad \underbrace{K + \Lambda + \cdots}_{\pi^{\pm}, \pi^0, \ldots} \tag{3.1}$$

Created π^0s decay quasi instantaneously ($\tau \approx 10^{-16}$s) into two γ-quanta and hence give birth to electromagnetic sub-cascades.

$$\pi^0 \rightarrow \gamma + \gamma \ .$$

Charged π-mesons have longer lifetimes resulting in the possibility that they may collide with a nucleus and create an interaction analogous to the one represented in equation 3.1. In particular first generation charged pions have such high Lorentz factors that their decay is suppressed and they practically all make nuclear interactions. The hadronic cascade proceeds until the charged pion energy is degraded to the point ($\sim$ 20 GeV) that decay to muons and corresponding neutrinos is more probable than further interaction.

$$\pi^{\pm} + \mathrm{X} \rightarrow \text{see} \quad (3.1)$$

$$\pi^+ \rightarrow \mu^+ + \nu_\mu \, ,$$

$$\pi^- \rightarrow \mu^- + \overline{\nu}_\mu \, .$$

Muons have a small cross section and relatively long lifetimes of $\tau = 2 \times 10^{-6}$ s; as a result of the time dilatation the majority of muons reach ground level. A few, mostly low energy, muons won't reach ground level and decay according to

$$\mu^+ \rightarrow e^+ + \nu_e + \overline{\nu}_\mu \, ,$$

$$\mu^- \rightarrow e^- + \overline{\nu}_e + \nu_\mu \,,$$

into electrons, positron and corresponding neutrinos. All other particles mentioned in equation 3.1 and not specified any further decay quickly by the strong interaction, mainly into pions and muons.
At each generation of shower particles about one third of the energy is transferred into an electromagnetic cascade due to the prompt decay of π^0. As a consequence of charged and neutral pion decay the predominant shower particles at the surface of the Earth are electrons/positrons, γ-quanta and muons, with the electromagnetic component outnumbering the muons. Ultimately, the electromagnetic cascade dissipates roughly 95% of the primary particle's energy through ionization. Therefore, the number of low energy electromagnetic particles is nearly proportional to the shower energy; the remaining energy is carried by muons and neutrinos from charged pion decay. Simulations indicate that for a 10^{19} eV proton-initiated shower 96% of the primary energy goes into the electron-photon cascade and only 2.4% and 0.8% go into muons and neutrinos, respectively. A small remaining energy is contained in the hadronic component at sea level [58]. The total muon number grows more slowly with primary energy than the number of electromagnetic particles mainly because of the suppressed charged pion decay at higher energies and the longer sustained hadronic cascade with a resulting transferral of energy into electromagnetic showering. Simulation [59] (chapter 17) and experimental results [60] indicate that the number of muons reaching ground level N_μ grows with energy as

$$N_\mu \propto E^{0.85} \,.$$

This is an important effect which can be used to distinguish air showers from heavy nuclei from those of protons or light nuclei.
A nucleus-initiated air shower can be modeled as a superposition of its A constituent protons and neutrons, each with energy E/A. The number of ground level muons N_μ^A of an air shower initiated by a nucleus of mass A can be expressed as

$$N_\mu^{\mathrm{A}} \propto A \left(\frac{E}{A}\right)^{0.85} \,.$$

In comparison with the number of muons of a proton shower N_μ^p the number of ground level muons N_μ^A of a nucleus shower is

$$N_\mu^{\mathrm{A}} = A^{0.15} N_\mu^p.$$

An iron-initiated shower will have about 80% more muons than a proton shower with the same initial energy. Any ground based detector sensitive to the muonic component of an air shower should therefore be able to differentiate between light and heavy cosmic rays.

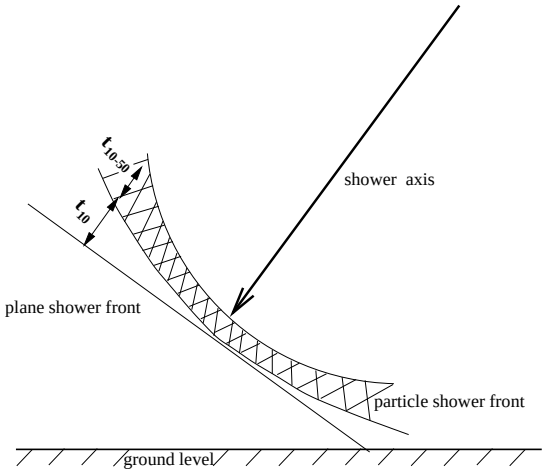

Figure 3.1: *Schematic view of an air shower traveling through Earth's atmosphere.*

3.3 Spatial structure of an air shower

An air shower can be visualized as a broad and thin disc of particles moving at the speed of light through the atmosphere. The shower direction coincides with the extension of the primary particles' trajectory around which the shower develops with nearly rotational symmetry and is described by the *shower axis*. The plane perpendicular to the shower axis and tangent to the disc of particles at the shower core is referred to as *shower plane*. The actual disc of shower particles, the *shower front*, is slightly curved and its thickness varies with distance from the shower axis. Figure 3.1 shows a schematic picture of an air shower indicating these parameters.

3.3.1 The longitudinal shower profile

The longitudinal shower profile describes the number of shower particles produced as function of atmospheric depth. Figure 3.2 displays the longitudinal profile of the Fly's Eye 3×10^{20} eV event, the largest cosmic ray air shower ever recorded. Fluorescence light, mainly produced by electromagnetic particles through excitation of atmospheric nitrogen along their track, is an excellent means to observe the longitudinal shower development. The intensity of the emitted light per particle is weak but due to the large amount of particles the net effect can be observed with suitable detectors. A shower with a primary energy of 10^{20} eV can build up to $\sim10^{11}$ particles. In a simplified model the emission of fluorescence light could be described

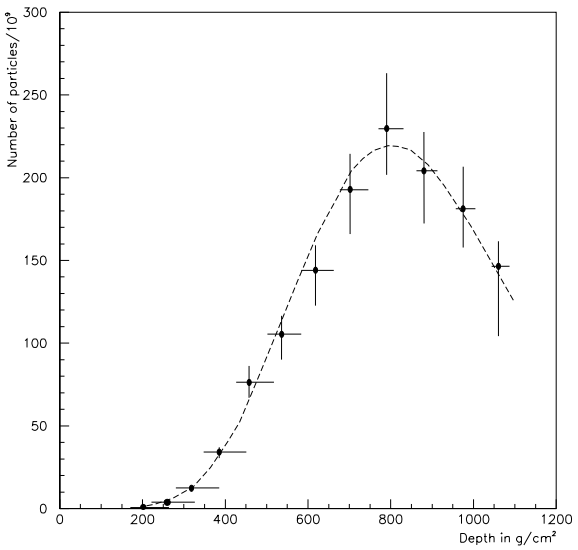

Figure 3.2: *Longitudinal shower profile for a 3×10^{20} eV event as recorded by the Fly's Eye detector.*

by a light spot moving along the shower axis and varying its intensity proportional to the number of particles at the corresponding atmospheric depth. Therefore, the light spot maps the longitudinal shower development from which information about the shower energy and type of primary can be extracted.
The atmospheric depth of maximum shower development is denoted $X_{\max}$ and represents an important parameter to characterize the primary cosmic ray. The shower maximum $X_{\max}$ moves deeper into the atmosphere at a rate of 50 – 70 g/cm^2 per decade in increase of primary energy E_0 [61, 58] and [6] (chapter 4). At the same total energy E_0, an air shower from a heavy nucleus is expected to develop faster than a shower initiated by a proton because heavy nuclei have larger cross sections and, more importantly, less energy per nucleon. In the representation of the *superposition model* a nucleon can be described as A individual protons where A is the number of its constituent nucleons, each of energy $E' = E_0/A$. For an iron-initiated shower $X_{\max}$ is expected to be ~ 100 g/cm^2 less than for a proton shower of same energy ($E' = E/56$). In summary, the atmospheric depth of maximum shower development is a function of primary energy and mass: $X_{\max}$=$X_{\max}(E_0, A)$; it becomes less by about 63 g/cm^2 per decade in energy decrease or per decade of increase in mass of the primary particle.
An important result of the deep $X_{\max}$ for air showers originating from light nuclei is that these showers have larger electron numbers N_e at ground level than showers initiated by heavy nuclei. The ratio of muon number and electron number

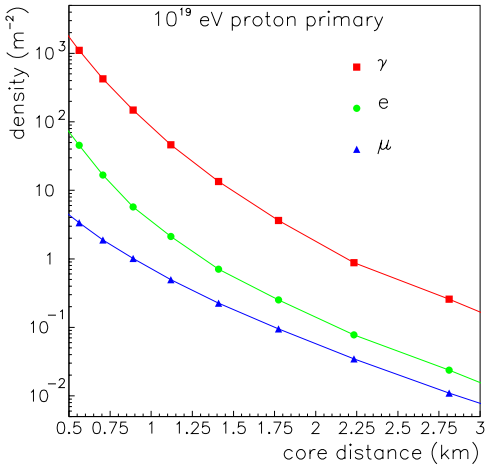

Figure 3.3: *Lateral distribution of γ-rays, electrons and muons for a simulated 10^{19} eV proton initiated shower at a zenith angle of 30°.*

$r_{\mu-e} = N_\mu/N_e$ which is smaller for lighter primaries, represents therefore an even more powerful handle on the cosmic ray composition than either parameter alone.

3.3.2 Lateral spread of shower particles at ground level

The lateral spread of particles in an air shower is caused by multiple Coulomb scattering, geomagnetic deflections and the transverse momentum in interactions and decays. Particularly for muons which interact rarely, the spread is dominated by the emission angle of the parent pion. As the angles involved are small, the particle density falls steeply with distance from the shower axis on a scale determined by the Molière radius in air which is of the order of 80 m. Experimental and simulation results collected over a wide range of energies demonstrate that the particle distribution has axial symmetry. Therefore, it is common to describe the lateral spread of particles as function of core distance in form of a lateral distribution function whose exact form depends on the type of ground array detector and the atmospheric depth at which observations are made.
Simulations indicate that at ground level more than 50% of all particles fall within the Moliere radius of 80 m from the core. Figure 3.3 shows the simulated lateral distribution for all major components of ground particles for a shower originating from a proton with primary energy 10^{19} eV at a zenith angle of 30°. Muons have a

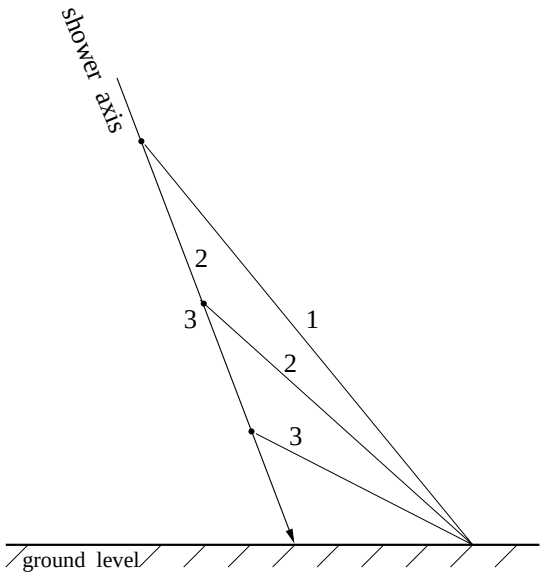

Figure 3.4: *Muon path length as function of production height in the atmosphere for a given core distance.*

much flatter lateral distribution than electromagnetic particles reflecting a relatively high production height for a large quantity of muons. At core distances larger than 500 m particle densities are low and photons dominate numerically over electrons and muons. However, beyond 500 m the energy flux is dominated by muons as the per particle energy for muons amounts to about 1 GeV whereas electromagnetic particles carry on average only 10 MeV.

3.3.3 The time structure of the shower front

At large core distances particles arrive at ground level spread out in time by more than 1 μs and delayed with respect to the shower plane. The time delays are directly determined by the path length of the particle if the particle velocity $v \approx c$ and only very little deflection occurs. This is generally true for the majority of muons. Figure 3.4 demonstrates the geometry of a number of path lengths; e.g., path 3 being larger than path 2 and path 1. Those particles distant from the shower core arriving at the ground first originate higher and thus earlier in the cascade. The time spread created is roughly proportional to the distance from the axis and is expected to be greater as the depth of shower maximum increases. Since muons suffer less scattering than electromagnetic particles as they propagate towards the ground they tend to

arrive earlier than electrons and photons. These features can be exploited by ground array detectors with transient signal recorders as signal rise time and signal duration reveal information about the muon content and $X_{\max}$ and hence the type of primary particle of the shower. For iron-initiated showers, which are expected to develop higher in the atmosphere and produce more muons than proton showers of same energy, the signal rise time should be smaller, firstly because of the geometric effect of shorter path lengths, and secondly because of the larger muon content, both resulting in a larger amount of early arriving particles.

3.4 Fluctuations in air shower development

The height of the first interaction point, specified by its atmospheric depth X_0 inherits the most important fluctuations of an air shower. Fluctuations in later interaction processes are averaged out by the large number of particles involved after the development of a few cascade generations. Due to the strong correlation between X_0 and $X_{\max}$, the atmospheric depth of maximum shower development, fluctuations seen in $X_{\max}$ are therefore mainly inherited from fluctuations in X_0. The latter cause the entire longitudinal development curve (see figure 3.2) to shift up and down in the atmosphere and as a result the shower size at the ground also depends strongly on the height X_0 of the first interaction. Experimental signal rise time measurements of fluctuations $\sigma(X_{max})$ in the depth of maximum of showers produced by primary particles of energy greater than 1.5×10^{17} eV reveal a value for $\sigma(X_{max})$ in the range 50 to 65 g/cm^2 with a logarithmic dependence on primary energy [62].
Far from the core a shower develops more deeply in the atmosphere. This can be understood as a consequence of shower spread which only occurs after the first (few) interaction process(es) and hence the successive sub-cascade starts deeper in the atmosphere with respect to X_0, the depth of the first interaction. For a 10^{19} eV proton-initiated shower $X_{\max}$ for core particles is typically around 820 g/cm^2. At 1 km from the core the maximum tends to be broader and typically appears at an atmospheric depth of 1100 g/cm^2. Therefore, at large core distances fluctuations in the shower size at ground level are less severe than fluctuations in $X_{\max}$ [66]. This is an important characteristic of air showers and is taken advantage of in the energy determination of cosmic rays by surface detectors which use signal densities at core distances of typically 600 m as an estimation of shower energy.
Apart from fluctuations in the depth of the first interaction, which will have consequences for the shower energy estimation, fluctuations in the relative number of charged to neutral pions in the first few generations of the cascade need to be considered. The fluctuations in type of created particles directly affect the rate

of development of electromagnetic cascades and the muon content of the shower which in turn represent a composition-sensitive parameter. Air shower simulations for showers of energies above 10^{19} eV show fluctuations in the ground level muon component of $\sim$15% and $\sim$5% for the electromagnetic component [63, 64]. A water Cherenkov detector which records equal contributions from muons and electromagnetic particles sees effective signal fluctuations of $\sim$10%. However, this fluctuation is controlled by Poisson statistics as the number of detected particles is small [65]. Note that muon number N_μ and electron number N_e are expected to increase for heavy and light nuclei, respectively. (The increase in N_e is a direct consequence of the fact that air showers initiated by light nuclei reach their maximum deeper in the atmosphere.) As a consequence larger absolute fluctuations are introduced for these numbers and, thus, are expected to be different for light and heavy primary particles. Only detailed Monte Carlo studies will be able to characterize these kind of differences in fluctuations accurately.

Chapter 4

The Pierre Auger Project

4.1 Observational requirements for an extremely high energy cosmic ray detector

The cosmic ray spectrum falls steeply towards higher energies (cf. figure 1.1). At energies above 10^{20} eV the cosmic ray flux amounts to only one particle per km^2 per century. Therefore it is crucial for an experiment which aims to investigate the nature of these most energetic cosmic rays to have a large collecting power. An appropriate aperture (area $\times$ solid angle) for such an EHECR detector should at least be of the order of 10,000 km^2 sr. This size of aperture will allow the collection of on the order of 100 events with energies above 10^{20} eV within a time of 5 years. The expected number of events was derived for a flux estimate based on the differential flux of the Fly's Eye experiment [12] with a spectral index of 2.71. A large number of events is required to accurately determine the cosmic ray spectrum beyond 10^{19} eV and identify possible features. The existence or non-existence of the GZK-cutoff needs to be well established as important conclusions about the cosmic ray source distribution will be directly drawn here from.
Furthermore, a detailed measurement of the spectrum requires good energy resolution. The steeply falling spectrum can be distorted significantly by measurement uncertainties. There will always be more mismeasured low energy events per bin than mismeasured high energy events. This effect leads to an artificial flattening of the spectrum and easily distorts structures possibly prevailing in the original spectrum. Numerical calculations suggest that an experimental energy resolution $\delta E/E \leq 20\%$ should be sufficient to observe a GZK-cutoff. Furthermore, changes in the power law slope as small as 0.2 or features greater than about 30% of the baseline power law should be discernable with such an energy resolution ([6], sec-

tion 5.2.5).
Closely coupled to the energy resolution of an EHECR detector is its ability to distinguish between different types of primary cosmic rays. In general, the longitudinal profile of an air shower as well as the ratio of muonic to electromagnetic ground particles is used to identify the primary particle type. The more accurate the energy of an air shower is known—usually derived from its longitudinal profile and the ground particle density at a given distance—the better the results of classification into groups of primary type will be. As the particle type gives important clues about conditions at the source region as well as the acceleration mechanism itself a particle identification especially for those primaries arriving with energies above the expected GZK-cutoff is very important.
The information about extremely high energetic cosmic ray primaries is inferred indirectly from measurements of air showers. Due to the statistical nature of the processes creating an air shower all information about the primary contains inherent uncertainties independent of the detection apparatus. Bearing this in mind even a perfect detector would not be able to confidently determine the type of a cosmic ray primary on an event by event basis. Therefore, the goal of any EHECR detector is to distinguish between major groups of potential primaries. These groups are

i) primordial nuclei (p, He)

ii) products of stellar nucleosynthesis (carbon and heavier nuclei)

iii) photons (expected in the framework of exotic sources).

An important tool for the determination of the primary composition are model calculations of air showers which can be used for comparison. These models are subject to uncertainties themselves as the first few interactions in an air shower occur at unexplored energy regimes. However, the relative differences between different primary species are not strongly model dependent.
The last but not least basic requirement for an EHECR detector is the capability to search for arrival direction anisotropies. A sensitive search for anisotropies or clustering of arrival directions demands a complete sky coverage with fairly uniform and large celestial exposure. It is therefore essential to have two observatory sites, one in the Northern and one in the Southern Hemisphere.
Anisotropy studies depend on the particular energy range of interest. At energies above 10^{20} eV magnetic deflection of protons by Galactic or extragalactic magnetic fields is expected to be small so that detector angular resolution becomes an issue. At lower energies Galactic—and, should the occasion arise, extragalactic—magnetic fields will cause significant angular deviations so that point sources are smeared out.

In the case of neutral particles detector resolution is always important.
The expected angular deflection for 10^{20} eV protons within the Galaxy is estimated to be of the order of 0.3° ([6] fig. 2.9). However, extragalactic deflections are likely to exceed the Galactic deflection. The average total angular deviation from the line of sight to the source can be approximated as $\Delta\Theta \approx \sqrt{L}\Delta\Theta_{\text{cohlen}}$, where L is the source distance in units of coherence lengths and $\Delta\Theta_{\text{cohlen}}$ is the mean angular deviation over one coherence length. For a coherence length of 1 Mpc and a source distance limited by pion photoproduction to 50 Mpc an arrival direction dispersion of $\Delta\Theta \approx \sqrt{50} \cdot 0.3° \approx 2.1°$ is expected. The detector angular resolution must therefore at least be better than 2°.

4.2 The surface detector array

A surface detector array is an arrangement of individual, equally spaced detector units. Each of these detector units samples the shower front as it hits the ground — the particle density is measured along with the arrival time of the signal relative to the other detector stations. The relative arrival times of the recorded signals are used to find the orientation of the shower front in space and thus determine the arrival direction of the primary cosmic ray. Once the orientation of the shower axis, which is the prolongation of the primary particle's trajectory, is known, the density measurements can be represented in a plane perpendicular to the trajectory, the shower plane. This representation is used to find the impact position of the shower core, the central part of the shower associated with the highest particle density. The core is reconstructed under the assumption of circular symmetry in the shower plane. The procedure of finding the core will ultimately lead to a lateral distribution of ground particles or water Cherenkov signal density and can be parameterized by a function, the so called lateral distribution function (LDF). An LDF is characteristic for showers of particular energy and a particular observation level and expresses the signal size as function of distance from the shower core. It was pointed out by Hillas [76] that for a set of air showers initiated by cosmic rays with the same characteristics the density fluctuations within a distance range from 600 m to 1000 m from the core are almost independent of $X_{\max}$, the atmospheric depth of the shower maximum. $X_{\max}$ is correlated with X_0 the atmospheric depth of the first interaction, which again depends strongly on the energy of the primary. This fact makes the density at core distances in the range from 600 m to 1000 m an ideal energy estimator of the primary particle. Uncertainties of energy estimation done according to the described method can originate from inaccuracies in the determination of the LDF,

statistical fluctuations in the shower development and a model based normalization constant. Simulation results for such a set of showers show that the fluctuations of $X_{\max}$ amount to ~ 50 g/cm^2 in case of proton primaries with an energy of $1{\times}10^{19}$ eV and entering the atmosphere at a zenith angle of 30°.
The size of the array and its spacing are determined by cost efficiency considerations and the requirement of being fully efficient for showers with energies around 10^{19}eV and above. The total area covered by detectors is proportional to the exposure of the experiment and ought to be maximized to account for the low flux of EHECRs. A large coverage of area at the least cost can only be attained with widely spaced detector units. The reference design for the Auger Observatory quotes a triangular grid with 1.5 km spacing as adequate to fulfill the observational needs and meet the above requirements. With 1600 detector stations per observatory site an area of $\sim$ 3000 km^2 will be covered. In any event, as a consequence of this design, no more than one detector will be closer than 750 m from the shower core. Therefore, the shower characteristics at large core distances are of importance for the design of the individual detector units and the selection of its materials and components.
The shower properties described here are deduced from air shower simulations. The results have been compared with existing experiments and good agreement was found for the properties of the ground particles. These properties are the energy of the shower particles and their spread in arrival time. The effect of various interaction models on these ground particle characteristics is not significant. Far from the core the shower front consists essentially of gamma ray photons, electrons, positrons and muons. These particles are accompanied by a large number of Cherenkov photons and a flux of generally sub-relativistic neutrons delayed with respect to the main shower front. The flux of relativistic hadrons is negligible at core distances beyond 50 m.
At a core distance of 1.1 km the mean energy of the electromagnetic component is $\sim$ 10 MeV while the mean muon energy amounts to $\sim$ 1 GeV. Figure 4.1, which shows the ground particle spectra at a core distance of 1.1 km, demonstrates this property. Further out from the core the energy of the muonic component decreases to about 600 MeV at 2 km whereas the energy of the electromagnetic component remains unchanged. The second relevant property of ground particles far from the shower core is their spread in arrival times. At a distance of 1.1 km the spread amounts to $\sim 2\,\mu$s and grows to $\sim 4\,\mu$s at core distances around 2 km. Figure 4.2 shows the integrated arrival times of electromagnetic and muonic ground particles at a core distance of 1.1 km. Muons arrive earlier and spread out less in time than the electromagnetic component. Both of these shower particle properties are independent of the energy and type of the primary particle.

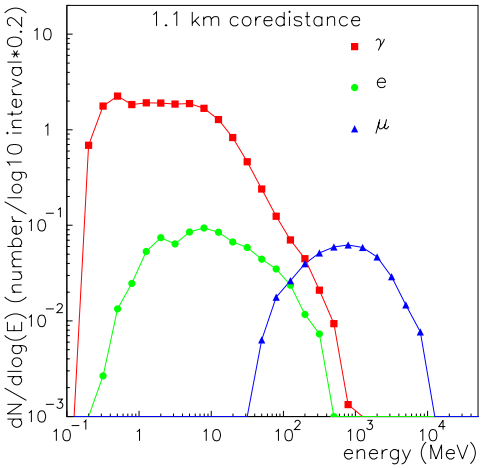

Figure 4.1: *Ground particle spectra at 1.1 km from the shower core.*

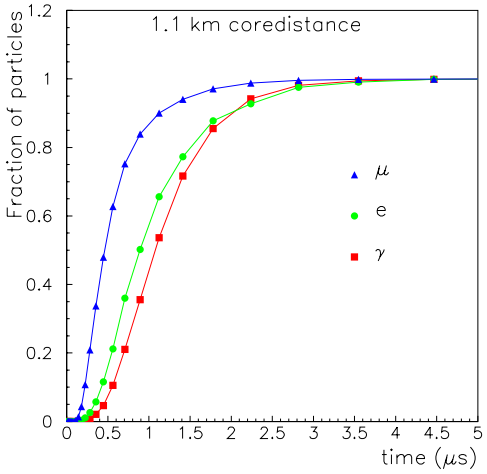

Figure 4.2: *Integral arrival times of ground particles.*

4.2.1 Key design parameters for a water Cherenkov detector

The individual detector units of the Auger Observatory ground array were chosen to be 1.2 m deep water Cherenkov detectors. This type of detector consists of a volume of clear water acting as a Cherenkov radiator viewed by 3 photomultiplier tubes (PMTs). At the same time the water acts as a massive absorber and converter for the numerous gamma rays.
A cylindrical detector shape with a top surface area of 10 m^2 corresponding to a radius of 1.8 m, was proposed and causes the detector to respond uniformly with respect to the azimuthal arrival direction of an air shower. The dimensions of the detector volume were chosen in analogy to the detector units of the Haverah Park (HP) experiment, an array of 1.2 m deep water Cherenkov detectors which was operated in the United Kingdom over a period of 20 years. Existing data and results from the HP experiment are thus very useful for comparison and consistency checks. (A detailed description of the Haverah Park Experiment is given in appendix A). The PMTs are placed at 120° intervals on a circle of radius 1.2 m and will have a photocathode measuring $\sim$ 200 mm in diameter; on the one hand maximizing the ratio of photosensitive area to tank wall area is desired as it causes an increase in the number of collected photoelectrons and thus sensitivity, but on the other it will also lead to an increase in cost. In order to maximize the sensitivity of the detector

for a given photocathode area, the inside of the water tanks will be lined with a highly reflective and diffusive white material such as Tyvek.
With water as detection medium the individual stations are sensitive to all the components of the shower. Gamma rays produce relativistic electrons by Compton scattering and pair production processes. Cherenkov light is released by relativistic electrons produced, as well as the electrons that enter the tank directly. Muons can be detected by the amount of Cherenkov light they release as they pass through the water. As a consequence of higher per particle energies, air shower muons travel further in water than electrons and a large fraction of muons will penetrate the tank losing ∼250 MeV which is only a fraction of their mean energy. The 1.2 m deep water volume corresponds to 3.5 radiation lengths and is therefore sufficient to absorb more than 90% of the incident, and by far more numerous electromagnetic shower particles (cf. figure 4.1). However, for a calorimetric detector, such as a deep water tank the energy carried by the entering shower particles is important, not their number. Cherenkov light is only produced by fully relativistic and therefore sufficiently energetic particles; electromagnetic particles however do not exceed the energy threshold for Cherenkov-light production over the entire length of their track within the water. – Figure 4.3 displays the energy flux of shower particles as function of core distance. The dominant role of muons and gamma rays is apparent. Due to the fact that at large core distances the mean per particle energy of the electromagnetic shower component is much smaller than the mean per particle energy of muons a deep water Cherenkov detector is relatively more sensitive to muons than electromagnetic particles. This effect is reflected in the lateral distribution of Cherenkov light produced in 1.2 m deep water Cherenkov detectors which is shown in figure 4.4. At core distances beyond 1.5 km the contributions from muons and electromagnetic particles to the amount of recorded Cherenkov light are nearly equal. Furthermore, at large core distances where the number of particles in the shower front is low and the time spread between the particles is relatively large, muons should be discernible from electromagnetic particles by their signal characteristics. For a good proportionality of detector response, that is when the signal of each particle is closely proportional to the amount of Cherenkov light released, muons are expected to produce more pronounced peaks in a time resolved signal trace. On the basis of a pulse height and arrival time analysis it should then be possible to determine the fraction of the signal that originates from muons. The muon fraction of ground particles is of interest because of the close connection between the muon content of an air shower and the mass of the primary. As described in chapter 3, iron initiated showers have significantly more muons than proton induced showers of the same primary energy. From simulations it is expected that for iron induced showers the density of muonic ground particles at core distances

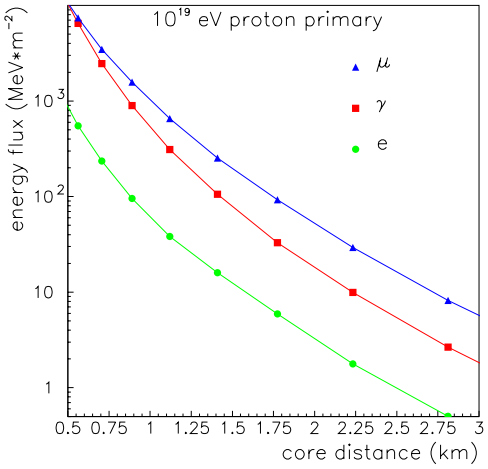

Figure 4.3: *Lateral distribution of energy flux.*

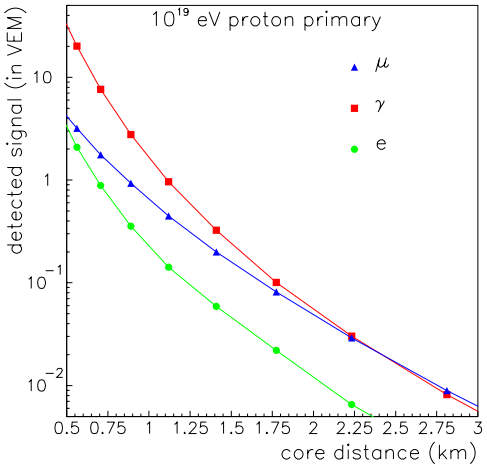

Figure 4.4: *Lateral distribution of signal in units of vertical equivalent muons (VEM) expected in 1.2 m deep water Cherenkov detectors.*

beyond 1 km is more than 75% higher than for an equi energetic proton shower. The densities of the electromagnetic particles are expected to be similar. The enhanced muon sensitivity of deep water Cherenkov detectors makes this kind of detector an ideal analysis tool for composition studies. The composition sensitive parameters extractable from water Cherenkov data are exclusively based on the muon component of an air shower. These parameters are the ratio of muonic to electromagnetic water Cherenkov signal, the signal rise time t_{10-50} and the shower front curvature. The latter can be expressed as a time parameter t_{10} in form of a delay to a plane shower front. The time based parameters are strongly coupled to the muonic component of the shower front because of the early and compressed arrival of muons. Figure 3.1 illustrates the composition sensitive time parameters.

4.2.2 Air shower reconstruction from surface detector data

In this section the extraction of relevant air shower information from ground array data is illustrated. Along with the principal method detailed parameterizations and heuristical constants from the Haverah Park air shower array (cf. appendix A.1) will be used as an example.

The geometrical reconstruction of the air shower, that is the determination of the shower axis and its core location at the ground can be done by simple triangulation if three or more ground stations record data. The position of the shower axis is located by exploiting circular symmetry of particle density in the shower plane. As a first estimate the position of the shower core can be approximated by the "center of gravity" of the density measurements. In a second step the fitting of an empirical LDF will reveal the most probable core impact position an the shower size being sought. Once the core impact position has been determined the recorded detector arrival times need to be re-fitted allowing for curvature of the shower front. This process allows to refine the shower direction and is repeated several times (≤ 3) until convergence is attained. For the technique to successfully characterize the shower the LDF needs to be known with great accuracy. An accurate experimental parameterization expressing the mean LDF in the distance range 50 < r < 700 m was derived from HP data for $2{\cdot}10^{17}$eV < E < $4{\cdot}10^{18}$eV and $\theta < 45°$:

$$\rho(r) = N \cdot r^{-(\eta + \frac{r}{r_0})}, \tag{4.1}$$

where N is a normalization constant $r_0 = 4000$ m, independent of zenith angle and η varies with zenith angle θ and energy E according to

$$\eta = 2.2 - 1.29 \cdot (sec\,\theta - 1) + 0.165 \cdot log\left(\frac{E}{10^{17eV}}\right). \tag{4.2}$$

An extrapolation of the parameterizations to the energy regime E $\geq 10^{19}$eV and core distances up to 800 m seems to be valid. For core distances r > 800 m a correction term was added:

$$\rho(r) = N \cdot \left(\frac{1}{800}\right)^{\beta} \cdot r^{-(\eta + \frac{r}{r_0}) + \beta}, \tag{4.3}$$

where β was found to be 1.03 $\pm$ 0.05 [75]. Good agreement was established between data from the Haverah Park experiment, the empirical LDF and simulations. However, due to the limited statistics of the data sample this result should only be regarded as an approximation.
The relationship between an EAS size parameter such as measured by a ground array and the energy of the primary particle initiating the cascade must in general be determined via analytical or shower model calculation. Simulations first carried out by Hillas et al. [76, 66] indicated the relation

$$E = 7.04 \cdot 10^{17} eV \cdot \rho_\lambda(600)^\alpha, \tag{4.4}$$

where E is the energy of the primary particle in eV and $\alpha = 1.018$. $\rho_\lambda(600)$ is the equivalent value of $\rho(600)$, the density at a core distance of 600 m, for a shower of

equal energy arriving from the vertical direction. The Monte Carlo calculations from which this relation was derived make assumptions about interaction physics well beyond the energy range explored and studied by accelerator experiments. Nevertheless, the prediction claims to be valid and independent of the mass of the primary particle !
In order to estimate the energy of non-vertical showers the attenuation of EAS in the atmosphere must be taken into account. Based on the constant intensity method [59](chapter 16.2.2) an exponential behavior with a characteristic attenuation length λ was derived. The principal idea of this method is to compare the average size of showers that fall at the same rate in various zenith angle bins. A plot of size versus slant depth for each intensity then maps the average development curve for the primary energy that corresponds to a particular rate. Edge et al. [77] showed that ρ_{600} followed the relationship

$$\rho_\lambda(600) = \rho(600) \cdot exp\left(\frac{1018}{\lambda}(sec\,\theta - 1)\right), \tag{4.5}$$

where θ is the zenith angle of a given shower and 1018 g/cm^2 is the mean atmospheric depth of the array site. The value determined for the attenuation length λ was 760 $\pm$ 40 g/cm^2 derived from showers with zenith angles less than 60°.

4.3 The fluorescence detector

A fluorescence detector measures the longitudinal development of an air shower as the shower front sweeps through the atmosphere and produces a faint glow of fluorescence light. The particle cascade initiated by a primary cosmic ray in Earth's atmosphere dissipates much of its energy by exciting and ionizing air molecules along its path. The excited nitrogen molecules return to their ground state by emitting fluorescence light in the near UV. The emission is isotropical and produces a discrete line spectrum which is shown in figure 4.5. The intensity of the emission is proportional to the number of particles and can be expressed in terms of photons released per track length l in the form

$$\frac{dN\gamma}{dl} = N_f \cdot N_e. \tag{4.6}$$

N_e represents the number of electromagnetic particles and N_f is the fluorescent yield in photons per charged particle and meter. The latter is of the order of 4.8 and is expected to vary by less than 12% over an altitude range of about 20 km in the atmosphere [69]. Although the efficiency of the fluorescence process in the atmosphere

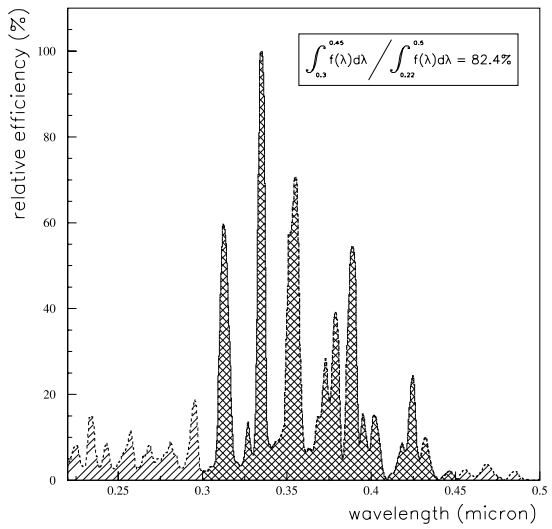

Figure 4.5: *Emission spectrum of fluorescence light from the 2P band of molecular nitrogen and the 1N band of the N_2^+ molecular ion. About 80% of the light is emitted between 300 and 450 nm [6].*

amounts to only $\sim 5{\cdot}10^{-3}$ the overall light production is substantial because of the vast number of shower particles. An estimate of the number of particles at a given atmospheric depth can be derived from the amount of observed fluorescence light if the distance to the corresponding shower segment is known. The number of shower particles as function of atmospheric depth is commonly referred to as longitudinal shower profile. The longitudinal profile of the shower yields, when integrated the energy of the primary particle and reveals X_{max} the atmospheric depth of the shower maximum. The latter being an indicator of the type of primary particle if the energy of the shower is known.

4.3.1 Key design parameters for a fluorescence telescope

A fluorescence detector consists of large light collectors which image regions of the sky onto clusters of light sensing devices. The size of the mirrors, the focal length and curvature as well as the specifications for the granularity of the camera depend on requirements for the aperture and sensitivity of the telescope. In order to maximize the number of events detected simultaneously by both, the ground array and the fluorescence detector, it is essential that the aperture of the fluorescence detector includes the entire aperture of the ground array for showers with energies above

10^{19}eV. The importance of these so called hybrid events will be discussed in the next section. Note that the fluorescence aperture depends on the energy of the shower because of the proportionality between primary energy, the number of electromagnetic particles and thus the intensity of the fluorescence light. Once the array size is determined the ground array aperture is fixed and defines the aperture required for the fluorescence detector. As for requirements on the sensitivity, a resolution of 20 g/cm^2 in the depth of shower maximum is envisaged. With this kind of resolution the analysis of primary mass composition is very promising because at any fixed energy the expected depths of maximum range over approximately 100 g/cm^2 as the primary mass varies from proton to iron. The here-from resulting constraints on the system are stringent enough to also achieve a 10% resolution in primary energy determination.
The main components of a fluorescence telescope, the mirror area and the pixel size of the camera are closely bound by the signal to noise ratio, as

$$S/N \sim (\frac{A \cdot \epsilon \cdot \Delta t}{B \cdot \Delta\Omega})^{\frac{1}{2}}, \tag{4.7}$$

where A is the collecting area of the mirror, ϵ the overall efficiency for converting photons to photoelectrons, Δt the integration time, B the overall background light and $\Delta\Omega$ the solid angle of a single photomultiplier tube. The uniformity of camera sensitivity and cost arguments plead for large photomultiplier tube sizes. Large mirrors are used to compensate the resulting degradation of the S/N ratio. However, $\Delta\Omega$ is strictly limited to a maximum pixel size of 1.5° because larger pixel sizes would not allow a sufficiently accurate reconstruction of the shower axis geometry. The background light B depends essentially on the site chosen and and can only be reduced somewhat by the use of optical filters with a transmissivity in the range of the nitrogen fluorescence bands. With ϵ being maximized by careful selection of detector components and materials the 1.5°-sized pixels require mirrors measuring 1.5 m in diameter in order for the apparatus to provide a sufficiently large S/N-ratio, so that the resolution accuracy of 20 g/cm^2 in atmospheric depth can be fulfilled. The fluorescence telescope will make use of spherical concave $f/1$ mirrors with a hexagonal camera consisting of 121 photomultiplier tubes (PMTs) at their focus. Each PMT is read out by an integrating flash ADC which samples the signal in 100 ns time slices. Typical durations of light pulses in individual PMTs vary from 100 ns for nearby showers to ∼4 μs for distant showers with small angles relative to the line of sight. The timing and amplitude information is used for the geometric reconstruction of the shower direction. The system's trigger electronics will be designed to recognize spatial and temporal patterns of illuminated PMTs in real time. Of primary interest are close to linear patterns of hits which progress in time as these are typical signatures of real cosmic ray showers.

In order for the fluorescence detector to include the aperture of the ground array the reference design for the Auger Observatory calls for three fluorescence eyes located within the surface detector ground array. Each telescope will view 360° in azimuth and cover and elevation angle range from 2° - 30°. Each mirror unit will have a field of view of 16° x 14° so that one eye will be composed out of 45 telescopes arranged in two rings of 22 and 23 units respectively. Three eyes are preferable over one single eye with better signal to noise characteristics as showers can be observed at closer distances. This minimizes uncertain but necessary atmospheric corrections. Furthermore, for the very highest energy cosmic rays the apertures of individual eyes start to overlap so that even more redundant information of the most interesting events will be available.
Only the most fundamental design parameters, important to understand the principal functioning of a fluorescence telescope have been outlined. The actual reference design for the Auger Observatories' fluorescence detectors differs somewhat as it calls for a dual-mirror system. In this setup single telescopes are replaced by two telescopes with almost identical fields of view and larger pixel sizes. The overlapping views of the two mirrors are offset by the size of half a pixel in azimuth and declination. The angular resolution of such a system is equally good as for a single telescope with a higher granulated camera. Major advantages of the dual-mirror concept are enhanced reduction of noise triggers resulting in a better trigger efficiency and a more uniform camera sensitivity as pixel boundaries are less problematic because of the larger PMTs. The optical system chosen is a Schmidt optics design which uses a diaphragm at the mirror's center of curvature in order to eliminate coma aberrations. A detailed description of the design can be found in [70],[71], [72],[73] and [74].

4.3.2 Air shower reconstruction from fluorescence data

As in the case of a ground array the first step of shower reconstruction is the determination of the trajectory of the shower axis. The shower-detector plane (SDP) containing the trajectory of the shower and its projection onto the camera of a fluorescence detector is found by using a fit to the hit pixel directions weighted by the corresponding signal amplitudes. The orientation of the plane can be determined with an accuracy of 0.2° [67]. The orientation of the shower trajectory within the SDP is described by the impact parameter R_p and the angle of the shower axis with the horizontal χ_0. These quantities are shown in figure 4.6 along with the shower-detector plane. The parameters R_p and χ_0 may be found from the light arrival times at the individual PMTs that have been hit. This method of track reconstruction with a single telescope is called "mono" method and allows to determine the zenith

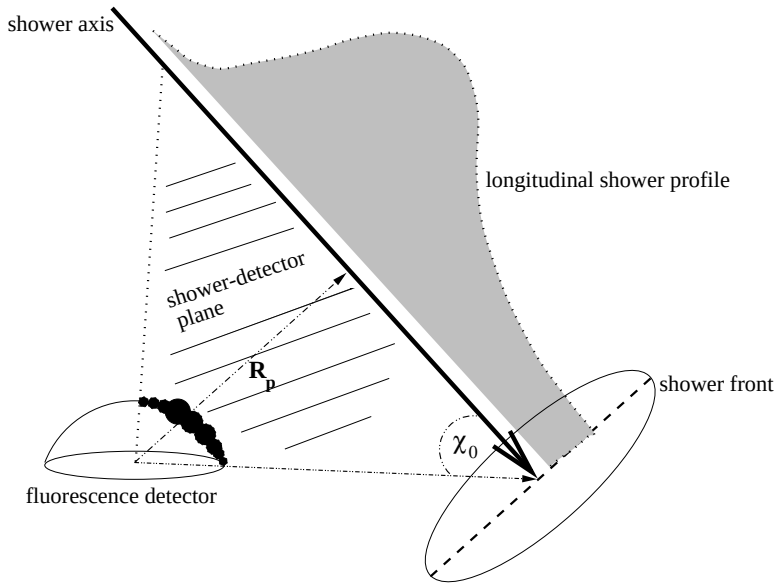

Figure 4.6: *Schematic view of the shower-detector plane geometry.*

and azimuth angle of an EAS. A disadvantage of the "mono" method is its intrinsic ambiguity which arises from the limited track length of recorded EAS. This drawback can however be compensated by using additional information from either a second fluorescence detector or a ground array.
Once the trajectory of the shower is known the PMT signal amplitudes are used to derive the shower size at a given atmospheric depth. In principle, every PMT seeing the track can make a separate estimation of the shower size. However, due to fluctuations and uncertainties for background light corrections the actual procedure applied consists of iteratively fitting a model shower shape to the data. Typically a Gaisser-Hillas [68] profile of the form

$$N_{\mathrm{e}} = N_{\mathrm{max}}(\frac{X - X_0}{X_{\mathrm{max}} - X_0})^{\frac{X_{\mathrm{max}} - X_0}{70}} \cdot exp(\frac{X_{\mathrm{max}} - X}{70}), \tag{4.8}$$

with N_{max} being the shower size at its maximum and X_0 the depth of the first interaction, is used. It is important to point out that substantial corrections for Cherenkov light as well as atmospheric attenuation have to be taken into account.
As the shower sweeps through the atmosphere a vast number of Cherenkov photons is produced. The emission angles of these photons are less than 1.38°, varying with altitude. Therefore, the Cherenkov light is highly focused and the amount detected under a certain viewing angle is not proportional to the local shower size. An estimate of its contribution, depending on the orientation of the shower axis relative to

the line of sight, needs to be subtracted in order to derive a realistic shower profile. Fluorescence and Cherenkov light are both subject to attenuation due to scattering processes in the atmosphere. In case of Cherenkov light the main concern is light scattered out of the beam to larger angles and possibly into the detector. The scatter mechanisms are twofold: 1) Rayleigh (molecular) scattering and 2) Mie (aerosol) scattering. At a given wavelength Rayleigh scattering is proportional to the column density of air through which the shower passes. The scattering length at sea level amounts to 23 km at a wavelength of 400 nm. Based on an exponential atmosphere corrections from Raleigh scattering can be calculated straight forward. The contribution from Mie scattering is much more difficult to estimate as it depends on the highly variable density and size distribution of particulate matter suspended in the air. In the absence of a mixing layer, a vertical particle distribution in form of an exponential can be assumed. Otherwise, uniform scattering is expected beneath the fixed-height mixing layer. Figure 4.7 displays the contributions of direct and scattered Cherenkov light for a simulated shower of 10^{19}eV, which approaches the detector and hits the ground 10 km from the detector. If no corrections for

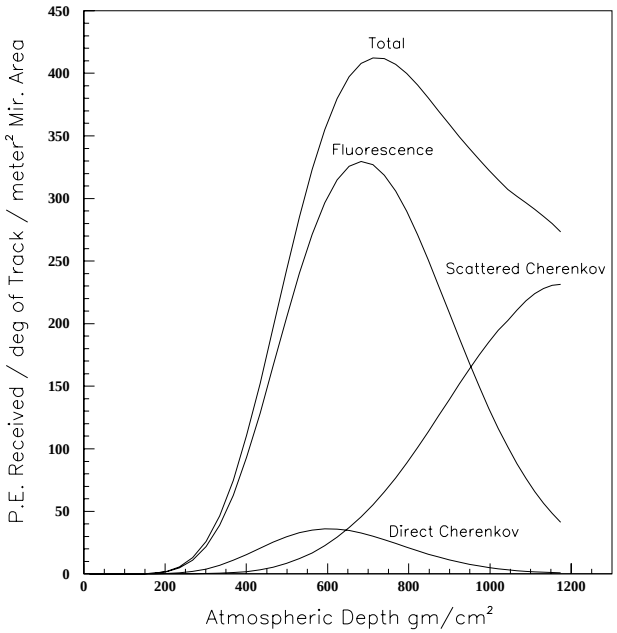

Figure 4.7: *Estimated light contributions to the signal from fluorescence, scattered and direct Cherenkov light as function of atmospheric depth. The simulation was carried out for a 10^{19} eV proton shower observed at a zenith angle of Θ=45°, an azimuth angle ϕ=0° and hitting the ground 10 km from the detector. The simulation included 300 - 400 nm band pass filters. [6]*

Cherenkov light contamination were made an error of about 30% in energy estimation and a shift of 50 g/cm^2 in $X_{\max}$ would occur in this worst case scenario.
The mentioned corrections due to Cherenkov light are of extreme importance because only a properly determined longitudinal profile yields accurate information about the shower energy and primary type. For an accurate energy estimation additional corrections are necessary due to energy dissipated into the ground in form of muons and neutrinos. This correction can however be calculated in a straight forward manner once a longitudinal model profile has been selected as a best fit to the data.

4.4 The hybrid design of the Auger Observatory

A fluorescence detector and a surface detector array are two complimentary techniques of detecting giant air showers. The fluorescence detector observes the longitudinal shower development by means of optical light whereas a ground array measures the lateral shower profile by sampling particles from the shower front at ground level. Both techniques have their strengths and pitfalls.
The shower reconstruction from mono fluorescence data is subject to ambiguities. In general a three parameter fit is used to determine the orientation of the shower axis within the surface-detector plane. The degree to which more than two parameters can be determined unambiguously depends on the degree to which the shower track image in the camera deviates from linearity. In case of short track lengths, which will be true for a large number of showers, the track is nearly linear. Therefore, it is wise to obtain additional constraints from independent measurements by either a second fluorescence detector or a ground array. In case of a hybrid detector two different fitting schemes are possible: First, the surface array can be used to determine the shower direction independently or in a second hybrid fitting scheme the arrival time of the shower front at the ground can provide additional information to allow unambiguous shower reconstruction. Not only does the ground array help the fluorescence measurement to better determine the direction of the shower but it also provides a crucial normalization for the longitudinal profile at ground level in form of a shower size measurement. This is especially important for showers measured at large distances for which atmospheric attenuation uncertainties can be significant. Since fluorescence detectors operate only during dark moonless nights about 10% of all data will be recorded in a hybrid mode.
Energy measurements by a fluorescence detector are much more direct than the energy estimation of a ground array which ultimately relies on air shower simulations. If however the final goal is to derive an energy spectrum (flux in units of $(\mathrm{m}^2 \cdot \mathrm{sr} \cdot \mathrm{s})^{-1}$),

	10^{19}eV		10^{20}eV	
	Surface	Hybrid	Surface	Hybrid
$\Delta\Theta$	2.0°	0.35°	1.0°	0.36°
Δ core	80 m	29 m	40 m	29 m
$\Delta E/E$	18%	4.2%	7%	2.5%
Δ X_{max}		17 g/cm^2		15 g/cm^2

Table 4.1: *Median errors in reconstruction of simulated proton showers at 10^{19} eV and 10^{20} eV for a surface detector alone and a hybrid detector [6](chapter 5).*

a surface detector bears the advantage of having a fixed aperture whereas the aperture of a fluorescence detector varies with energy. The hybrid technique allows to combine the more direct energy measurement of the fluorescence detector with the fixed aperture of the ground array and provides a straight forward approach in deriving an accurate energy spectrum. Table 4.1 indicates the energy resolution of a hybrid detector and a surface array alone for showers of energy 10^{19}eV and 10^{20}eV. The hybrid data set will furthermore allow to cross calibrate the surface detector with the fluorescence measurements so that even for the bulk of data recorded by the surface detector alone (90% of all data) the surface array can provide nearly model independent energy measurements !
Simulated reconstruction accuracies for proton showers of 10^{19}eV and 10^{20}eV are given in table 4.1. The arrival direction reconstruction of a hybrid detector leads to accuracies as good as the direction resolution achieved by the stereo fluorescence technique. In terms of anisotropy studies the hybrid design has nevertheless the significant advantage of providing a uniform coverage of the range in right ascension on a daily basis. Any type of fluorescence detector views only less than half of the available range in right ascension per day and requires a full year of data taking to obtain uniform coverage. A hybrid design is clearly preferable for the search of repetitive sources with unknown time scales.
The orientation and core impact position of air showers that are observed by two or more fluorescence eyes can be reconstructed unambiguously without any information from the ground array. This subsample of events will allow to study the lateral distribution of shower particles in an independent manner and will enable to derive a parameterization for the lateral distribution of these showers.
The fluorescence and surface detector technique use different and at least partially independent parameters to get a handle on the primary cosmic ray composition. The relevant parameters for the surface detector are the muonic signal fraction and arrival time parameters such as the signal rise time t_{10-50} and the shower front cur-

vature. The latter are tightly bound to the muon component of the shower front. The depth of shower maximum $X_{\max}$ is the most sensitive composition parameter for the fluorescence detector. $X_{\max}$ and the muon density are not independent parameters but they are measured with essentially independent instruments which minimizes instrumental biases. A combination of the four parameters will enhance the composition sensitivity of the hybrid detector and makes it superior to any of the techniques alone. It is important to note that an absolute composition measurement is basically impossible because of the statistical nature of the processes within an air shower. However, simulations indicate that if the energy of an air shower is accurately determined a separation into "light-like" and "heavy-like" primaries is possible. The confusion of energy uncertainty with composition represents an inherent problem and needs to be reduced to a minimum. A comparison of the data set with results from combined air shower and detector simulations for different types of primaries will reveal a model dependent composition of cosmic rays at the highest energies.

The Pierre Auger collaboration plans to build two observatories of the same hybrid design, one in the southern and one in the northern hemisphere in order to achieve full sky coverage. The southern observatory will be build in Mendoza province in Argentina and the on-site detector construction is supposed to start in January of 2000. It is foreseen to first build an "engineering array" consisting of 40 WCDs overlooked by a fluorescence detector; the principal goal of this first stage is to test the integrity of the various detector components. At a later stage the engineering array will be part of the full size observatory. The funding situation for the northern site, which was chosen to be in Millard county, Utah, USA is less clear.

Chapter 5

Water Cherenkov Prototype Detectors at AGASA

5.1 Detector description and experimental setup

Water Cherenkov detectors aim to detect air shower particles, in particular muons, at ground level by means of Cherenkov radiation created inside the detector. As air shower particles move at near relativistic speed through the atmosphere towards the ground they emit Cherenkov light upon entering a medium with refraction index larger than 1, e.g. water. This effect is used by water Cherenkov detectors which consist of a deep and preferably large volume of water viewed by photosensitive devices. The latter aim to detect faint flashes of Cherenkov light produced by relativistic particles inside the detector volume. Due to the calorimetric nature of the detector the signal size is expected to be proportional to the particle's energy.
The main detector component is a cylindrically shaped PVC bag, with radius 1.8 m and a depth of 1.2 m. The inner surface is lined with a highly diffuse reflective (reflectivity of $\approx 90\%$) Tyvek sheet. The water reservoir is surrounded by a 2.2 cm thick insulation shield and a Para-web mat to support the bag shape within a metal frame of stainless steel tubes. The tank is based on a wooden frame enabling scintillation counters to be placed beneath the tank. The PVC bag is filled with normal and un-filtered tap water which is pumped up from a depth of 250 m underground. Three Hamamatsu R1408 PMTs, mounted at a radius of 1.2 m are spaced at angles of 120°. They view the tank volume in a downwards direction from the top surface. Figure 5.1 shows a side and top view of the PVC bag and the mechanical construction. The dimensions of this detector have been chosen according to the design report of the Pierre Auger Project [6](chapter 6); simulations have demonstrated

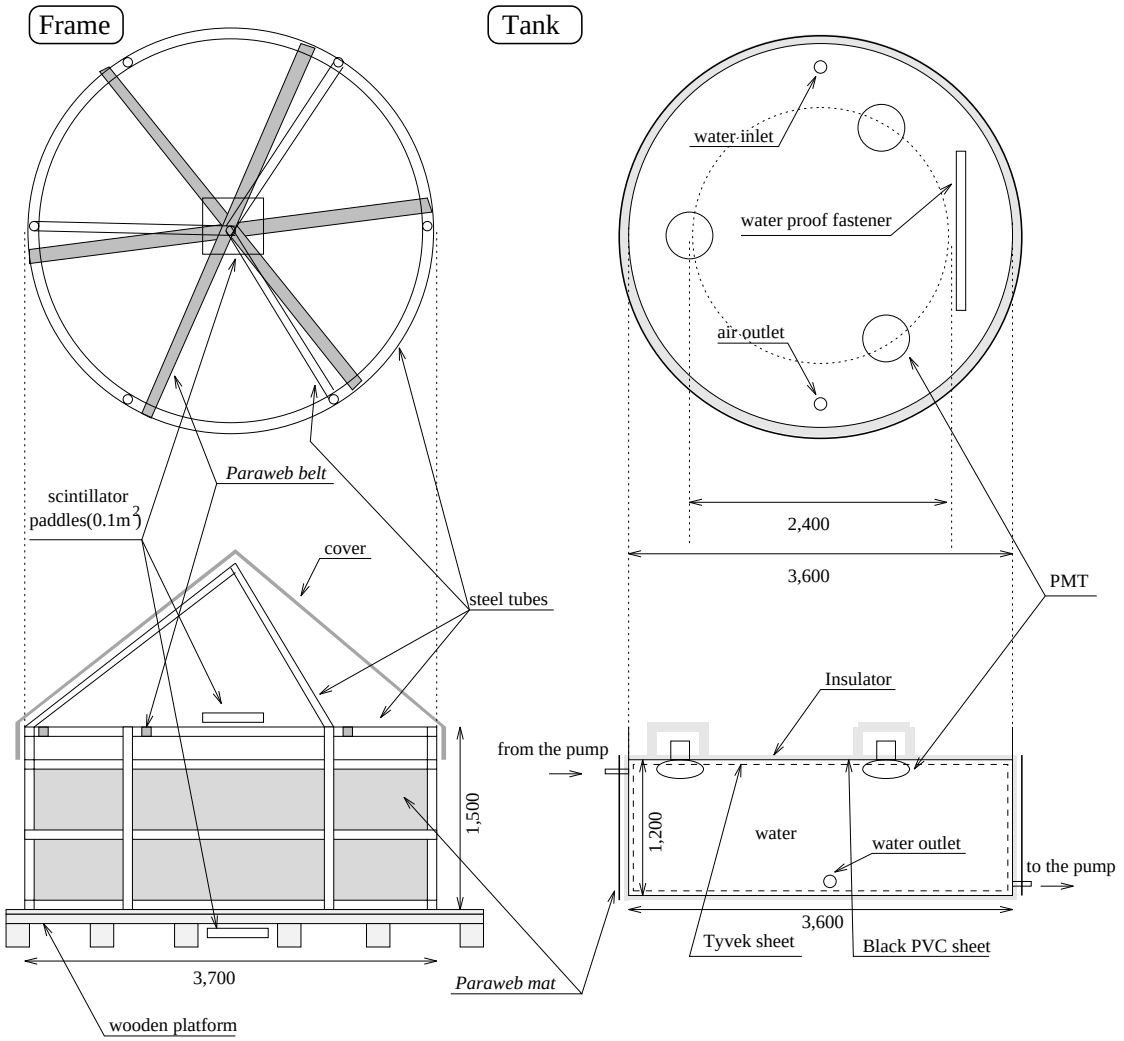

Figure 5.1: *Schematic side and top view of the first water Cherenkov prototype detector at AGASA [78].*

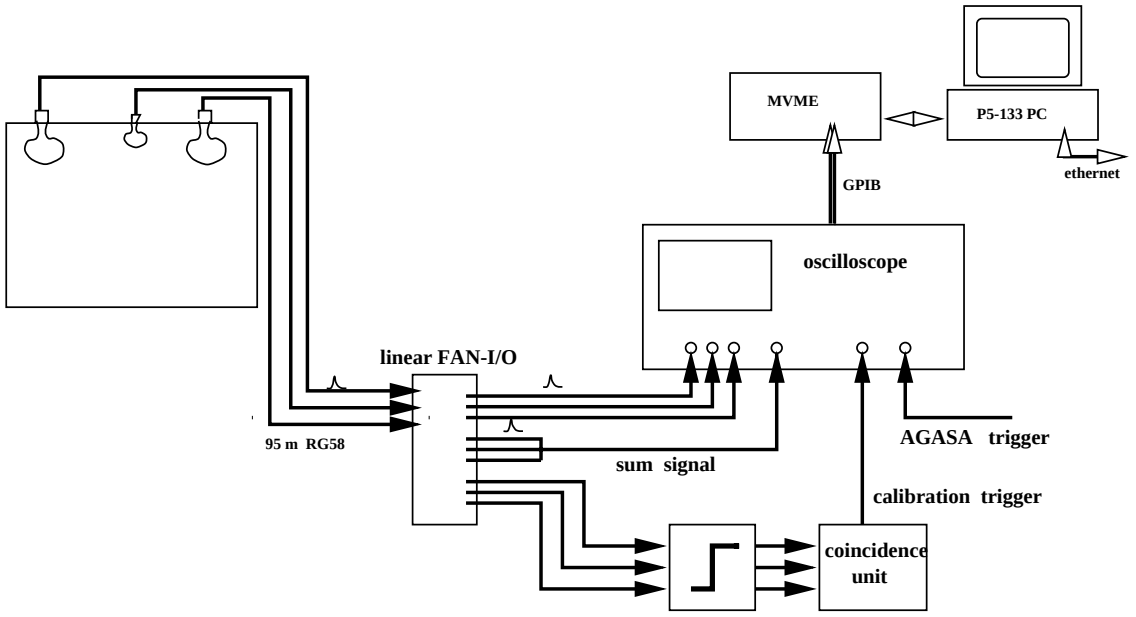

Figure 5.2: *Experimental setup and data acquisition system. The calibration trigger is shown as used for the second prototype detector.*

that the specified dimensions fulfill the project requirements. The photomultipliers measure 200 mm in diameter and have a pseudo-hemispherical, bialkali cathode with typical effective area of 530 cm^2. The electron multiplication is attained by a 13 dynode structure, operating at an overall voltage in the range from 1350 to 1430 V. The high voltages have been set to produce equal pulse sizes for vertical, central muons identified by a muon telescope.
The PMT signals are transmitted via 85 m of RG58 cable to the data acquisition system (DAQ). This consists of a digital oscilloscope (LeCroy 9304A), read out via GPIB to a Motorola MVME 162-222 CPU operating under VXworks. The VME computer is linked to a gateway P5-133 PC computer running under Linux and steering the data acquisition (see figure 5.2). The signals of the three Photomultiplier Tubes viewing the tank volume are split by a LeCroy 428F linear fan-in fan-out. One copy of each PMT signal is fed into a digital oscilloscope, and is recorded by FADCs with a dynamic range of 8 bits, and a sampling rate of 100 MHz. The recording range expands over 800 mV; with an axis offset of 25 mV the recordable range is 25 mV to - 775 mV. Duplicates of all three PMT signals are added together and recorded by the fourth channel of the oscilloscope. This channel accepts signals over a range of 8V, and is intended to yield information on signals from nearby air showers which saturate the three 800 mV FADC channels. The memory depth of

the oscilloscope is 10 kilo samples per channel; at a sampling rate of 100 MHz this translates into a full time scale of 100 μs.
The second prototype detector uses the same type of data acquisition. The main difference between the two water Cherenkov detectors is the inner lining of the detector volume. While the first tank is fully lined with Tyvek, the top surface of the second tank is a black absorber and only the bottom and side walls are Tyvek lined. The idea of this design is to shorten the lifetime of the Cherenkov light produced inside the water volume. Hence, shorter and better resolved peaks are expected to be seen in the signal trace which ultimately could lead to a better separation of the muonic and electromagnetic signal component. Other differences between the two prototype detectors are minor. The PMTs of the second detector are Hamamatsu R5912, which is a follow up model of the R1408 with a 10 dynode structure. The dimensions and in particular the dimension of the photosensitive area are the same as for the R1408. The overall voltages applied range from 1624 to 1762 V; the higher voltages are used to compensate for the smaller number of amplification stages and hence, the actual gain is comparable to the gain of the PMTs used for the first prototype detector. For the second tank, which is not equipped with a muon telescope the PMT high voltages were set to produce equal pulse size distributions when self-triggered by background muons creating signals above a specified minimum threshold (of typically 7 mV in pulse height).
In order to avoid artificial broadening of the signals due to transmission, RG62 cables, which have a higher bandwidth than RG58 were investigated for signal transmission from the PMTs to the DAQ. For a cable length of 30 m no superiority of RG62 over RG58 cable was found; termination problems with RG62 cable led to the decision of using RG58 cable for signal transmission to the DAQ.

5.2 Detector calibration and monitoring

The calibration method used for the water Cherenkov detectors takes advantage of the persistent flux of muons in the atmosphere. By selection of a suitable and preferably strongly constraint subsample of these muons a signal standard can be established.
For calibration purposes the first water Cherenkov detector is equipped with a muon telescope. This consists of two scintillator paddles each measuring 0.1 m^2 in area which are placed below and above the center of the detector. The scintillation counters are read out by a pair of PMTs whose signals are discriminated and fed into a coincidence unit. The output signal is used as trigger indicating the penetration

of a vertical muon at the center of the detector. Hence, integrated signals are specified in units of vertical equivalent muons (VEM). A calibration run typically records $\sim$ 500 signals from muon telescope events. A maximal threshold (750 mV) is applied to the sum of integrated pulse sizes from all three PMTs in order to eliminate events for which more than one particle at a time entered the tank, as would be the case for small nearby air showers. The average value of the remaining distribution is defined as the equivalent of one vertical muon. Figure 5.3 shows the pulse size distribution of such a calibration run. The average pulse size corresponds to a pulse charge of $\sim$ 70 pC. The spread in the pulse charge distribution is about 34% for the individual PMTs and about 19% for the distribution of the sum pulse charge of all three PMTs. The spread can be split into three components: i) the spread in size of the light burst, ii) the Poisson spread of photoelectrons emitted at the photocathode and iii) the spread of the single electron spectrum. Adding up the individual spreads in quadrature will yield the square of the observed fractional spread σ_{obs}:

$$\sigma_{\mathrm{light}}^2 + \left(\frac{1}{\sqrt{n}}\right)^2 + \left(\frac{0.67}{\sqrt{n}}\right)^2 = (\sigma_{\mathrm{obs}}^{\mathrm{indi}})^2, \tag{5.1}$$

where $\sigma_{\mathrm{light}}^2$ is the fractional spread in the size of the light burst and n is the number of incident photoelectrons. The fractional spread of the single electron spectrum amounts to about 0.67 for the R1408 PMTs [79]. The fractional spread $\sigma_{\mathrm{obs}}^{\mathrm{sum}}$ of the sum pulse distribution is also described by equation 5.1 if n is replaced by $3{\cdot}n$. From this system of equations σ_{light} is determined to be $\sim$ 10%. Since this method denotes a lower limit to the number of photoelectrons, n is estimated to be $n \geq 14$ and the total number of photoelectrons observed for an average vertical, central muon is at least 42.
The muon telescope fulfills all requirements to adequately calibrate and monitor the detector. Furthermore, it is a suitable tool to investigate basic detector characteristics such as uniformity and zenith angle dependence [78].

For the Auger project, which envisages to employ $\sim$ 1600 detector stations per Observatory site, it is nevertheless advisable to use a calibration technique which requires no equipment in addition to the three PMTs directly viewing the detector volume. This is more cost effective and also implies higher reliability since the complexity of the detector system is reduced.
The second water Cherenkov prototype detector is calibrated and monitored by a trigger signal from a coincidence of the three PMTs. Each of the PMT signals is discriminated at a threshold of 15.3 mV which corresponds roughly to a two photoelectron pulse. Each individual distribution of typically 500 trigger events shows a modest peak. For small threshold values well above noise level, the peak position

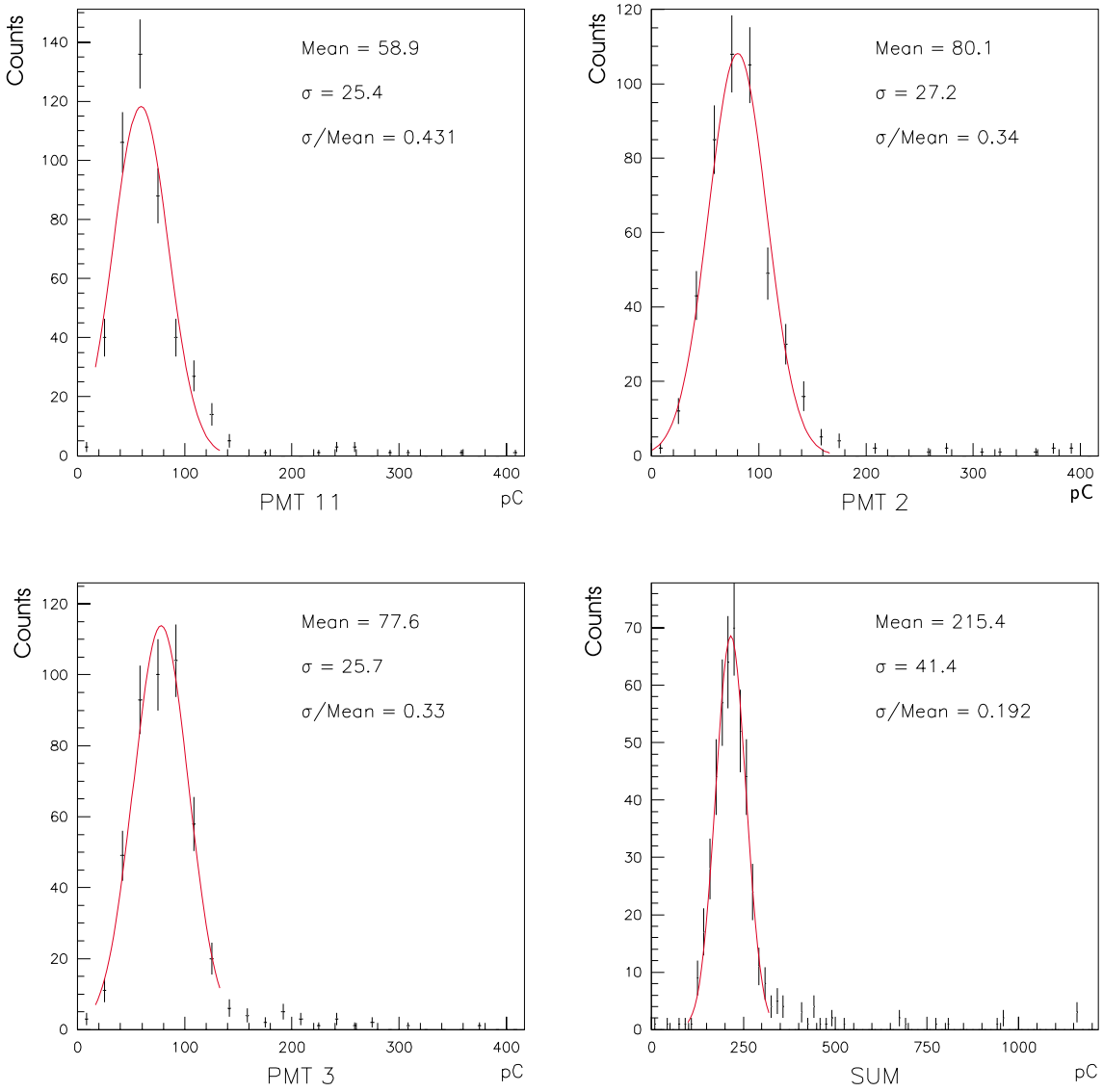

Figure 5.3: *Pulse charge distribution for ∼ 500 vertical, central muons for each of the three PMTs and the sum of all three PMTs. A Gaussian fit was made to the central part of each distribution and its mean value and standard deviation are plotted.*

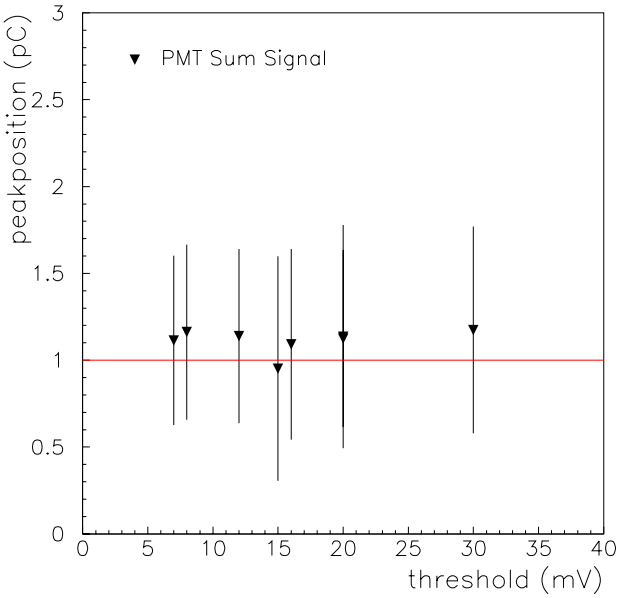

Figure 5.4: *Shown are the peak positions of the sum pulse charge distributions recorded for a threefold coincidence as function of threshold value applied to the signal of each PMT. The peak positions have been normalized by the peak position derived from a pulse size distribution of a muon telescope event. The error bars represent the width of the distributions at a one sigma level (standard deviation).*

is independent of the actual threshold value chosen. This is illustrated in figure 5.4 which shows the peak position of the sum signal distribution as function of threshold value. Since the peak in the distribution of the integrated sum pulse of all three PMTs is more pronounced than in the distributions for an individual PMT, its position is used for calibrating and monitoring the detector.
As can be seen in figure 5.4, the peak positions are on average 1.15 times larger than those for a strictly vertical muon. This correction factor needs to be taken into account when integrated signals, expressed in units of VEM are gauged by calibration data from the threefold coincidence method. (The measurements for vertical muons were done with a muon telescope which had been installed temporarily for purposes of data comparison.) A more detailed description of the threefold coincidence calibration method and other self calibration techniques can be found in [80]. In analogy to the method used for the first water tank the number of photoelectrons per PMT has been estimated to be $n \geq 5$ pes; the total number of photoelectrons obtained for a vertically penetrating muon is therefore $n \geq 15$.

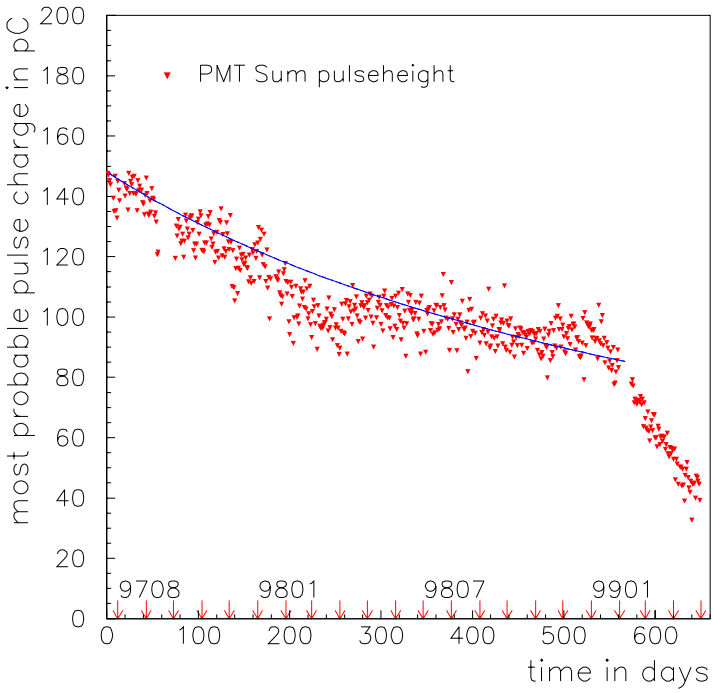

Figure 5.5: *Sum pulse charge as function of time. Each data point represents the average over 500 detector calibration signals.*

The daily calibration data have been used to monitor the stability of the optical properties of the detector. Figure 5.5 shows the pulse charge for calibration data summed over all three PMTs and daily averages over all 500 calibration events as function of time for the second prototype detector. Data are displayed for the time range from August 1997 till April 1999; the water was kept in a closed system and no water exchange took place. An exponential decrease in pulse size and hence in the number of detected photoelectrons is apparent for data up to January 1999; For this time range an exponential curve has been fitted to the data. A similar behavior was detected in the fully Tyvek lined prototype detector. The calibration data do not allow to distinguish between the optical properties of individual detector components and therefore the cause of the pulse decay with time cannot be easily identified. The strong decay of signal size starting in January of 1999 is certainly due to the growth of algae inside the detector as tests revealed the detector to be green on the inside. No such indications were found for the earlier period. However, it is currently assumed [90] that some sort of biological growth in the water or at the inner detector walls is also responsible for the exponential decay of the optical detector quality.

5.3 Simulation of the detector response

In order to fully understand the data coming from the water Cherenkov prototype detectors it is necessary to have detailed knowledge of the behavior of the detector components being used. In particular the knowledge of spectral characteristics of the lining material and the water as well as the photomultiplier tube characteristics are important input parameters for a detector simulation which in turn should improve the understanding of the measured parameters and the interpretation of recorded data.
Detector simulations have been carried out with the custom written code "AGASim" [81] whose major advantage is its computational speed when compared to standard detector simulation packages such as GEANT [82]. "AGASim" ray traces Cherenkov photons created by relativistic particles entering the water volume of the detector. Once a photon hits the photocathode of one of the 3 PMTs a complete photomultiplier simulation based on Poisson statistics and a measured single electron spectrum is followed trough. After completion of the ray tracing and PMT simulation process the simulated anode signal is submitted to calculated alterations by the transmission cable and the data acquisition electronics.
The single electron spectrum (ses) for two sample PMTs of type R1408 operating at a voltage of ~ 1.4 kV was investigated by means of a laser test setup at Fermilab [86]. The spectra, of which one is displayed in figure 5.6 and which turned out to be worse than specified by the manufacturer, are used as input to the PMT simulation. The correctness of the ses has been tested by reproducing measured signal distributions at higher light intensities. If the number of photo electrons (pes) is obtained by sampling from a Poisson distribution and the resulting charge for each pe is drawn from the ses than a charge distribution for any given mean value of pes can be generated [87]. Figure 5.7 shows the measured (points) and predicted (solid line) signal pulse charge distributions at two different light levels. The agreement is good and provides a consistency check between data and simulations. Furthermore, the same test facility was used in combination with a set of attenuation filters to vary the light intensity of the laser pulses such that the linearity of the PMT response could be examined. Good linearity was found; however, the range explored reaches only up to the equivalent of about 4 to 5 vertical muons in the water Cherenkov prototype detector [87].
Spectral characteristics of the absorption length of pure water [83], the Tyvek lining [84] and the quantum efficiency of a bialkali photocathode [79] as used for the simulation are specified in figure 5.8. Uncertainties arise from the fact that Tyvek was measured in air and not in water and that the curve for the absorption length was inferred for clear water. Hence, the shape and normalization of the latter can

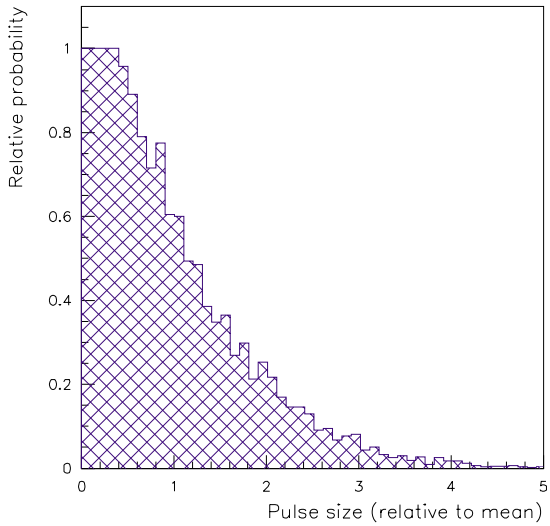

Figure 5.6: *Single electron spectrum as measured for a R1408 PMT at an operating voltage of 1.4 kV.*

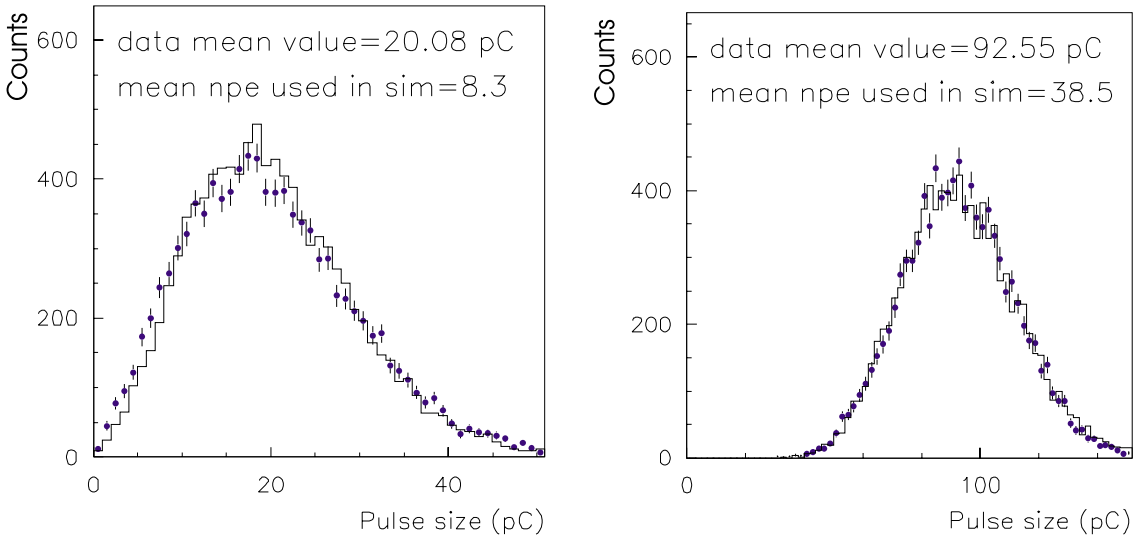

Figure 5.7: *Measured (points) and simulated (solid histogram) pulse charge distributions for two different light intensities. Simulations are based on Poisson statistics and the experimentally determined single electron spectrum of the R1408 PMTs.*

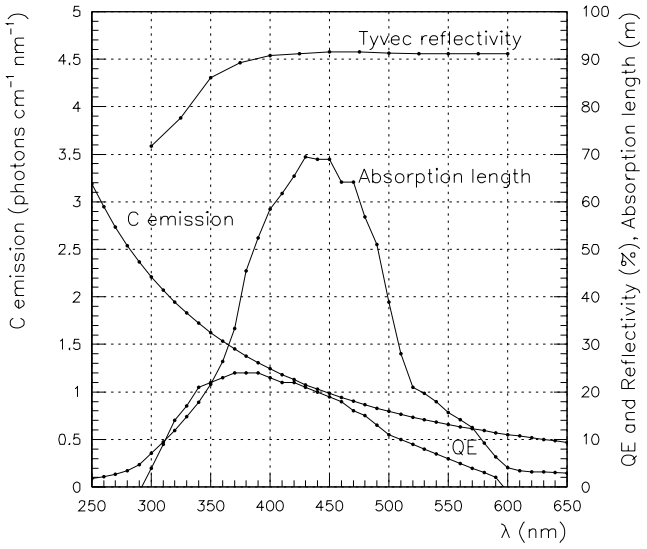

Figure 5.8: *Spectral characteristics for a water Cherenkov detector [85]. The emission of Cherenkov light is calculated for a fully relativistic particle.*

be expected to alter [85]. If the peak absorption length is adjusted to 35 meters [85] the average pulse shape of muon telescope events can be very well reproduced as is shown in figure 5.9. The data curve has points and the simulated average signal curve is represented by a solid line. The average muon pulse shape shows a long exponential tail with a decay constant of ~ 55 ns. This exponential tail originates partly from the signal transmission through 80 m long RG58 cables as was first demonstrated by direct measurements [87] and later confirmed by simulations [88]. It is noteworthy that individual muon pulse shapes show a rich time structure which is due to diffuse reflections of Cherenkov light of the inner detector walls. Figure 5.10 shows 2 experimentally recorded and 2 simulated pulse shapes of individual muon events. The good agreement between simulated and measured pulse shapes results in agreement between the measured and simulated charge distributions in the central region between 150 and 250 pC in which the majority of pulses fall (cf. figure 5.12). Minor disagreement was found between the experimentally observed high end tail of the distribution which was not reproduced by simulations. It is assumed that this tail is due to δ-ray production and at the most extreme pulse charge values, due to small air showers triggering the muon telescope — both effects are not included in the detector simulation [85].
A similar exercise was carried out to simulate the self-calibration method used for the second prototype detector. A significant difference arises from the fact that

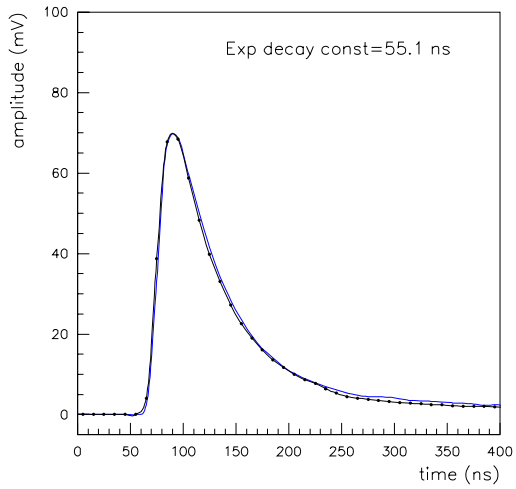

Figure 5.9: *Average pulse shape of vertical central muons selected by a muon telescope. Simple solid line and line with points are simulation and data respectively [85].*

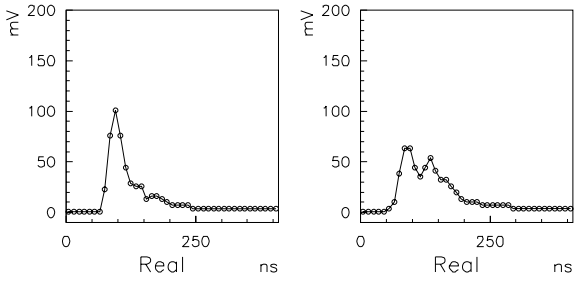

Figure 5.10: *Waveform traces from individual vertical muon events from the first prototype detector at AGASA.*

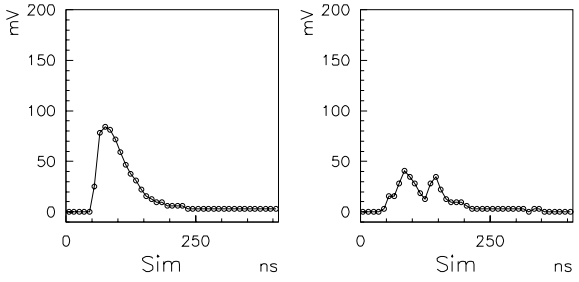

Figure 5.11: *Waveform traces from simulated individual vertical muon events for a fully Tyvek lined water Cherenkov detector [85].*

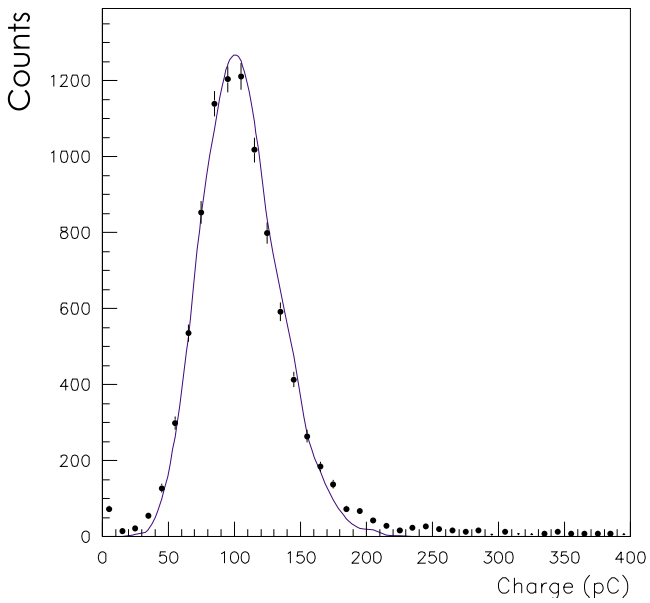

Figure 5.12: *Muon charge distribution from muon telescope events. Points and solid line represent data and simulations respectively [85].*

muons at all zenith angles and all energies need to be considered as the selection of triggering muons is less severe for the threefold coincidence method than it is for the muon telescope. Figure 5.13 shows the expected Cherenkov light pulse amplitude distribution originating from background muons entering the detector; zenith angle and muon energy spectrum effects are included. If self-trigger conditions are applied to the simulated PMT signals, signal size distributions similar to the experimentally observed can be obtained [89]. Some disagreement was found in the region of smaller than average and larger than average pulses. However, it is likely that this deficiency can be attributed to the simulation: the low energy part of the ground level flux, that is mostly electromagnetic particles, has been ignored. Furthermore, the decay electrons of stopping muons are not considered. Larger than average pulses will be underestimated by the simulations for the same reasons as mentioned above. A detailed experimental study [80] and according simulations [89] of a variety of self-trigger mechanisms has been carried out for the water Cherenkov prototype detectors at AGASA, and was documented in form of Auger collaboration technical notes.

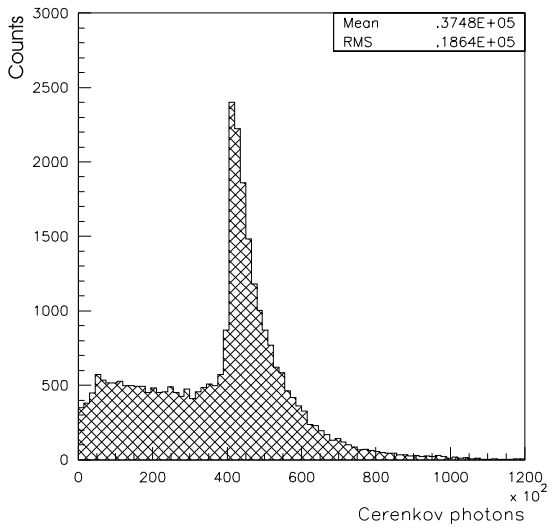

Figure 5.13: *The amplitude distribution of Cherenkov light pulses inside the detector volume as expected from simulations which include zenith angle and energy spectrum effects of the ground level muon flux [89].*

5.4 Observation properties of water Cherenkov detectors

A muon telescope represents an excellent tool, not only to calibrate the water Cherenkov prototype detector but also to investigate its basic properties. The dependence of signal size on distance between PMT and Cherenkov light emitting particle was investigated by placing the muon telescope at eight different detector positions. The distance was increased in step sizes of 40 cm and at each position a total of 1000 muon events was recorded. The pulse size (charge) was found to depend strongly on distance for distances up to 1.5 m beyond which it becomes almost constant. However, the sum pulse charge of all three PMTs is constant within $\sim 5\%$ if none of the PMTs is hit directly by an entering particle [78].
Furthermore, the dependence of signal size on track length was studied by selecting muons incident on the detector at various zenith angles θ. For this study the top scintillator of the muon telescope was fixed at the tank center while the bottom scintillator was moved at steps of 20 cm. For muon incident angles up to 45° the pulse charge summed over all three PMTs was found to be proportional to the track length l of the particle: $l = h \cdot sec\,\theta$, where h indicates the height of the detector. At particle incident angles larger than 45° the pulse size becomes larger than expected from the increase in path length [78]. This can be easily understood by

direct irradiation of Cherenkov light onto the photocathodes of the PMTs. For this work air shower signals up to 45° have been investigated. Since individual particles show only little scatter around the shower axis the effect of direct irradiation can be neglected in the present study. However, any analysis of highly inclined air showers ($\theta > 45°$) needs to account for large pulse sizes caused by direct Cherenkov light ! An important characteristic of the water Cherenkov detector design is its large depth of 1.2 m. It is this finite height which makes the detector's effective surface almost independent to air showers impinging at various zenith angles. The effective surface is constant to within 9% for showers with zenith angles up to 45° and constant to within 12% for showers with zenith angles up to 60°.

5.5 Water Cherenkov detector (WCD) operation and the Akeno Giant Air Shower Array

The two water Cherenkov prototype detectors on which this work is based have been operated within the Akeno Giant Air Shower Array (AGASA) in Japan, a scintillator array covering 100 km^2 in area. The first detector (WCT1) is located at the south east corner of AGASA and the second prototype detector (WCT2) is located more centrally in the Akeno branch; its location is near the AGASA detector AB32. In figure 5.14 locations of WCT1 and WCT2 are marked by a star.
Most of the time the two water Cherenkov prototype detectors are operated in air shower mode, meaning that they receive a trigger signal from AGASA upon detection of an air shower. In addition to air shower signals, each day 500 muon events are recorded for calibration purposes. This calibration measurement takes about 30 min and corresponds to an off-line time of about 2% per day.

5.5.1 The Akeno Giant Air Shower Array (AGASA)

The Akeno Giant Air Shower Array (AGASA) is located in Japan, $\sim$ 120 km to the northwest of Tokyo in the southern Japanese Alps at an altitude of about 900 m above sea level (corresponding to an atmospheric depth of $\sim$ 920 g/cm^2). The array, spread over an area of about 100 km^2 consists of 111 scintillation detectors, each measuring 2.2 m^2 in area and 27 muon detectors of six different sizes. The scintillation detectors are placed with a nearest-neighbor separation of about 1 km and are sequentially connected with a pair of optical fibers. The array is divided into four branches and information is passed on and processed in the four branch controllers. The array layout and the communication network are shown in figure 5.14. The four

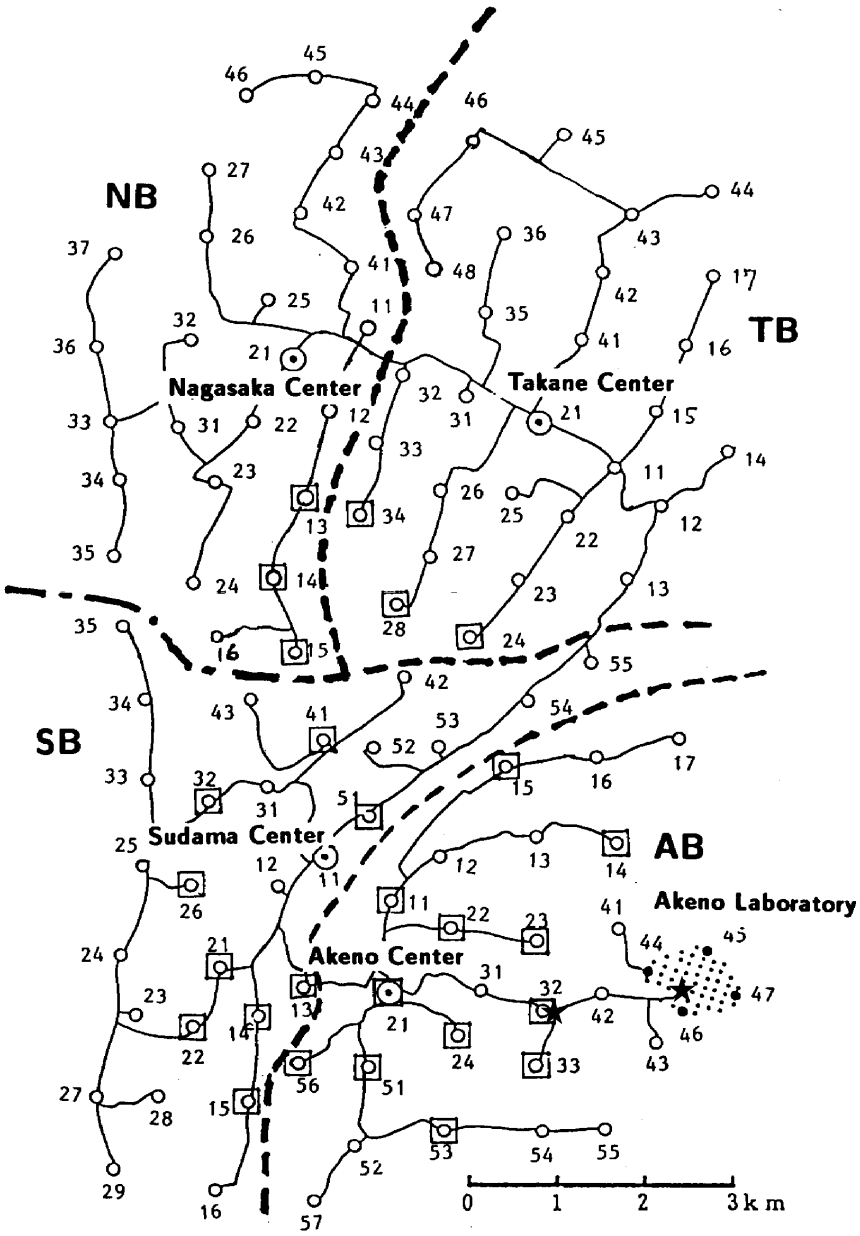

Figure 5.14: *Schematic view of the AGASA. Open circles and squares represent the surface detectors (scintillators) and the shielded muon detectors (proportional counters), respectively. Solid lines show the routes of the optical fibers for the data communication network. Dotted lines are the boundaries of the four branches [22]. The locations of the water Cherenkov detectors are indicated by stars.*

branches of AGASA have been operated independently since 1990. In 1995 the four branches were unified by the implementation of a fast trigger exchange communication system and the 100 km^2 array has been operated successfully and stably ever since.
AGASA registers an event whenever five or more neighboring detectors record a signal within a coincidence window of 26 μs. In order to reduce accidental coincidences the pattern of hit detectors is compared to a set of stored patterns which has been selected from combined air shower and detector simulations. The effective detection area (area $\cdot$ solid angle) of AGASA is independent of the primary energy above $\sim 10^{18.5}$ eV and amounts to a value of 125 km$^2 \cdot$sr. However, at lower energies the effective detection area clearly depends on primary energy and varies from about 70% of its maximum value for energies around $10^{18.0}$ eV to 125 km$^2 \cdot$sr for energies above $\sim 8 \times 10^{18}$ eV [23].

5.5.2 The recording of EAS signals

The data acquisition system of both water Cherenkov detectors is triggered by the Akeno branch trigger of AGASA at a rate of 1 per minute; about 99% of these triggers are accidentals or partly caused by very low energy air showers. Since this trigger is formed at the branch center located several kilometers away from the water tank the trigger signal is delayed by about 70 μs with respect to the water Cherenkov signal. Upon receipt of an external trigger signal, the FADC traces of all 4 channels for the time period 100 μs to 50 μs before the occurrence of the trigger are read out and saved to disk along with a time stamp. The later permits identification of corresponding AGASA events off-line. Although the time delay of the AGASA trigger pulse depends on the arrival direction and core position of the shower, this time period is sufficient to grasp all signals from showers hitting the Akeno branch. Air shower data have been recorded with the first and second water Cherenkov detector since July 1996 and July 1997, respectively. Although data taking continues at the time of writing only data until November 1998 have been used for this work. The reason being problems in proper matching of water Cherenkov and AGASA events for December 1998 due to AGASA network problems and in 1999, the detectors partly being used for particular studies such as the determination of background event rates [106]. However, for both detectors the overall dead time (excluding time allocated for calibration measurements) was less than 2% for the data period until November 1998. In the energy range from 10^{18} to 10^{19} eV, 1007 events have been recorded, whereas at higher energies, between 10^{19} to 10^{20} eV, 26 events and above 10^{20} eV 2 events were recorded.

Chapter 6

Separation of the Muonic and Electromagnetic Components in WCD Signals Originating from Extensive Air Showers (EAS)

Cosmic ray showers originating from iron nuclei contain more muons than proton initiated showers of same primary energy. Hence the ratio of muonic to electromagnetic particles in extensive air showers is sensitive to the nature of the primary particle. To gain some understanding of cosmic ray composition this information needs to be extracted by analysis of the structure of air shower signals as recorded by water Cherenkov detectors.

6.1 Characteristics of EAS-muon signals

Two characteristics of EAS muons can be taken advantage of in order to separate the muonic from the electromagnetic component:

1) The calorimetric water Cherenkov detection technique is comparably more sensitive to muons than electromagnetic particles due to the muons' higher per particle energy. Muons are expected to produce more pronounced peaks in signal traces recorded by water Cherenkov detectors.

2) Furthermore, simulations reveal the muons to arrive earlier than the bulk of electromagnetic particles. The latter arrive over an extended period of time

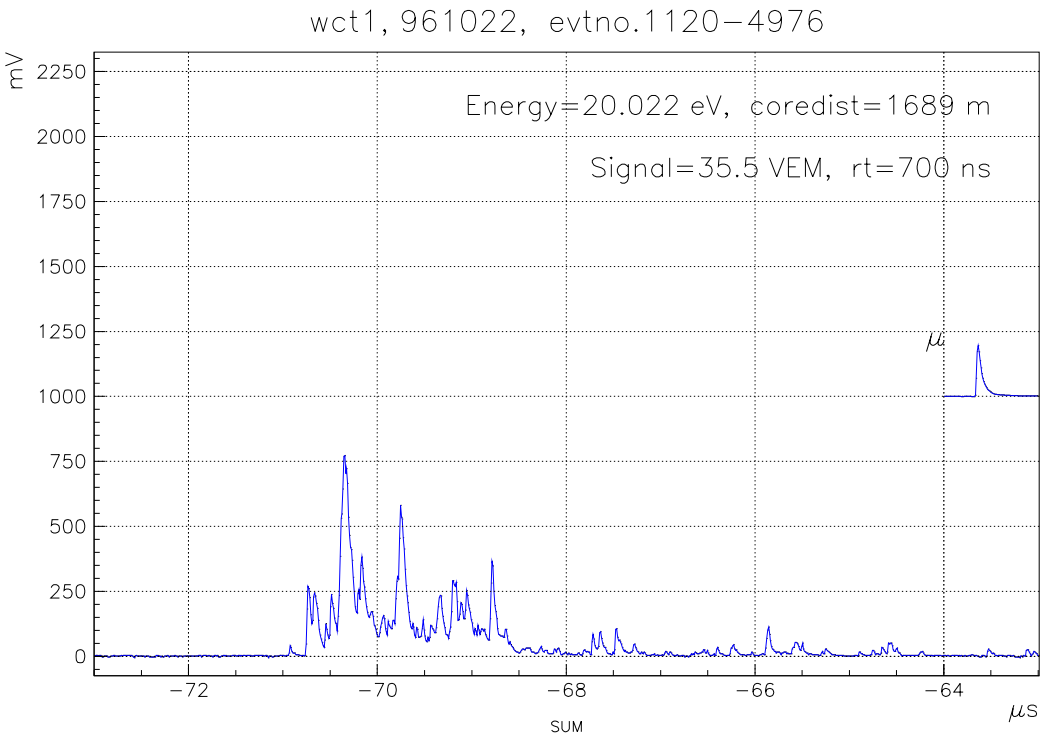

Figure 6.1: *Air shower event of primary energy $10^{20.0}$ eV and zenith angle $\Theta = 33.5\,^{\circ}$ as recorded by WCT1 (white top) at a core distance of 1.7 km. Also shown is the average signal of 500 vertical muons penetrating the detector at the center. The time offset of about 70 μs is caused by the formation of the AGASA trigger (cf. section 5.5.2).*

and in larger quantities which results in broader pulses by superposition of many individual pulses.

These properties may permit the contribution of the muon component to be estimated from the recorded FADC traces. Indeed do some experimentally recorded signals clearly show a peaked "leading" component and a variety of small and broad pulses at the "trailing edge" of the trace. Figure 6.1 shows the FADC signal trace of a 10^{20} eV air shower event recorded at a core distance of ∼1.7 km. The signal structure is characteristic for the distribution of particles within the shower front, which for the example in hand, has a thickness of 6 to 7 μs at core distances around 1.7 km. Despite the fact that a number of pronounced peaks can be seen at the "leading" edge of the trace, the signal structure is complex and the overall ability to separate electrons from muons appears to be rather difficult.
The following approaches have been suggested to tackle the problem:

i) Rise time and shower front curvature analysis:
The rise time t_{10-50} is the time in which the integrated signal originating from an EAS rises from10% to 50% of its total integrated charge (cf. figure 3.1). It can be easily determined and is correlated with the muon content of an air shower as muons tend to arrive earlier than the bulk of electromagnetic particles. At any given core distance the rise time t_{10-50} is expected to be smaller for muon rich, and hence iron initiated EAS. With increasing core distance the spread of shower particles increases which also results in lager signal rise times [91, 92].
The shower front curvature can be determined by measuring the signal times t_{10} as function of core distance. The time t_{10} is defined as the time in which the integrated signal rises to the 10% level of its maximum integrated charge (cf. figure 3.1). In iron initiated air showers muons tend to be produced in greater height than in proton showers of same primary energy. Hence, at large core distances muons arriving from great heights will arrive earlier than those produced at lower heights. This is for purely geometrical reasons as muons arriving from lower production heights have longer path lengths than those arriving from large heights; see figure 3.4. Therefore the shower front curvature is expected to show some sensitivity towards the mass of the primary cosmic ray.

ii) Signal structure analysis:
Exploiting the signal structure of FADC traces is less straight forward than the determination of rise times and a number of different analysis have been suggested [93, 94, 95]. In all approaches the basic idea is to relate the signal fraction above a certain threshold to the muon content of the corresponding air shower.

6.2 Description of EAS and detector simulations

The development of muon extraction techniques must rely on simulations for which the muon fraction of the signal is well known a priori. A detector simulation study [96] indicated that even with a special muon detector placed underneath a water Cherenkov detector the muon content could not be measured sufficiently accurate as to enable the development of muon extraction algorithms solely based on experimentally recorded signal traces. Electromagnetic contamination in such a muon detector, caused by the conversion of gamma-rays inside the water Cherenkov detector volume, amounts to $\sim$35% of the expected muon signal.

For the study at hand, air shower simulations have been taken from a shower library which has been created for the Pierre Auger experiment and contains information about air shower particles at ground level from approximately 1000 simulated air showers, half of which were initiated by protons and half by iron nuclei. These EAS have been simulated with the program MOCCA (M.Hillas [76]) using the hadronic interaction model Sibyll [97, 98]. The energies and zenith angles of the primary cosmic rays range from 10^{19} to 10^{20}eV and up to 60°. For each shower a list of ground particles, characterized by their energy, arrival time and particle type is produced. Following, particles are re-sampled from the ground particle flux distributions and injected on individual water Cherenkov detectors. The detector simulation code AGASim [81] — containing all essential physical processes relevant for a water Cherenkov detector and already mentioned in section 5.3 — tracks every particle entering the detector and calculates the number of photons hitting the photomultipliers. Finally the number of photon hits is converted into a number of photo-electrons and corresponding FADC counts. The detector simulation allows to keep track of the particle type up to the generation of FADC traces, the last stage of the simulation. Therefore, not only the muon fraction of individual FADC signals is known but it is also possible to relate individual peaks in an FADC trace to the type of particle by which it was caused. Undoubtedly, the simulations are a very powerful tool to develop muon extraction algorithms.

6.3 The muon extraction algorithm

The approach chosen for the extraction of the muonic component of air shower signals is based on the large pulse sizes expected for muons and their early arrival time with respect to the arrival of the electromagnetic component. The idea is to count the number of individual peaks appearing in a simulated FADC trace and estimate the type of the particle causing them, based on the peak height and their timely appearance in the signal trace with respect to the time spread of the entire signal.
Identification of peaks occurs primarily by detection of a change of sign in the first derivative of the signal trace. However, this criterion alone is not sufficient to reliably determine peak positions as fluctuations mimic peaks. Additional selection conditions in form of constraints on the magnitude of the change of slope or the size of the range of monotonic behavior around the signal peak, help to suppress artificial peaks originating from fluctuations and thereby improve the recognition of peaks originating from EAS particles. For each peak the absolute peak height is determined.

The WCD average response function to vertical muons shows long exponential tails with a time constant of up to τ=60 ns. These will cause signal pile up effects if a series of particles is recorded within a time range of the order of the decay time of individual particle signals. Typical peak distances are of the order of a few tens to a few hundreds of nano seconds (cf. figure 6.1), depending on the core distance at which they are observed. Hence, corrections need to be applied in order to accurately determine actual peak heights. It is assumed that the average pulse shape of vertically penetrating muons is representative for the shape of all individual peaks in FADC signal traces. The actual peak height of individual spikes is then estimated by subtracting an offset caused by the tail of the preceding peak from the absolute peak height. The offset is calculated from the relative distance between neighboring peaks and the pulse of an average muon signal which has been normalized to the peak height of the preceding peak.
If an actual peak height surpasses a threshold of 60% the height of a standard muon pulse, the peak is retained as a potential muon peak. However, it is only considered to be of muonic origin if it appears within the time in which the integrated signal rises from zero to the 70% level of its total integrated charge. This conditions aims to improve the performance of muon recognition by exploiting the early arrival of muons with respect to the electromagnetic shower component. For the remaining peaks, classified to be of muonic origin, the nearest integer smaller than or equal to the ratio of actual peak height h_a to the average pulse height $<h_{\mathrm{muon}}>$ of a vertically penetrating muon, serves as an estimate for the number of muons causing the corresponding peak. The sum of these integers calculated for the entire FADC trace specifies the number of reconstructed muons n_μ^{recon} per EAS signal:

$$n_\mu^{\mathrm{recon}} = \sum_{i=1}^{n} \left[\frac{h_a^i}{< h_{\mathrm{muon}} >} \right] , \tag{6.1}$$

where n indicates the number of muon like peaks for the FADC trace of one detector.

6.4 Analysis results and the lateral muon distribution

The described analysis procedure has been applied to simulated FADC traces captured at core distances of up to 3 km for events with 19.0<log(E_0)<20.0. Both type of prototype detectors have been simulated: a fully Tyvek lined and a black top detector. Figure 6.2 shows the logarithm of the ratio of the number of reconstructed

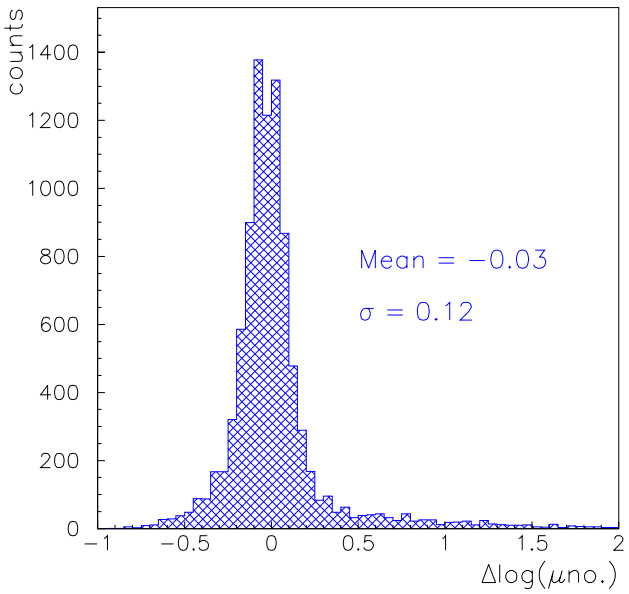

Figure 6.2: *Fluctuations of reconstructed muon number for showers with energies between 10^{19} and $10^{20}\,eV$ and $\sec\theta < 2$ recorded at core distances of up to 3 km. The horizontal axis shows the logarithm of the ratio of reconstructed to actual number of muons per FADC signal trace. The detector simulation assumed a white top detector.*

muons n_{recon} and the number of muons entering a fully Tyvek lined detector n_0. The width of the distribution represents the muon number resolution and amounts to 30% at half maximum. The reconstruction of the muon content works equally well for proton and iron initiated showers; furthermore no differences between the white and black top detectors were found. The muon extraction algorithm was also run without the previously described time based selection criterion. The resolution of the extracted muon number did not change significantly.
A simulated average lateral muon distribution has been derived from the same set of EAS data which have been used for the muon extraction analysis It is used for comparison with the average lateral muon distribution derived from the number of muons which have been reconstructed from FADC signal traces recorded at various core distances. Both of these distributions were normalized to a primary shower energy of $10^{18.8}$eV and are shown in figure 6.3 along wit the lateral muon distribution as published by the AGASA collaboration [60] for muons with energies above 1 GeV. The simulated average lateral muon distribution is represented by triangles; the lateral distribution estimated from the reconstructed number of muons with the

previously described muon extraction mechanism is shown by squares. The curve represents the lateral distribution of muons as reported by AGASA for EAS in the energy range from $10^{17.0}$ - $10^{19.5}$eV. The muon reconstruction mechanism seems to

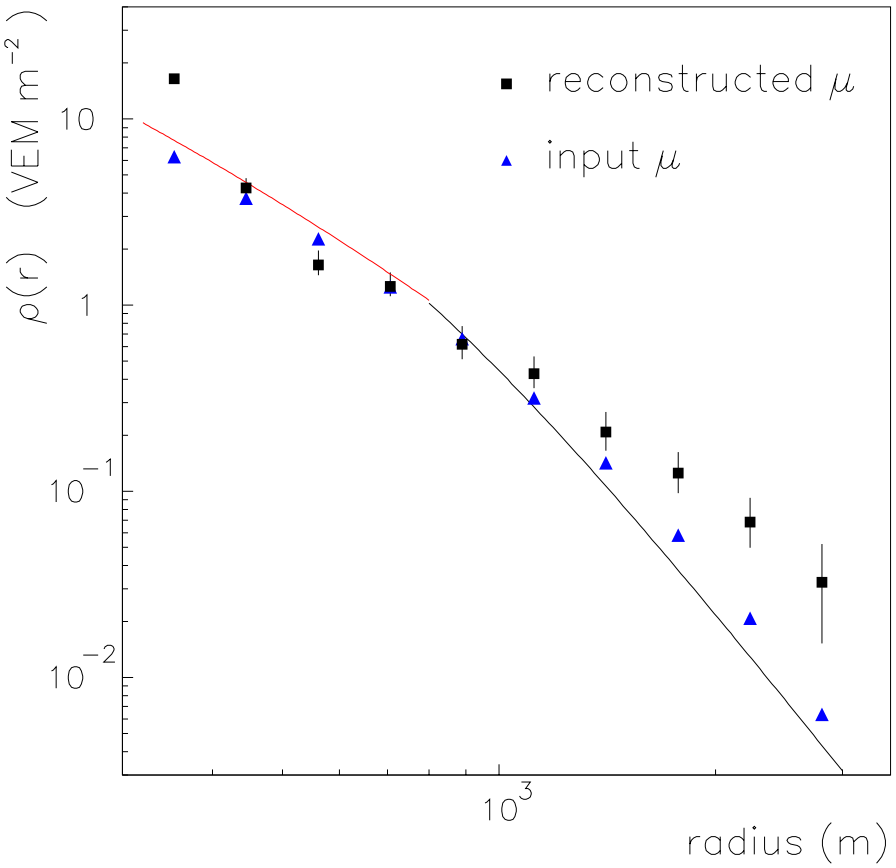

Figure 6.3: *Triangles and squares represent the average lateral muon distribution for input and reconstructed muons in units of vertical equivalent muons (VEM). Both distributions were normalized to a primary energy of $10^{18.8}$ eV. Error bars represent the standard error of the mean. The curve represents the published AGASA muon LDF [60].*

accurately reconstruct the number of actual muons at core distances between 600 m and 1000 m. At core distances beyond 1 km the muon number n_μ^{recon}, as reconstructed from water Cherenkov detectors overestimates the actual muon number by $\sim$50% at core distances around 1.2 km and by up to a factor of 4 at core distances beyond 2.5 km. This result is rather surprising since the time spread of particles arriving at large core distances is larger than at small distances: one would expect better separation capabilities of individual particle peaks at large core distances. No

error could be identified in the described muon reconstruction program.
Since the resolution of muon reconstruction is equally good for iron and proton initiated showers, an attempt was made to classify these events into categories of "heavy" and "light", based on the extracted muon parameter. Results from the muon estimation algorithm described suggest only a loose coupling between the resulting muon parameter and the mass of the primary cosmic ray. However, in combination with other composition sensitive parameters such as signal rise time t_{10-50} and shower front curvature, a muon content parameter might prove very valuable.
The limited success of the presented muon extraction algorithm and reports [95] from a more successful approach to gain composition information from a parameter, which is based on signal size, lead to the decision to abandon the investigated method. This other approach first deconvolutes the FADC signal traces with a simple triangle response function. This is a standard process in signal processing. Signal traces are integrated if the signal would surmount a specified threshold. A classification of showers into "light"-like and "heavy"-like primaries was described to work only if information from simulated FADC traces of several water Cherenkov detectors, hit by one air shower is combined. Only detectors at core distances larger than an energy dependent threshold would be considered for this muon extraction analysis. This method seems more promising than the peak identification and counting method described described in this work, as it exploits standard signal processing techniques.

Chapter 7

Cross-calibration of the AGASA and Haverah Park Energy Estimation Techniques by Means of the Auger Water Cherenkov Prototype Detectors

The idea is to take advantage of redundant air shower information originating from observations simultaneously performed by two different techniques. Not only are the observed air showers characterized to a greater degree but they can also be used to help identify systematic biases in air shower detection by any of the involved techniques. It is the goal to estimate the primary energy of air showers detected by AGASA by means of the water Cherenkov prototype detectors. Differences in energy estimation by the AGASA and WCD analysis must then be due to particularities in either one or both of the techniques. Due to the similarity of the prototype detectors and the detector modules used in the Haverah Park experiment (cf. appendix A), signal density measurements by these detectors can be compared without need of any conversions. As a result the prototype detectors function as a link between the AGASA and Haverah Park energy estimates and hence the corresponding cosmic ray spectra can be evaluated on the basis of the prototype measurements.
Two water Cherenkov detectors are not sufficient to represent an array of detectors with which an air shower could be fully characterized. However, when results from the HP array are assumed to be valid for the 1.2 m deep prototype detectors, the primary energy of an air shower can be estimated by individual water Cherenkov

density measurements. If the measured signal density is sufficiently large and hence Poisson fluctuations are small the estimate is expected to be accurate. In addition to a water Cherenkov LDF and energy conversion model which are provided by the Haverah Park experiment [10] the shower core position and zenith angle need to be known and must be taken from the AGASA analysis. Figure 7.1 outlines the idea of how to estimate the shower energy of any given event with an individual water Cherenkov detector placed within an array of scintillation counters. As a first step the measured signal densities need to be corrected for accidental signals originating from background muons and small air showers. The background event rate was measured separately [106] (see also B) and found to be $1.7{\cdot}10^{-3}$ VEM/μs for detectors with 10 m^2 surface area. Since air shower signals are typically integrated over a time range of up to 20 μs the average accidental correction for non-zero signals amounts to about 0.003 VEM/m^2 if many events are grouped together in bins. The effect of this correction has only marked impact ($\geq$ 20%) at large core distances where signal density values are expected to fall below 0.01 VEM/m^2. This corresponds to core distances of 2.2 km and 2.8 km for showers with energies in the range $10^{18.0}$ - $10^{18.2}$ eV and above $10^{18.6}$ eV, respectively.
With knowledge of shower core position and zenith angle the experimentally recorded water Cherenkov signal density can be expressed as function of core distance and can be corrected for zenith angle dependent attenuation effects of the air shower in the atmosphere. The signal density value at 600 m core distance is inferred by means of the Haverah Park lateral distribution (cf. equations 4.1 and 4.3): After normalization of the LDF to the water Cherenkov signal density measurement at the respective core distance of the event, $\rho(600)$ can be calculated easily. Due to differences in atmospheric depth of the site of data taking (920 g/cm^2) and the Haverah Park array (1018 g/cm^2), for which the parameterizations were established, corrections for attenuation effects need to be applied. These corrections are detailed as follows:

1) **Lateral distribution function:**
As far as penetrated slant depth is concerned a vertical shower at an observation level of 1018 g/cm^2 is equivalent to a shower with an inclination of 25° at an observation level of 920 g/cm^2. Therefore the relative angle between vertical and actual shower inclination as it appears in the exponent η of the lateral distribution function needs to be reduced by this amount. The parameterization of η changes into:

$$\eta = 2.2 - 1.29 \cdot \frac{920}{1018} \cdot (sec\,\theta - 1) + 0.165 \cdot log\left(\frac{E}{10^{17eV}}\right), \qquad (7.1)$$

and consequently the LDF becomes steeper.

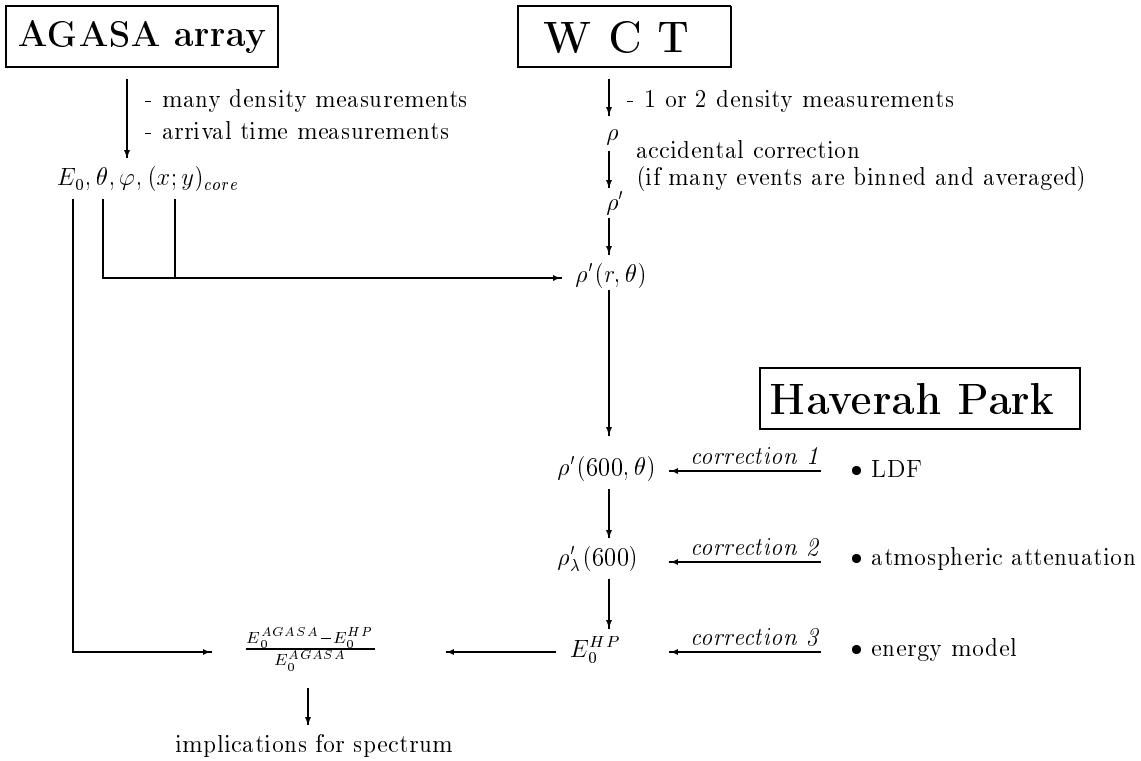

Figure 7.1: *Flow diagram of analysis procedure to cross calibrate water Cherenkov and scintillation detectors.*

2) **Attenuation length λ:**
The attenuation length at the HP level was determined to be 760 $\pm$ 40 g/cm^2 by the method of equal intensity cuts [59](chapter 16.2.2). It is expected to be somewhat longer at higher altitudes and for the following analysis it was assumed to be 850 g/cm^2 since no measurements could be conducted. However, even for θ=45° the difference between the derived primary energies with λ_{Akeno}=760 g/cm^2 or 900 g/cm^2 is less than 6%. The air shower attenuation length determined by the AGASA experiment can not be applied as the scintillator data recorded by AGASA has a larger electromagnetic signal fraction than the WCD signals and electromagnetic particles have a shorter attenuation length than muons.

3) **Energy model:**
The HP energy model, that is the conversion from $\rho_\lambda(600)$ to energy, was established from simulations carried out for observations at sea level ($\sim$ 1018 g/cm^2) and found to be

$$E_0^{\mathrm{HP}} = 7.04 \times 10^{17} \cdot \rho_{\lambda_{\mathrm{HP}}}(600)^{1.018} \text{ eV} \ . \tag{7.2}$$

$\rho_{\lambda_{\mathrm{HP}}}(600)$ denotes the water Cherenkov signal density for a vertical shower at a core distance of 600 m. In order to use the same energy conversion factor for data from the water Cherenkov detectors at Akeno (observation level of 920 g/cm^2), the density at 600 m from the core needs to be corrected to the density of a shower with the same primary energy and a zenith angle of 25° according to

$$\rho_{\lambda_{\mathrm{HP}}}(600) = \rho^{25^\circ}_{\lambda_{\mathrm{Akeno}}}(600) = \rho(600) \cdot exp\left(\frac{920}{\lambda_{\mathrm{Akeno}}}(sec\,\theta - \frac{1018}{920})\right) . \tag{7.3}$$

In addition to atmospheric attenuation corrections whose sum effect alters the inferred estimation of primary energy by less than 10%, the uncertainty of the core position as measured by AGASA needs to be taken into account as it can have a strong effect on the derived density $\rho(600)$ at 600 m core distance, and hence the primary energy E_0. E.g. for a density measurement at 1 km core distance a 100 m core location uncertainty translates into an energy uncertainty of +41% and -28%, respectively. At larger core distances this effect becomes less significant but Poisson fluctuations originating from the shower front sampling process by the detectors become more important and hence contribute more strongly to the uncertainty in energy estimation.
The core position uncertainty for AGASA showers depends on the number of hit

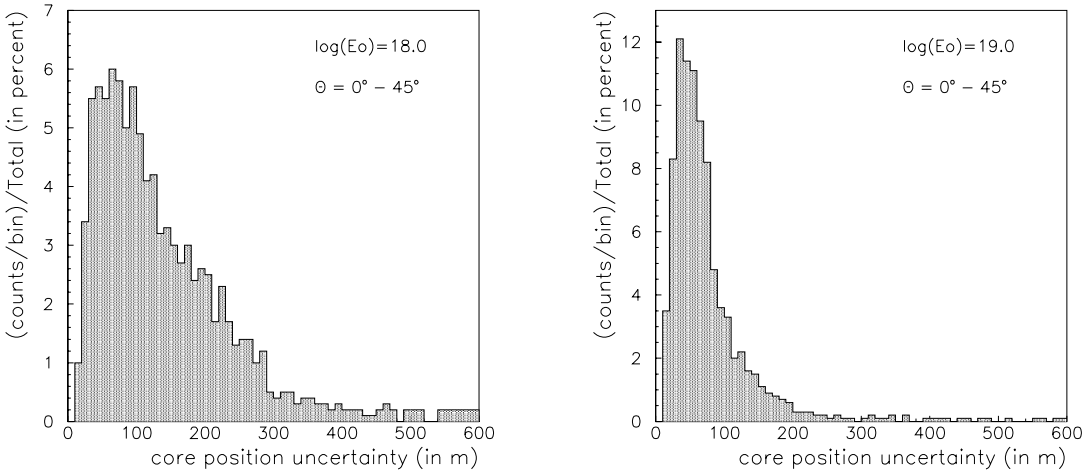

Figure 7.2: *Distribution of core location uncertainties in AGASA as obtained from reconstructed simulated showers of energy $10^{18.0}$ eV and $10^{19.0}$ eV respectively and zenith angle less than 45° .*

detectors and hence on the energy of a shower. It is furthermore strongly correlated with the uncertainty in energy assignment and can only be characterized in a statistical way. Figure 7.2 shows the core uncertainty distributions for showers with energies around 10^{18} and around 10^{19} eV as was derived from simulations carried out by the AGASA collaboration [105]. Air showers with directions sampled from an isotropic distribution were simulated in the energy range from 10^{18} to 10^{20} eV and injected over an area larger than the size of the array. After accomplishing a full detector Monte Carlo and reconstruction of showers with the analysis procedure which is applied to experimentally recorded data, only showers with zenith angles $\leq 45°$ and core position well inside the array boundaries, were selected to derive the distributions shown in figure 7.2 [105, 8].
Due to the fact that the core location uncertainty is only known statistically rather than on an event by event basis, and due to its dependency on primary energy, it is necessary for any accurate analysis to group events into bins of energy and zenith angle, for which a core location correction can be applied. When grouping data into bins, it is important to consider all events including such for which the recorded signal density was zero. Note that zero density measurements are sensible whereas showers of zero energy are not. The latter would have to exist if densities are converted into energy before grouping events into bins. Therefore, the approach presented in figure 7.1 needs to be slightly modified.

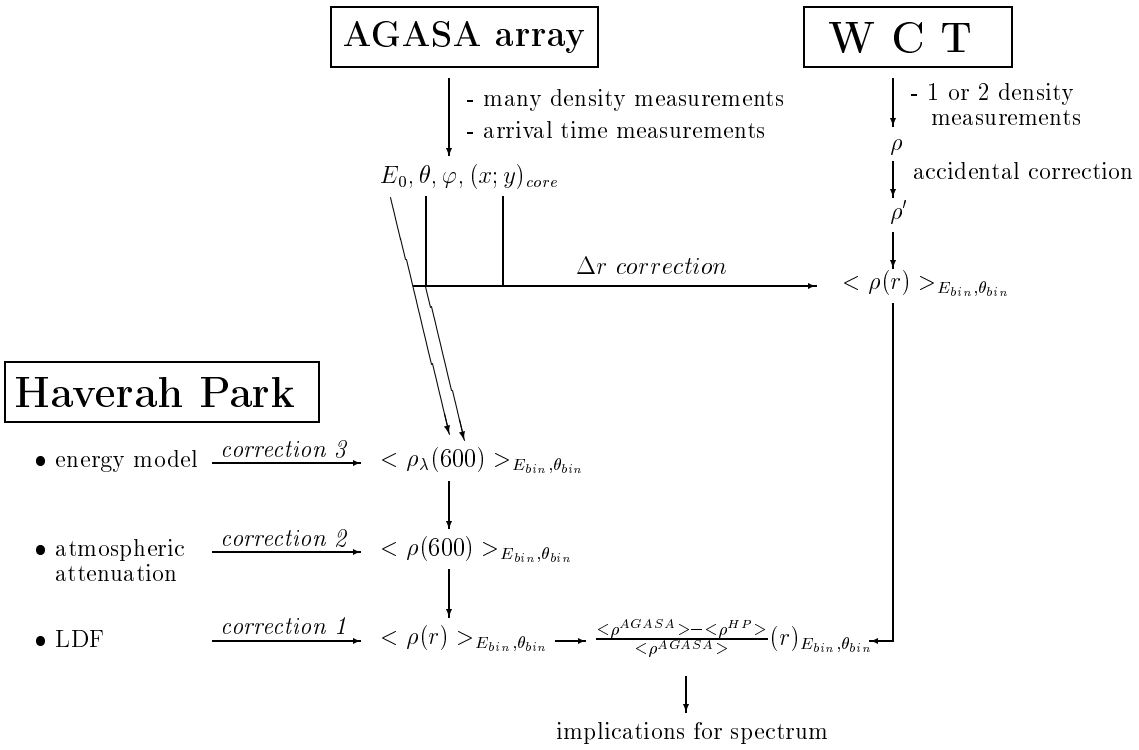

Figure 7.3: *Flow diagram of analysis procedure to cross calibrate water Cherenkov and scintillation detectors by means of density comparison.*

The modification is presented in figure 7.3 which outlines the principal method of the analysis pursued in this work. The approach makes use of the near proportionality between primary energy and $\rho_\lambda(600)$, the water Cherenkov signal density of a vertical shower at 600 m core distance; the density to primary energy conversion was described by $E_0 = \mathrm{C} \cdot \rho_\lambda(600)^\gamma$, where C indicates a constant and the density exponent γ was found to be 1.02±0.02 and 1.018 for AGASA and HP respectively (compare equation 4.4 and equation (3) in [104]). Therefore, a cross calibration performed by comparing energies is equivalent to the comparison of densities. The event binning is based on shower energies and zenith angles as estimated by AGASA with lower and upper bin limits defined according to $(18.0 + 0.2 \cdot (i-1))\,\mathrm{eV} < \log(\mathrm{E}) \leq (18.0 + 0.2 \cdot i)\,\mathrm{eV}$, with $1 \leq i \leq 3$ and $(j-1) \cdot 15^\circ \leq \theta < j \cdot 15^\circ$ with $1 \leq j \leq 3$. Per energy and zenith angle bin, the expected water Cherenkov signal density was determined as function of core distance according to the corrected Haverah Park energy conversion model and the LDF. Input parameters to this calculation were the AGASA mean mean energy and mean zenith angle per bin. Applied corrections are due to differences in atmospheric

attenuation effects and were described previously.
After grouping the experimental water Cherenkov densities as measured by the prototype detectors into logarithmic bins of core distance with bin upper limits defined as $r = 50 \cdot 10^{i/10}$ where $10 \leq i \leq 20$ and r is measured in meters, the averaged signal densities were corrected for background signals.

As the effects of core position uncertainty are distance dependent, a correction factor was calculated for individual core distance bins in the following manner: For each water Cherenkov signal density measurement 20 core distances were determined by sampling 20 times from the core location uncertainty distribution appropriate to the energy of the event, and randomly adding or subtracting the sampled core location uncertainties Δr from the current event core distance r. r denotes the core distance based on the core location as determined by the AGASA and therefore inherits the core position error of the AGASA analysis. Then, Haverah Park parameterizations, adjusted for an observation level of 920 g/cm^2, were used to calculate the expected signal densities $\rho(r + \Delta r)$ for each of the 20 core distances. Since all bins in which experimental measurements saturated the FADC system were discarded from the analysis, effectively all experimentally recorded signals were below a core distance dependent threshold corresponding to the typical signal size of a saturated event. In order for the core location correction to be accurate, all calculated densities $\rho(r+\Delta r)$ must also be smaller than the corresponding distance dependent saturation threshold. Should the occasion arise that calculated density values $\rho(r + \Delta r)$ would not meet the saturation criterion, Δr would be re-sampled until $\rho(r + \Delta r)$ would be in the allowed range for all 20 events. Subsequently, the mean density of all these artificially created events ($20 \times n$, where n is the number of experimental measurements per bin) is calculated relative to the expected density at the core distance of the bin center. The obtained value for $\frac{<\rho(r+\Delta r)>}{\rho(r_{\mathrm{bincenter}})}$ is used to correct the observed mean densities according to

$$< \rho_{\mathrm{corrected}} > (r) =< \rho_{\mathrm{observed}} > (r) \cdot \frac{\rho(r_{\mathrm{bincenter}})}{< \rho(r + \Delta r) >}(r) \tag{7.4}$$

It is claimed that the resulting density values $< \rho_{\mathrm{corrected}} > (r)$ are statistically corrected for effects induced by uncertainties in shower core locations.
The significance of this correction can be seen in figures 7.4, 7.5 and 7.4 which show the uncorrected (circles) and for core uncertainty corrected (triangles) mean water Cherenkov densities as function of core distance for three different energy regimes. Displayed errors for uncorrected data points are the standard error of the mean. The errors on the corrected mean signal density points are compiled from the standard error of the experimental mean and the sampled mean. The error originating from the sampling process is dominant and hence the errors on the data points increase

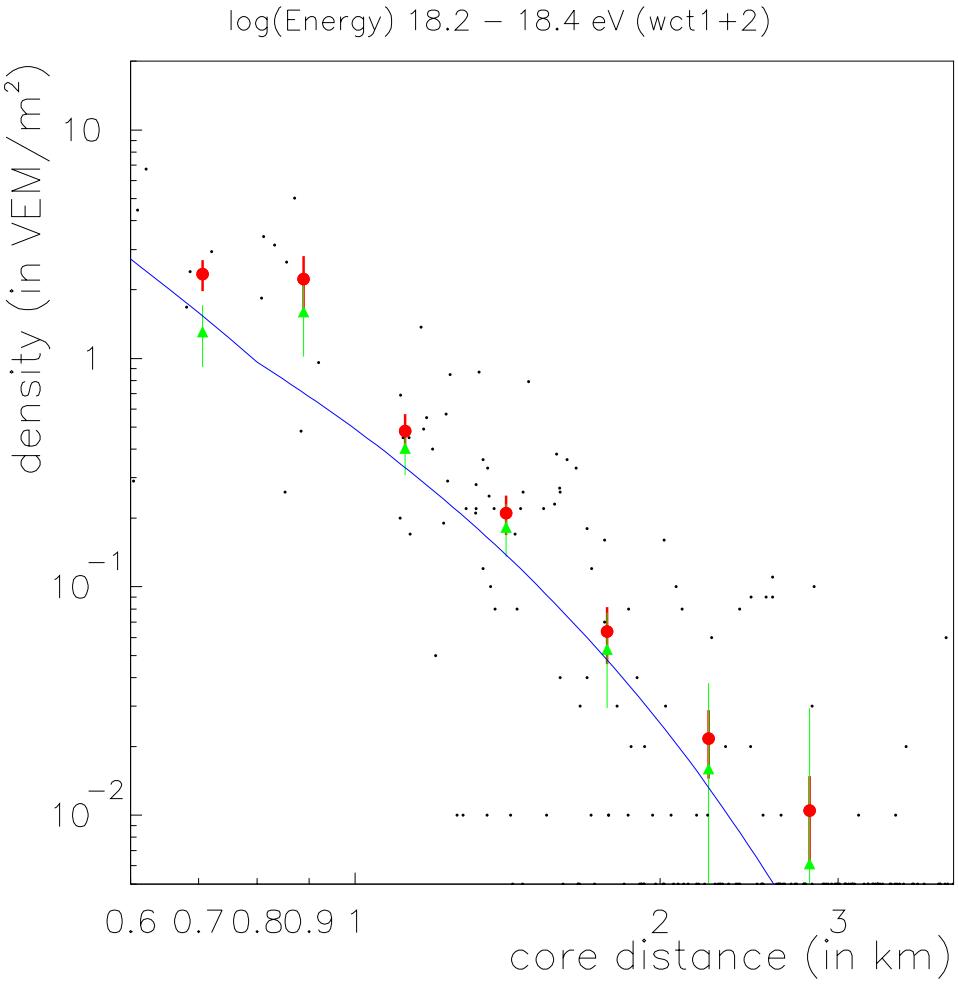

Figure 7.4: *Lateral distribution of water Cherenkov signal density as observed for showers with energies from $10^{18.2}$ to $10^{18.4}$ eV and with zenith angles between 15° and 30°. Continuous line, circles and triangles are expected, measured and for core uncertainty corrected densities.*

due to the fluctuation in the correction. Dots correspond to individual density measurements. In each figure the plotted curve represents the expected lateral distribution based on the Haverah Park parameterization adjusted to an observation level of 920 g/cm^2 and the mean AGASA energy and zenith angle of events contained in the displayed energy and zenith angle range. The energy ranges chosen as examples for graphical display are $18.0 < \log(E) < 18.2$, $18.2 < \log(E) < 18.4$ and $\log(E) > 18.6$ whereas the zenith angle range is the same for all three plots.

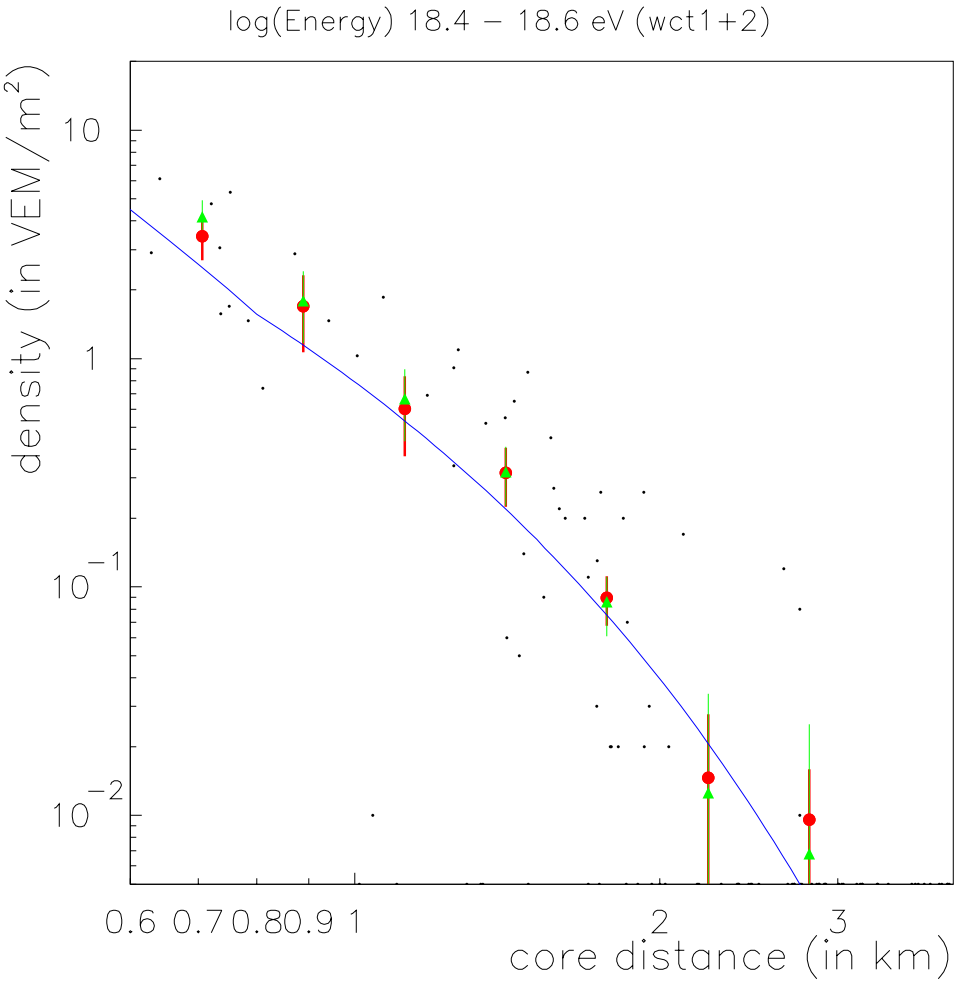

Figure 7.5: *Lateral distribution of water Cherenkov signal density as observed for showers with energies from $10^{18.4}$ to $10^{18.6}$ eV and with zenith angles between 15° and 30°. Continuous line, circles and triangles are expected, measured and for core uncertainty corrected densities.*

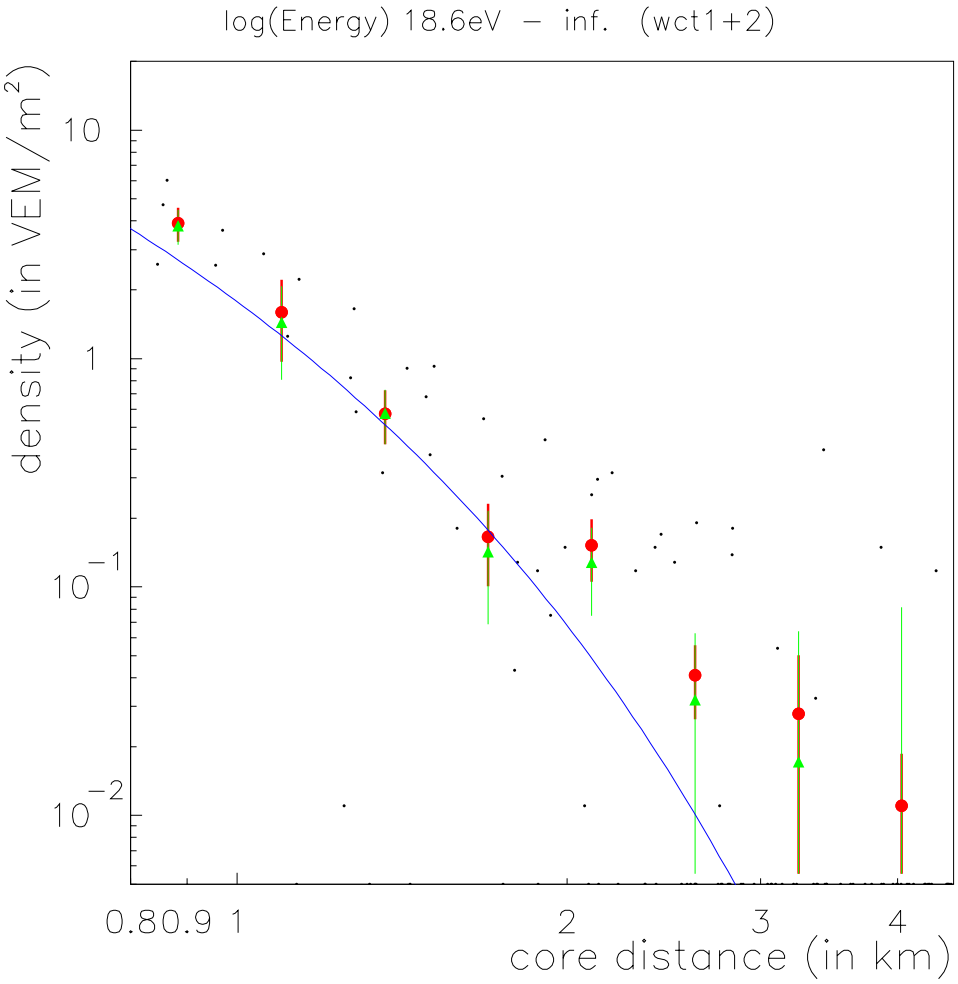

Figure 7.6: *Lateral distribution of water Cherenkov signal density as observed for showers with energies above $10^{18.6}$ eV and with zenith angles between 15° and 30°. Continuous line, circles and triangles are expected, measured and for core uncertainty corrected densities.*

For each bin in primary energy and zenith angle the logarithm of the ratio of measured to expected density $log(\rho_{\mathrm{measured}}/\rho_{\mathrm{expected}})$ was determined as function of core distance. The values are equal to the logarithm of the ratio of water Cherenkov based energy estimate and AGASA energy estimate. Since the energy dependence of η and hence the energy dependence of the shape of the LDF is weak, the ratio of $\rho_{\mathrm{measured}}/\rho_{\mathrm{expected}}$ is in good approximation equal to the corresponding ratio of densities $\rho_{\mathrm{measured}}(600)/\rho_{\mathrm{expected}}(600)$ at 600 m core distance. The latter is proportional to the ratio of primary energies as was pointed out earlier. Equation 7.5 illustrates the path along which the conversion from density to primary energy is established:

$$log\left(\frac{\rho_{\mathrm{measured}}}{\rho_{\mathrm{expected}}}\right) \approx log\left(\frac{\rho_{\lambda,\mathrm{m}}\,(600)}{\rho_{\lambda,\mathrm{ex}}\,(600)}\right) = log\left(\frac{E_{0,\mathrm{m}}^{\mathrm{HP}}}{E_{0,\mathrm{ex}}^{\mathrm{AGASA}}}\right). \tag{7.5}$$

Results are indicated in table 7.1. The small numbers next to the $\Delta log(\rho)$ entries in table 7.1 indicate the number of events per E_0, θ and r bin included to derive the logarithmic density differences. A certain number of events caused the FADC system to saturate. This happens preferentially at small core distances where particle densities are large. All bins in which saturated events occurred were eliminated from the analysis as the signal of the remaining events is likely to be smaller than the actual average signal because of the failure to record most upward fluctuations. Corresponding fields in table 7.1 are marked as "$sat(urated)$". The column last but one specifies the mean logarithmic differences $< \Delta\log(\rho) >$ per energy and zenith angle bin and was calculated as

$$\frac{\sum_{i=1}^{k} \Delta\log\rho(\mathrm{r}_i) \cdot n_i \cdot \rho_i}{\sum_{i=1}^{k} n_i \cdot \rho_i}, \tag{7.6}$$

where k indicates the number of core distance bins, ρ_i is the measured mean density and n_i represents the number of events per energy, zenith angle and core distance bin. The last column indicates the mean logarithmic deviations after additional averaging over all zenith angle ranges. Each range was weighted by the number of contained events.

log(E) [E in eV]		Θ_{min}	Θ_{max} [°]		$\Delta\log(\rho)(r) = \log(\rho_{measured}/\rho_{expected})(r)$								$<\Delta\log(\rho)>$	
min	max			r	561.009	706.269	889.14	1119.36	1409.19	1774.07	2233.42	2811.71		
18.0	18.2	0	15		-.043 $_{7}$	0.289 $_{4}$	-.042 $_{13}$	-.086 $_{10}$	0.073 $_{14}$	0.319 $_{15}$	-.117 $_{20}$	0.000 $_{16}$	.054	
		15	30		*sat.*	-.082 $_{21}$	-.042 $_{25}$	0.055 $_{30}$	0.153 $_{65}$	0.226 $_{68}$	0.046 $_{74}$	0.551 $_{76}$	.014	.054
		30	45		*sat.*	*sat.*	0.073 $_{31}$	0.121 $_{45}$	-.003 $_{49}$	0.189 $_{71}$	0.192 $_{74}$	0.751 $_{83}$	.095	
18.2	18.4	0	15		-.258 $_{2}$	-.120 $_{3}$	0.012 $_{6}$	0.213 $_{5}$	0.025 $_{18}$	0.301 $_{9}$	0.063 $_{2}$	0.810 $_{13}$	-.029	
		15	30		*sat.*	-.100 $_{3}$	0.296 $_{8}$	0.052 $_{14}$	0.138 $_{27}$	0.020 $_{33}$	0.086 $_{31}$	0.316 $_{43}$	.146	.075
		30	45		*sat.*	*sat.*	-.110 $_{19}$	0.206 $_{20}$	0.028 $_{29}$	0.044 $_{41}$	0.130 $_{45}$	0.437 $_{42}$	.051	
18.4	18.6	0	15		*sat.*	-.008 $_{1}$	-.032 $_{2}$	0.048 $_{2}$	0.087 $_{4}$	-.030 $_{6}$	0.284 $_{4}$	0.479 $_{8}$	.012	
		15	30		*sat.*	*sat.*	-.032 $_{3}$	-.054 $_{8}$	0.117 $_{15}$	-.022 $_{20}$	-.311 $_{13}$	0.068 $_{22}$	.010	.026
		30	45		*sat.*	-.111 $_{9}$	-.109 $_{6}$	0.179 $_{16}$	0.250 $_{11}$	0.228 $_{18}$	0.169 $_{25}$	0.705 $_{32}$	.040	
18.6	∞	0	15		*sat.*	0.000 $_{0}$	-.409 $_{2}$	-.151 $_{1}$	0.030 $_{2}$	0.294 $_{3}$	0.291 $_{6}$	0.341 $_{3}$	-.094	
		15	30		-.529 $_{2}$	0.000 $_{1}$	-.038 $_{5}$	*sat.*	0.007 $_{11}$	-.119 $_{8}$	0.427 $_{11}$	0.472 $_{24}$	.016	-.041
		30	45		*sat.*	*sat.*	-.788 $_{2}$	-.328 $_{10}$	-.072 $_{9}$	-.165 $_{14}$	0.480 $_{22}$	0.473 $_{20}$	-.072	

Table 7.1: *Logarithmic differences between measured and expected densities as function of core distance. The data have been binned into (logarithmic) bins of primary energy and zenith angle.*

7.1 Analysis of experimentally recorded signal densities

One characteristic which is common to all energy and zenith angle ranges is the increase of the discrepancy between measured and expected densities $\Delta\log(\rho)$ with growing core distance. This increase is shown graphically in figure 7.7 for showers with energies and zenith angles in the range $10^{18.0}$ to $10^{18.2}$ eV and 15° to 30°, respectively. The large discrepancies distant from the shower core are partly due to Poisson fluctuations in the sampling of the shower front. As can be seen from figure 7.4, densities at core distances beyond 1.5 km range around 5 VEM/10 m^2 and smaller. Beyond 2.5 km shower front particle densities amount to less than about 0.1 VEM per 10 m^2 for showers of energy below $10^{18.6}$ eV; since the sensitivity of the 10 m^2 water Cherenkov detector is about 0.1 VEM, events in the core distance bin around 2.8 km were not considered further for the analysis of events with primary energies below $10^{18.6}$ eV. However, at the highest energies, densities are expected to be accurately measurable out to distances of about 3 km; as a consequence events with energies above $10^{18.6}$ eV and core distances around 2.8 km will be considered for analysis. At core distances smaller than 1 km the observed densities are on average smaller than expected on the basis of the AGASA energy estimate. For events with energies up to $10^{18.6}$ eV this difference amounts to about 15% on average. As core distances in the range from 600 m to 1 km are used to estimate the shower energy, a direct consequence of this observation is that energies below $10^{18.6}$ eV as determined by AGASA are higher by about 15% in comparison to the HP energy estimates. No clear dependence of $\Delta\log(\rho)$ on zenith angle was detected. It is however noteworthy that the largest discrepancies between measured and expected densities occur at large zenith angles. This might be an indication that the attenuation length λ_{Akeno} has been underestimated; the reasoning leading to this conclusion is detailed as follows:

1) The expected density is derived from the AGASA energy estimate according to:

$$E_{\text{AGASA}} \rightarrow \rho_\lambda(600) \rightarrow \rho(600) \rightarrow \rho(r)$$

The step of interest is the conversion from $\rho_\lambda(600)$ to $\rho(600)$ by multiplication of $\rho_\lambda(600)$ with the attenuation factor f, defined as: $f = e^{-\frac{920}{\lambda}\cdot(sec\,\theta - \frac{1018}{920})}$.

2) For $30° \leq \theta \leq 40°$ the expression in parentheses is always positive so that

- larger values for λ imply larger values for f,

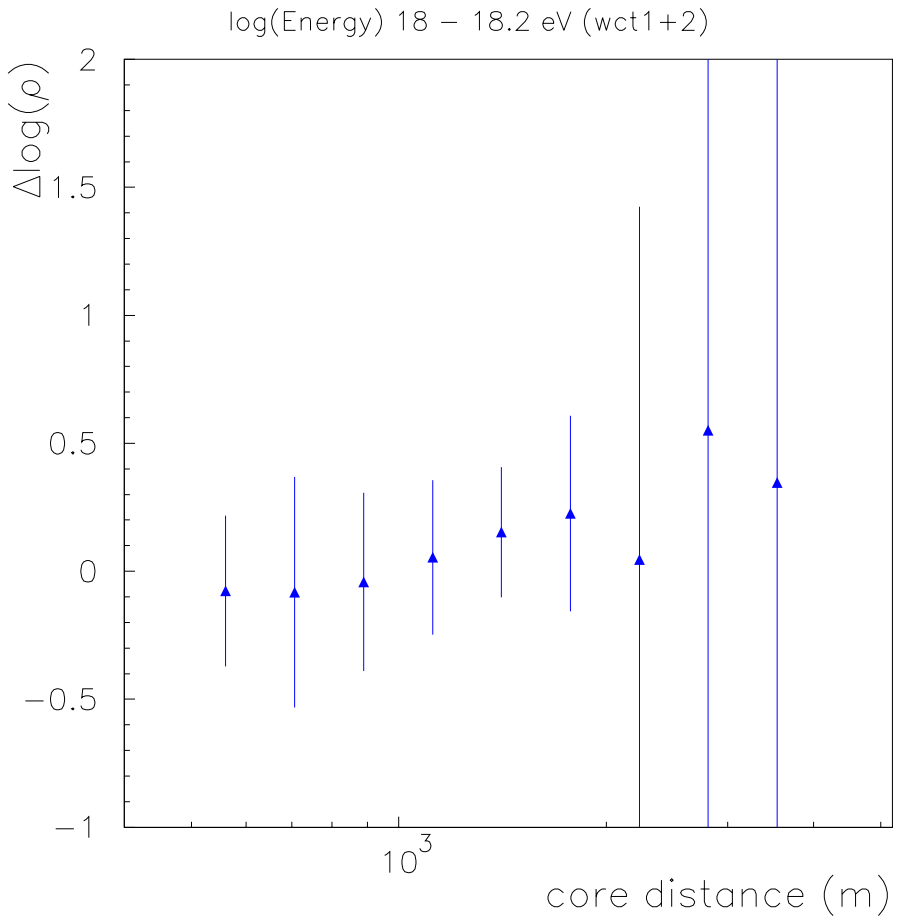

Figure 7.7: *Logarithmic difference between expected and measured densities as function of core distance. Expectations are based on the AGASA energy estimate and HP energy conversion model. Experimental measurements originate from water Cherenkov prototype detectors at AGASA. The error bars are the standard errors of the corrected experimental mean (e.g., see figure 7.4) divided by the expected mean density.*

log(E) [E in eV]		Θ_{min}	Θ_{max} [in °]		Δ log(ρ)		
min	max			λ	850	1000	1200
18.0	18.2	0	15		.054	.060	.067
		15	30		.014	.014	.015
		30	45		.095	.088	.080
18.2	18.4	0	15		-.029	-.034	-.039
		15	30		.146	.148	.151
		30	45		.051	.043	.041
18.4	18.6	0	15		.012	.013	.014
		15	30		.010	.012	.010
		30	45		.040	.025	.023
18.6	∞	0	15		-.094	-.118	-.128
		15	30		.016	.017	.020
		30	45		-.072	-.085	-.095

Table 7.2: *Mean logarithmic differences for core distances from 500 m to 2.8 km between expected and observed densities as function of primary energy, zenith angle and attenuation length.*

– smaller values for λ imply smaller values for f.

Therefore, larger values of λ are expected to bring expectations and measurements at large zenith angles into better agreement. At small zenith angles the effect is opposite but negligible because of small values for $(sec\,\theta - 1018/920)$. As was mentioned earlier, a variation of λ between 760 and 900 g/cm^2 is expected to have a 6% effect on derived densities. If even larger values for λ are assumed, the fluctuations Δlog(ρ) at large zenith angles become smaller. Mean discrepancies between expected and measured densities have been calculated for attenuation lengths λ equal to 850, 1000 and 1200 g/cm^2 and are presented in table 7.2. Attenuation lengths around 1000 g/cm^2 cause the discrepancies between measured and expected densities to fall below the 25% level for all zenith angles.

In the regime of the most energetic events (E $\geq 10^{18.6}$ eV) two striking properties can be observed:

i) At core distances less than 1.2 km the observed densities are consistently lower than the expected values.
The number of detected events is small and hence the numbers are subject to

large fluctuations; however, if only bins with more than 5 events are considered the measured density is lower than expected by 10% to 50%.

ii) At core distances beyond 2 km the reverse effect can be observed: $\Delta\log(\rho)$ becomes positive and more so, the discrepancies are larger and more systematic than at lower energies. The effect is too systematic for it to be caused by upward density fluctuations from the sampling process.

At energies above $10^{18.6}$ eV the observed average lateral distribution seems thus flatter than the LDF expected from the Haverah Park results. An attempt was made to quantize the degree of flattening by fitting a curve based on the HP parameterization of the lateral distribution to the data points in each zenith angle bin. A fit parameter $p1$ has been introduced to the HP parameterization according to:

$$\eta = 2.2 - 1.29 \cdot \frac{920}{1018} \cdot (sec\,\theta - 1) + 0.165 \cdot log\left(\frac{E}{10^{17eV}}\right) + p1. \qquad (7.7)$$

$p1$ was allowed to vary freely in order to obtain the best match between the data and the modified HP-LDF. Although better agreement at large core distances could be achieved, the overall agreement between data and parameterized LDF did not improve due to increased discrepancies at small core distances. Note that the subsample of events under investigation is constraint by only a lower limit in energy and that events range over about 1.5 decades in primary energy which has impact on the average shape of the LDF. No attempt was made to allow a fit with more degrees of freedom, as the resulting parameterizations would lack reliability due to limited statistics of the currently available data sample.
If the indication of an LDF-flattening above $10^{18.6}$ eV is true the core distance at which individual events are recorded, will have impact on the energy estimation: Small and large core distances would yield smaller, and respectively larger energies in comparison to what is observed by AGASA. Therefore it is difficult to quantize the average agreement between AGASA and water Cherenkov based energy estimates. The current data set indicates differences as large as - 60% at small core distances and differences of up to a factor of $\sim$2.5 for events recorded at large core distances.

7.2 Simulation of the water Cherenkov signal LDF

Air shower simulations have been carried out with the simulation code MOCCA by M. Hillas [76] in combination with the hadron interaction model Sibyll [97, 98].

Shower energies and zenith angles have been chosen to match a subset of showers observed with the water Cherenkov prototype detectors at AGASA. For the following study only primary protons have been simulated to create a ground particle list at 920 g/cm^2, the observation level of the AGASA experiment. The next step consists of sampling the simulated ground particles with a 10 m^2 water Cherenkov detector at a series of core distances out to about 4 km. The detector simulation has been carried out using the AGASim [81] code. Subsequently showers are grouped into bins of primary energy with the previously described bin limits; no zenith angle binning was used. Per energy bin the average water Cherenkov signal density was calculated as a function of core distance.
The lateral distribution of water Cherenkov signal density as derived from simulations is displayed in figure 7.2 for the energy range $10^{18.0}$ – $10^{18.2}$ eV (top) and above $10^{18.6}$ eV (bottom), respectively. The large triangles represent the simulation results. Experimental data are plotted as points (uncorrected) and for core position uncertainty corrected data are shown as small triangles. Error bars were calculated as in figure 7.4 and dots correspond to individual EAS measurements. The curve represents the LDF as expected from results of the Haverah Park experiment and the mean energy and zenith angle of the data sample.
For the low and high energy range the simulation results suggest a larger water Cherenkov signal density at core distances beyond 2 km than expected from the Haverah Park based prediction. However, the effect seems to be more pronounced for the energy regime above $10^{18.6}$ eV, for which measurements can be made out to core distances of $\sim$3.5 km. It will not be attempted to quantify the discrepancy between simulations and expectations because the hadron interaction model Sibyll which was used for the simulations, was reported to be faulty after the EAS simulations had been carried out. The muon content is supposedly to high by as much as 20%. It is not clear whether this effect is muon energy dependent and whether it has any impact on the muon lateral distribution on ground level. However, it is remarkable that the simulations also show, at least qualitatively, a flattening of the water Cherenkov signal LDF at large core distances and high energies.

7.3 Energy estimation and cross-calibration of the most energetic events

Despite the fact that the core location uncertainty in the AGASA analysis cannot be corrected for on an event by event basis, an attempt was made to cross calibrate the

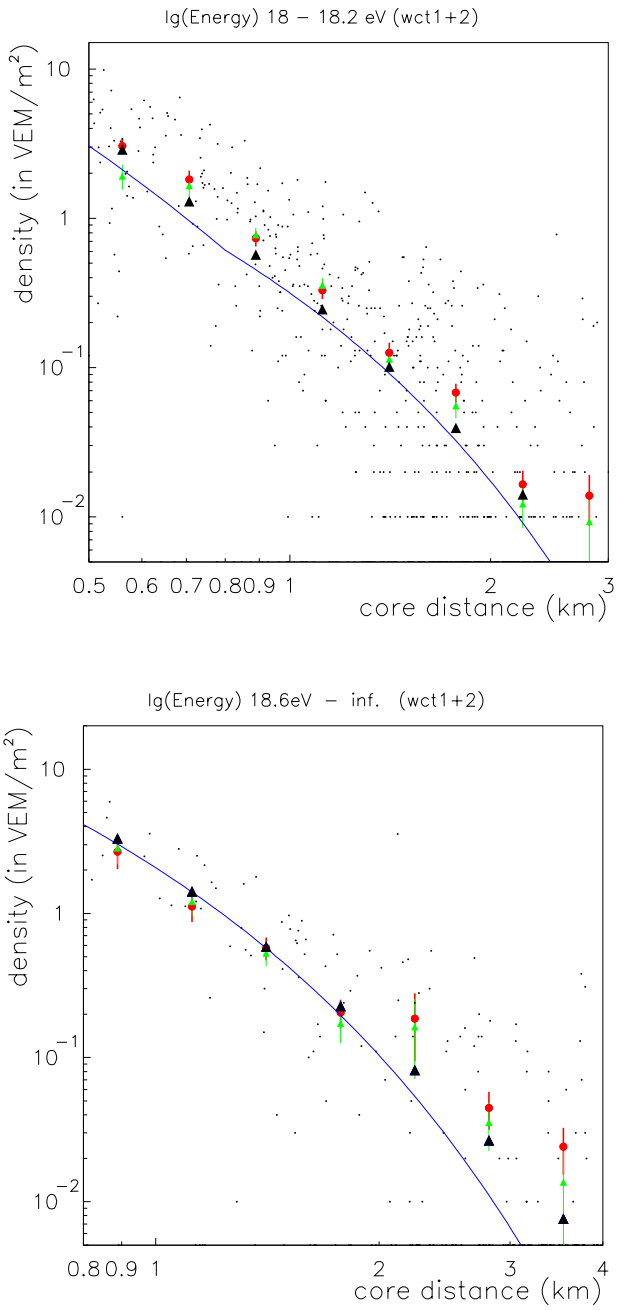

Figure 7.8: *The lateral distribution as measured with the water Cherenkov prototype detectors is shown along with the expected LDF based on results from the Haverah Park experiment (continuous line) and simulation results (large triangles). The points and small triangles are raw and for core location uncertainty corrected data. The top and bottom figure correspond to the energy range $10^{18.0}$ – $10^{18.2}$ eV and the range above$10^{18.6}$ eV, respectively.*

HP and AGASA energy estimation techniques by use of individual events. As the core location uncertainty decreases with increasing energy only events with AGASA energies above 9×10^{18} eV were selected. This data subset was further constraint to events with core distances less than 2.3 km and water Cherenkov signals larger than 0.1 VEM/m^2. These selection criteria were chosen in order to minimize Poisson fluctuations induced by the sampling process of the shower front. For energies around 10^{19} eV signal densities around 2 km are expected to be of the order of 1 VEM.
For the remaining 16 events the shower energy was estimated on the basis of the water Cherenkov signal density measurement and the HP energy model as described earlier. The obtained energies were directly compared to the energy estimates from the AGASA analysis. Figure 7.9 shows the AGASA energy estimates as function of the water Cherenkov energy estimates for all 16 events. The square marker corresponds to the mean of 63 events with WCD signals larger than 0.1 VEM/m^2, core distances smaller than 2.3 km and AGASA energies in the range from 4×10^{18} eV to 9×10^{18} eV. The continuous and broken lines indicate equal energy estimation by both techniques and the $\pm15\%$ deviation from equality. The agreement of AGASA and WCD based energies is poor. Despite the scatter of some events around the line of equal energy estimates, the WCD based energy estimates are systematically too high in comparison with the AGASA energies. As the uncertainty in core location causes the distance of the water Cherenkov detector from the shower core to fluctuate symmetrically towards smaller and larger distances it is unlikely that this uncertainty is the cause for the observed systematic shift in WCD based energy estimates. However, next to fluctuations from the shower front sampling process this uncertainty is likely to be the origin of the observed scatter in energy estimates for a minority of events.
In the previous section, the average lateral distribution of ground particles for showers with energies above $10^{18.6}$ eV was found to be flatter than suggested by the Haverah Park parameterization. This result is qualitatively incorporated in the analysis of the 16 event-data subset. The flattening of the lateral distribution was achieved by introducing a negative E^2 dependence to η, the exponent of the LDF in the HP representation. Best agreement between AGASA and water Cherenkov based energy estimates was achieved for:

$$p1 = -0.15 \cdot log^2\left(\frac{E}{10^{17eV}}\right). \tag{7.8}$$

with $p1$ being the fit parameter introduced in equation 7.7. Figure 7.10 displays the AGASA energies as function of the energy estimates based on the water Cherenkov signal measurements and the Haverah Park LDF with modified shape. The agreement between the different energy estimates is good. If individual and largely scattered events, presumably caused by uncertainties in core location and sampling

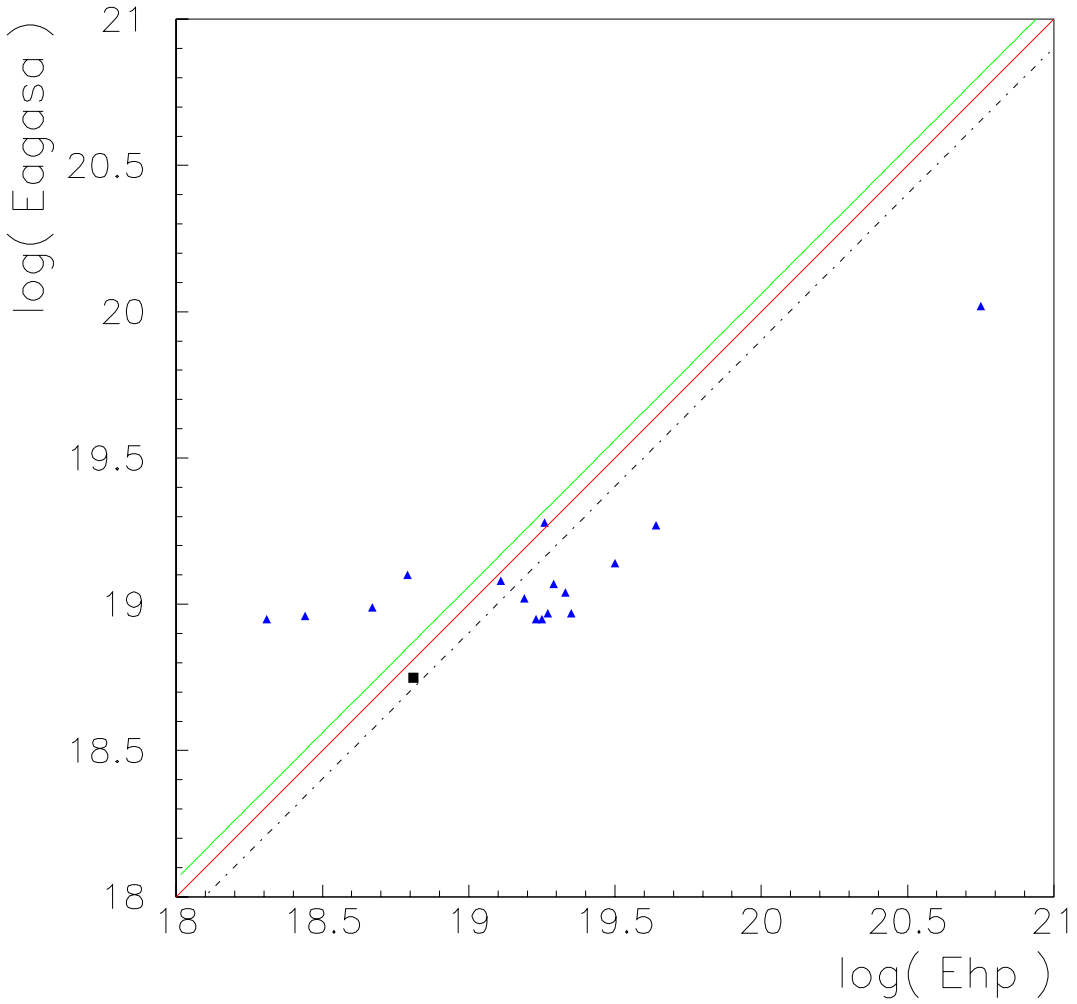

Figure 7.9: *Plotted are energies as estimated by the AGASA analysis versus energy estimates based on the HP energy model and water Cherenkov prototype measurements at AGASA. Each triangle corresponds to an individual event with AGASA energy above 9×10^{18} eV, a water tank signal larger than 1 VEM per 10 m^2 and core distance smaller than 2.3 km. The square represents the mean value of events with energies between 4×10^{18} eV and 9×10^{18} eV and water Cherenkov signal density and core distance conditions as above.*

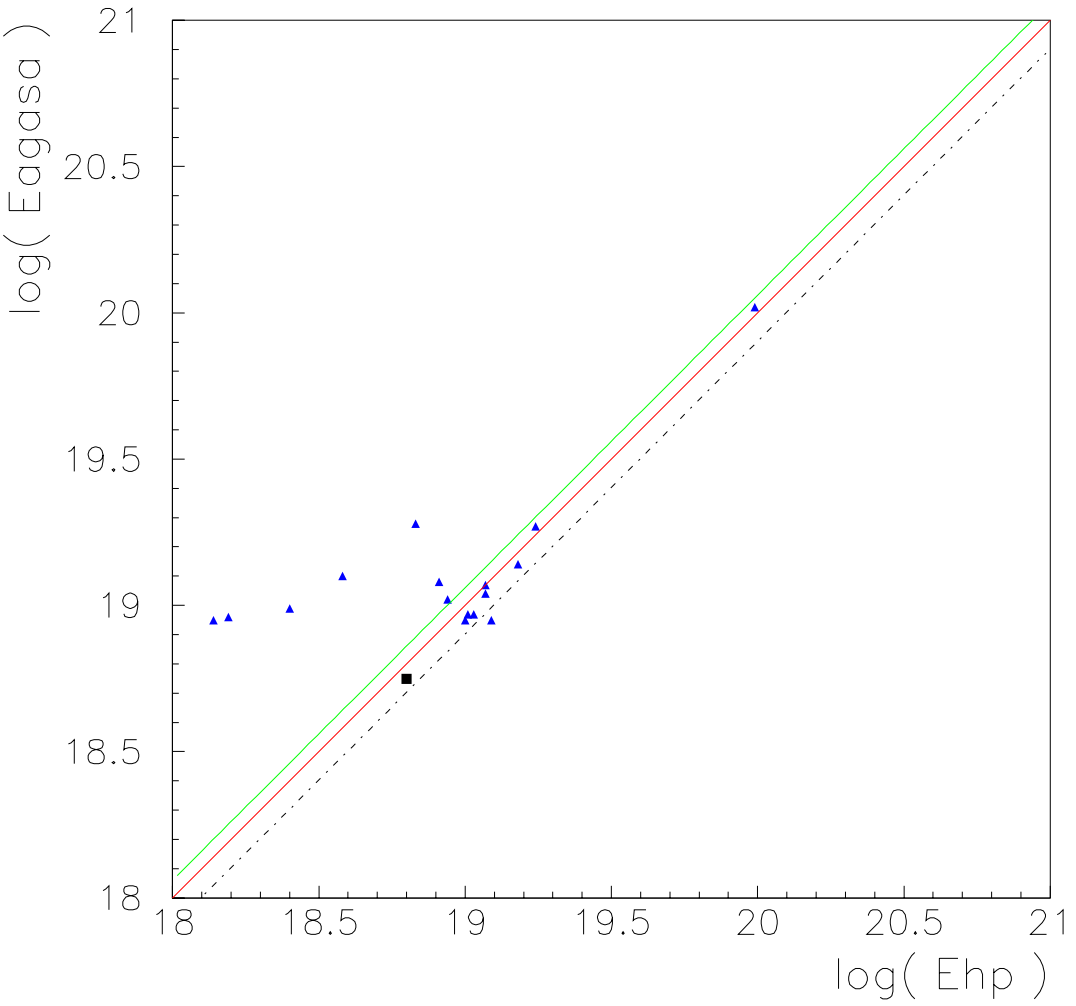

Figure 7.10: *Plotted are energies as estimated by the AGASA analysis versus energy estimates based on water Cherenkov prototype measurements and the HP energy model. An energy dependent flattening of the LDF was introduced by an additional E^2 dependence of the LDF exponent η. Each triangle corresponds to an individual event with AGASA energy above 9×10^{18} eV, water tank signal larger than 1 VEM per 10 m^2 and core distance less than 2.3 km. The square represents the mean value of events with energies between 4×10^{18} eV and 9×10^{18} eV and signal density and core distance conditions as above.*

fluctuations, are ignored the energy estimates agree with each other to within 15%. The events to the far left in figure 7.10 have either very small signal densities (¡ 1.4 VEM/m^2) and hence are subject to large sampling fluctuations or were observed at core distances of about 1.2 km. As was pointed out earlier, at small core distances uncertainties in core location have significant effects on the energy estimation. The same argument applies to the two events which lie just outside, to the left and right, of the 15% boundaries of equal energy estimates. These events with water Cherenkov energies of $10^{18.91}$ and $10^{19.09}$ were recorded at core distances of 1.2 and 1.1 km, respectively. All other events were observed at core distances in the range from 1.3 to 2.3 km were the sum effect of core location uncertainties and sampling fluctuations is minimal on average.

An agreement between the AGASA and water Cherenkov based energy estimates in the energy regime above 9×10^{18} eV can be achieved to within 15%, if the lateral distribution function of water Cherenkov signal densities is assumed to be flatter for the most energetic air showers than indicated by the published Haverah Park result [75]. The lateral distribution function published by the Haverah Park group steepens with increasing energy according to $r^{-log(E_0/10^{17})}$. The modification which brings the AGASA and water Cherenkov signal based energy estimates into good agreement introduces a $r^{-log^2(E_0/10^{17})}$ dependence of η, which means that for air showers with energies above 4×10^{18} eV, the lateral distribution steepens at a lower rate with increase in primary energy than in the energy range from 4×10^{17} eV to 4×10^{18} eV. This corresponds to a relative flattening of the LDF with increasing primary energy. The parameterization of η as expressed in equation 4.2 was established for data recorded in the energy range between 4×10^{17} eV and 4×10^{18} eV. It is furthermore known from results from the Fly's Eye detector [12] that the composition of cosmic rays changes within this energy range from "heavy" to "light", that is from iron dominated to proton dominated. Therefore, the steepening of the lateral distribution function with increasing energy, as specified by the Haverah Park experiment and expressed by equation 4.2 is a manifestation of two effects:

1) an increase of primary energy

2) a change in composition towards lighter nuclei

Both effects cause the maximum shower development $X_{\max}$ to occur deeper in the atmosphere and hence cause steeper lateral distributions. Since it is extremely unlikely that the change of composition takes place over more than one decade in energy, a decrease of the rate of LDF steepening with increasing primary energy is expected for energies above $\sim4\times10^{18}$ eV. The derived expression for the flattening of η with increasing energy can only be regarded as an indication. Statistics of the

present data set is too limited to quantitatively indicate the flattening of the lateral distribution function of water Cherenkov signal density. However, at energies above 4×10^{18} eV qualitative indications for a weaker energy dependence of the LDF exponent η than suggested by the HP results for the energy range from 4×10^{17} eV to 4×10^{18} eV exist.

7.4 Comparison of the Haverah Park and AGASA energy spectra

When comparing cosmic ray spectra it is common to look at the differential flux J multiplied by E^3 as features in the spectrum are emphasized and differences between measured spectra are more apparent. A variation of this representation was chosen: The AGASA and Haverah Park spectra are each compared to a standard spectrum J_S as a direct comparison by plotting the two spectra on top of each other does not allow to see any details due to large error bars. The standard spectrum J_S has been adopted from [10] where it is defined as

$$J_S = 3.84 \times 10^{24} E^{-3} \mathrm{m}^{-2}\mathrm{s}^{-1}\mathrm{sr}^{-1}\mathrm{eV}^{-1} \ . \tag{7.9}$$

It has been normalized to the Haverah Park data point at an energy of $\sim 6\times10^{17}$ eV which has a statistical uncertainty of about 4% [10]. Figure 7.11 shows the fractional deviation $D = (J/J_S - 1)$ of the differential intensity, J, from the standard spectrum for the AGASA [7, 8] and Haverah Park [10] spectra. The number of events included in the highest energy data points are indicated. In the energy regime up to $10^{18.6}$ eV it is apparent that the differential flux J times E^3 as determined by AGASA is larger than the corresponding Haverah Park values by about 40% to 55% for the energy range $18.0 < \log(\mathrm{E}) < 18.4$ and $18.4 < \log(\mathrm{E}) < 18.6$, respectively. Since for a number of given events with specified energies the flux determination for ground arrays is rather straight forward (due to their near constant aperture) it is assumed that the error in the differential flux $J(E)$ is dominated by the error in primary energy. A shift in primary energy towards smaller values would result in a left-downward shift of the data points in a JE^3 versus E representation of the spectrum (of which the fractional deviation representation chosen in figure 7.11 is one). The AGASA and Haverah Park differential fluxes can be brought into agreement by reducing the AGASA energies by 10% to 14% for the energy ranges $18.0 < \log(\mathrm{E}) < 18.4$ and $18.4 < \log(\mathrm{E}) < 18.6$, respectively. These results are in good agreement with the 15% energy difference found in the cross-calibration of energy estimates

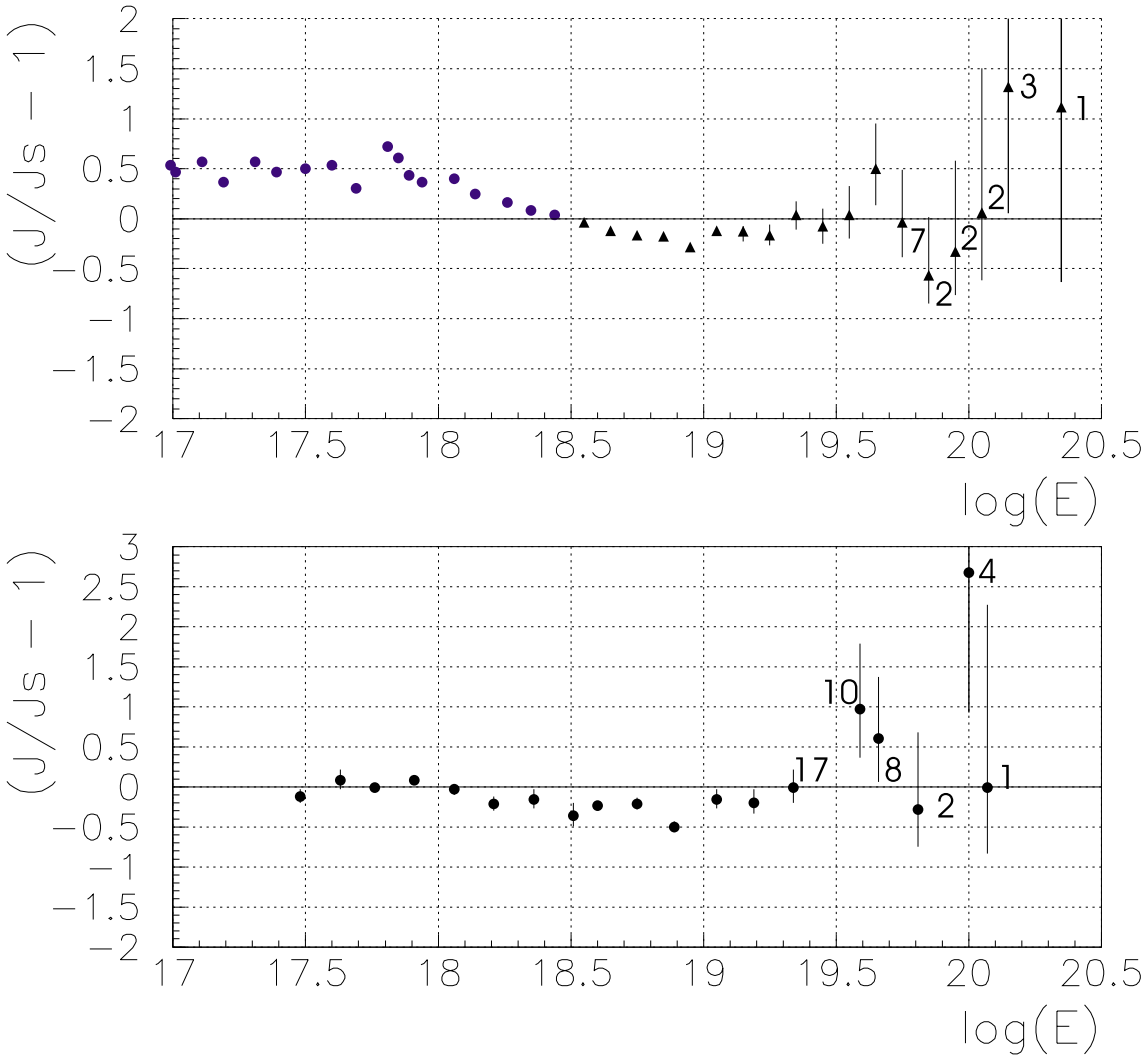

Figure 7.11: *Fractional deviation of the AGASA (top) and Haverah Park (bottom) spectra from the standard spectrum* J_S*. Circles and triangles in the AGASA spectrum correspond to data points taken from [7] and [8], respectively. The numbers next to the highest energy data points indicate the number of events included in the corresponding data point.*

by means of the Auger water Cherenkov detectors. (Equally, the Haverah Park energies could have been increased. However, the good agreement [10] between the Haverah Park spectrum and the Fly's Eye spectrum, which is based on observations of the longitudinal shower profile and has therefore superior calorimetric quality than results based on observations made by a ground array, lead to the above choice.) For energies above $10^{18.6}$ eV the situation is less clear. However, two regimes can be separated:

1) Between $10^{18.6}$ eV and $10^{19.3}$ eV AGASA and Haverah Park energy estimates are in good agreement. Energies just below $10^{19.3}$ eV were observed to agree to within 15% and energy estimates around the lower end of the range agree, on average, to within 25% despite the fact that at energies around $10^{18.9}$ eV the discrepancy is as large as 55%.

2) For the energy regime above $10^{19.3}$ eV Haverah Park energy estimates are found to be larger than the AGASA energies by up to about 60%. However statistics is very limited in the regime of the highest energy cosmic rays.

Chapter 8

Conclusions and Outlook

Two water Cherenkov prototype detectors for the Pierre Auger Observatories have been set up and operated within the Akeno Giant Air Shower Array (AGASA) since July 1996 and July 1997, respectively. These were used to study detector properties in response to background muons and signals originating from extensive air showers.

- Basic properties of the water Cherenkov prototype detectors were investigated and agreement with simulations has been demonstrated.

- Experience with the current detectors shows the design to be appropriate for observations at the highest energies. A water Cherenkov detector can be recommended as a basic and reliable detector unit for the Auger Observatories.

- They can be easily calibrated and monitored in situ without the need for auxiliary equipment.

- The separation of the muonic and electromagnetic components of EAS signals recorded by WCDs proved more difficult than initially expected due to a large background caused by stopping gamma-rays. The analysis approach chosen in the present study showed only modest muon separation capabilities and further work and development of suitable extraction mechanisms is needed.

- Although the shape, size and choice of materials for the prototype detectors at AGASA were chosen according to the design anticipated for the Auger detectors, the mechanical construction was not. However, from experience with the present construction of stainless steel pipes it is clear that the tanks will need a strong and durable container in order to withstand harsh environments for an extended period of time. This problem will be taken care of by installing

the Tyvek-lined PVC bag in either a rotomolded plastic or a stainless steel container.

- An open issue regarding the water Cherenkov detector design is the incorporation of a low gain channel, which would permit measurement of particle densities from EAS at small core distances without saturation.

- A decay of optical detector quality was observed. Although no cause was unambiguously identified it is most likely linked to the water quality. The preservation of the water quality remains to be investigated.

WCD data recorded in air showers were compared to the data observed by AGASA. Events reconstructed by AGASA, when combined with parameterizations provided by the Haverah Park WCD array, reproduce measurements of the water Cherenkov prototype detectors. Furthermore, the same type of air shower and detector simulations which showed agreement with data from the Haverah Park array [75] successfully reproduce observations by the water Cherenkov prototype detectors. Hence, the Haverah Park and Auger prototype detectors have similar properties. The latter were used to perform a relative energy cross-calibration between the AGASA and Haverah Park arrays. After adjustment of the HP parameterization to an atmospheric depth of 920 g/cm^2, the observation level of AGASA, energy estimates were found to agree within 15% at energies below 4×10^{18} eV and zenith angles smaller than 30°. For zenith angles in the range 30° to 45° an agreement to within 25% was found. This result is based on a conservative estimate for the attenuation of air showers across the array at 920 g/cm^2 as seen by the water Cherenkov technique. If, however, the attenuation length λ is assumed to be greater than or equal to 1000 g/cm^2 (instead of 850 g/cm^2), then for small angles the energy estimates agree to within 17% while at the larger angles it improves to about 20%. These results are in good agreement with the energy differences derived from the AGASA and Haverah Park spectra. In the energy range $10^{18.0}$ – $10^{18.6}$ eV the published spectra can be brought into agreement if an uncertainty of ∼15% in either of the two experiments' energy estimates is assumed. Although the spectra indicate systematically higher energy estimates by AGASA, the energy estimates based on the measurements with the prototype detectors do not show such a behavior. No domains of energy, zenith angle and core distance bin were identified for which the AGASA energy estimates are consistently greater than HP energy estimates or vice versa; the values fluctuate about each other within a limit of ∼15%.
At energies above 4×10^{18} eV, an energy domain for which it is not known whether the Haverah Park parameterizations hold true, the data at hand and simulations indicate a flattening of the lateral distribution relative to the HP parameterization.

However, due to limited statistics in the high energy regime, the degree of flattening was not described quantitatively. A comparison of the AGASA and Haverah Park spectra above $\sim 10^{19.3}$ eV shows the Haverah Park energies to be larger than the AGASA based energy estimates, which is in qualitative agreement with the result from the prototype detector based cross-calibration. Due to the very limited number of events recorded at the highest energies, this conclusion must be regarded as preliminary.

The good agreement between energy estimates by the water Cherenkov technique and by the scintillator array AGASA in the energy range $10^{18.0}$ – $10^{18.6}$ eV fosters confidence in both techniques and in their use in the detection of extensive air showers. The study at hand demonstrates the agreement of air shower measurements by ground arrays and thereby contributes to an increasing confidence in their results. It will be the task of future experiments such as the Pierre Auger Observatories to increase the number of observed events at energies above 10^{19} eV and to accurately measure the lateral distribution of particles arriving at ground level. From these data the cosmic ray spectrum can be determined with high statistics at energies around and above the predicted GZK-cutoff.

Appendix A

The Haverah Park Experiment

The Haverah Park array was operated at a location 220 m above sea level at 53° 58.2' N, 1° 38.2' W. The detectors consisted of a number of units of varying area built from water Cherenkov detectors modules. The modules were of two types. The majority, which were used throughout the experiment, were galvanized iron tanks 2.29 m^2 in area and filled to a depth of 1.2 m with water from a nearby bore hole in magnesium limestone. A minority of detectors, operated for four years, were 1 $m^2 \times$ 1.2 m water Cherenkov detectors constructed from expanded plastic foam, 5 cm thick; these tanks were filled with deionized water as the plastic construction lacked the zinc which is believed to have prevented fungoid growth in the galvanized metal tanks. All tanks were lined with a white diffusing plastic (ICI Darvic). The water in each tank was viewed with an EMI photomultiplier (type 9618YB) with 5 in diameter S11 Sb/CsO photocathode held so that it just dipped into the water. Detector areas larger than 2.29 m^2 were achieved by grouping together a number of the larger modules in huts with roofs having thicknesses less than 4 g/cm^2 [24, 25]. The arrangement of the detectors is shown in figure A.1. Detectors A1, ..., A4 (34 m^2) were operated from 1963 - 1987, detectors B,...,G (each 4 $\times$ 13.5 m^2) from 1968 - 1987, and detectors J,K and L were added in 1976 along with the "infilled" array of 30 $\times$ 1 m^2 detectors spaced at 150 m. While J,K and L were operated until 1987 the "infill" array ceased operation in 1981. During the operation of the array, 3 detectors of 9 m^2 each (A150) and one detector of 13.5 m^2 (H) were added and used from 1971 - 1987 and 1970 - 1984, respectively.

The array recorded air showers whenever A1 and any two of A2, A3 and A4 recorded a signal at least equivalent to that produced by 10 muons traveling vertically through a water depth of 1.2 m and within 4 μs. Data at the individual detector stations were recorded in various ways (see [10, 26] for details). Air shower directions were generally measured from the relative arrival times of the signals at A1,...,A4. The

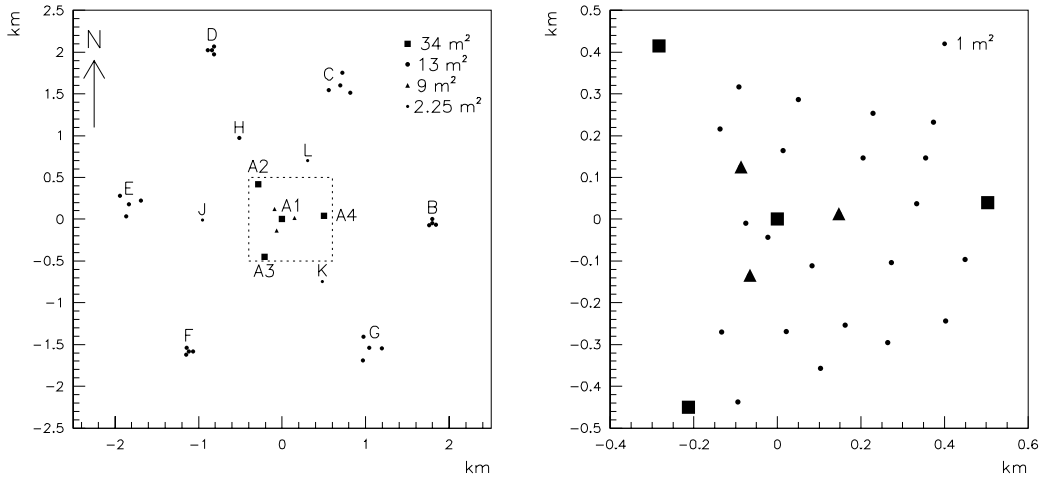

Figure A.1: *The Haverah Park air shower array. On the left the 12 km^2 array is shown; the areas of the various detector units are indicated by the key. The center area of the array (dotted square) is shown enlarged in the right plot where the detector positions of the infill array are indicated. [75]*

angular accuracy is well described by $\sigma_\theta = 2.5\,^\circ \cdot sec\,\theta$ and $\sigma_\Phi = 2.5\,^\circ \cdot csc\,\theta$. The primary energy of the cosmic ray was determined from a measurement of $\rho(600)$, the water Cherenkov signal density at 600 m from the shower axis (see section 4.2.2 and references therein).

A.1 The Haverah Park measurement of the lateral distribution function

The basic technique of air shower reconstruction from ground array data consists of finding the shower direction and successively estimating the shower size from the available pattern of signal amplitudes in the shower plane. It is standard procedure to fit an empirically determined average lateral distribution function (LDF) to the density pattern of hit detectors and derive a shower size parameter, typically the signal density at 600 m core distance, in order to obtain an estimate of the cosmic ray energy. As the number of hit detectors per shower is limited and the signal density measurements are subject to fluctuations, the importance of the fitted LDF's correctness is apparent: Errors in the shape of the LDF directly translate into uncertainties in shower energy estimation.

The first and most important task for determining an LDF is an accurate measurement of the shower core position on the ground. This is a difficult problem as it arises from the danger of a 'self-fulfilling prophecy' as was eloquently expressed by Linsley [99]. He pointed out that in order for the shower core to be determined independent of assumptions about the lateral distribution function it needs to be determined by a subset of 3 or 6 detectors of a regular array. Furthermore the spacing of such a regular array will significantly contribute to the accuracy with which the core position can be determined. The lateral distribution as specified in equation 4.1 was derived from data recorded with the infill array of 1 m^2 detectors. The core was located to within about 5 m by 3 or more ringing detectors, that is detectors surrounding the core of this densely spaced array. Once the core position was found, the lateral distribution function was derived from density measurements which were not used for the core position determination. This is to assure minimum correlation between the uncertainty in core position and the density measurements used to derive a lateral distribution function. The steep fall off of density values with increasing distance from the shower core suggests to describe the lateral distribution by a power law. An iterative method was adopted to find the best value for the exponent η of the lateral distribution function and no more than 6 iterations were needed to determine it to an accuracy of about 5 % [100, 101]. A multiple linear regression was used to determine the dependence of η on zenith angle and energy [101]. The result is indicated in equation 4.2. The flattening of the lateral distribution function at core distances beyond 800 m was determined in analogy to the method described above: On the basis of density measurements at core distances smaller than 800 m and the well established LDF up to 700 m, the shower core location was determined and the shower properties were characterized. Subsequently, data were binned versus core distance and a fit to the observations at core distances greater than 800 m lead to a parameterization (cf. equation 4.3) approximating the average LDF at large distances from the shower core [102, 75].

Appendix B

Measurement of the background rate

The Auger Observatory will record the majority of events with a surface array of water Cherenkov detectors. The array will trigger if a minimum number of individual detector stations have triggered and topological trigger conditions are met. The triggering of individual detectors occurs in two stages — so called level 1 and level 2 triggers. The level 1 trigger selects signals above a certain threshold; these are primarily due to electrons. The level 2 trigger discriminates against short (in time) and small (in amplitude) signals. The envisaged post trigger rates are $\leq$ 100 Hz and $\leq$ 20 Hz for level 1 and 2 respectively. This 2 staged trigger mechanism is expected to work efficiently for regular and neutrino initiated showers but, as was pointed out recently [107], might be problematic for hadronic showers at large zenith angles or simultaneous but separated showers. Highly inclined hadron initiated showers typically produce signals with time spreads of less than 50 ns [108] and would therefore be discarded by a level 2 trigger which demands that the signal be spread in time. As highly inclined hadronic showers contain interesting and valuable physics it is important to retain as many potential candidates of this event type as possible. The event rate can easily be increased by lowering the threshold on the signal size. In this context Watson [107] raised the question for what pulse size the observed event rate could be reduced to 20 Hz, the output requirement of the level 2 trigger. This work investigated this issue using data from the prototype detector at AGASA.

B.1 Recording of the data set

The first water Cherenkov detector at AGASA (WCT1; white top) was triggered by a regular pulser signal in order to record background data. It can be assumed that the trigger is totally independent of any air shower event and therefore the recorded signal traces can be used to estimate the integral background rate as function of signal size.
For each trigger a signal trace totaling 50 μs was recorded and saved to disc. The data rate was limited by the data acquisition system and on average a total of about 1.3 s of data were recorded per day. The entire data set of FADC traces totals a time of about 31 s.
For practical purposes it was decided to scan the data and to only keep all non-empty traces along with the values of the total time covered by all, that is empty and non-empty traces. These data are available via anonymous-ftp from *aupc1.uchicago.edu: auger/agasa/backgr* . A brief description of the scanning follows: For each trace of 50 μs the baseline was determined from the first 400 ns after assuring that no pulse occurred within this time range. Subsequently traces were corrected for baseline shifts and the sum trace of all three PMTs was scanned for the occurrence of signals. A trace was counted as empty if over the entire range of 50 μs no time bin showed a signal larger than 4 FADC bins. Typical baseline fluctuations for the sum trace (3 PMTS) were observed to range between 1 and 4 FADC bins. For comparison the size of an average muon signal totals about 17 FADC bins. Data were recorded at a sampling rate of 100 MHz and the recording range of the 8 bit FADC was set to 800 mV.

B.2 The analysis of random FADC traces

In the following the analysis procedure is described and results will be presented. The previously described data set is scanned for the occurrence of signals. The identification of signals is done by applying a threshold to the FADC trace and searching for FADC bins exceeding the threshold. The chosen value has to be small but must lie above the noise level of the FADC. Peaks are counted as individual if the separation between them is more than 300 ns. A 300 ns limit was chosen as small air showers are expected to have time spreads within this range. However, peaks are counted as one signal if their relative time separation is less than 300 ns. The identified signals have been integrated and the time in which the signals rises from 10% to 90% of it's total integrated charge value, the rise time $t_{10\%-90\%}$, has been determined. Figure B.1 shows the pulse size in units of vertical equivalent

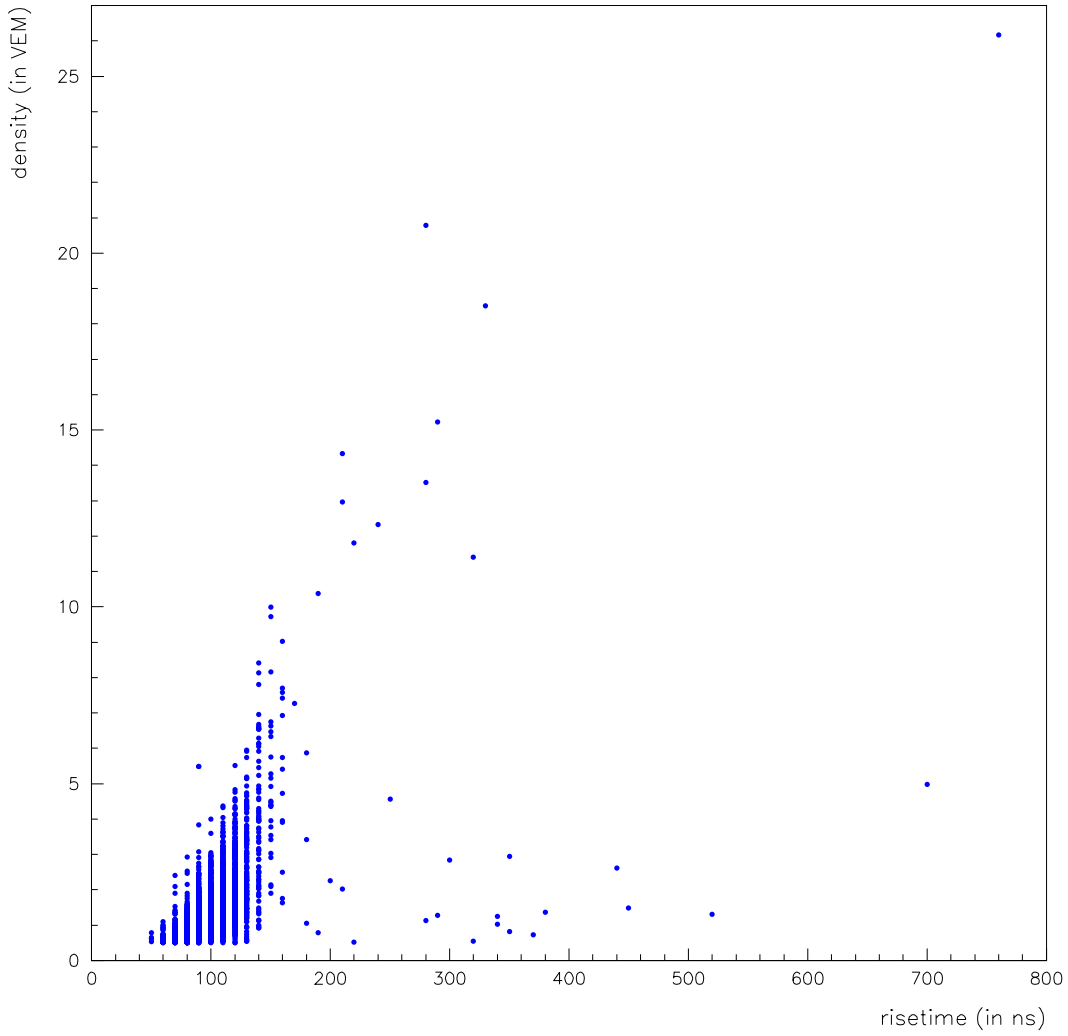

Figure B.1: *Plotted are integrated signals in VEM as function of their rise time* $t_{10\%-90\%}$.

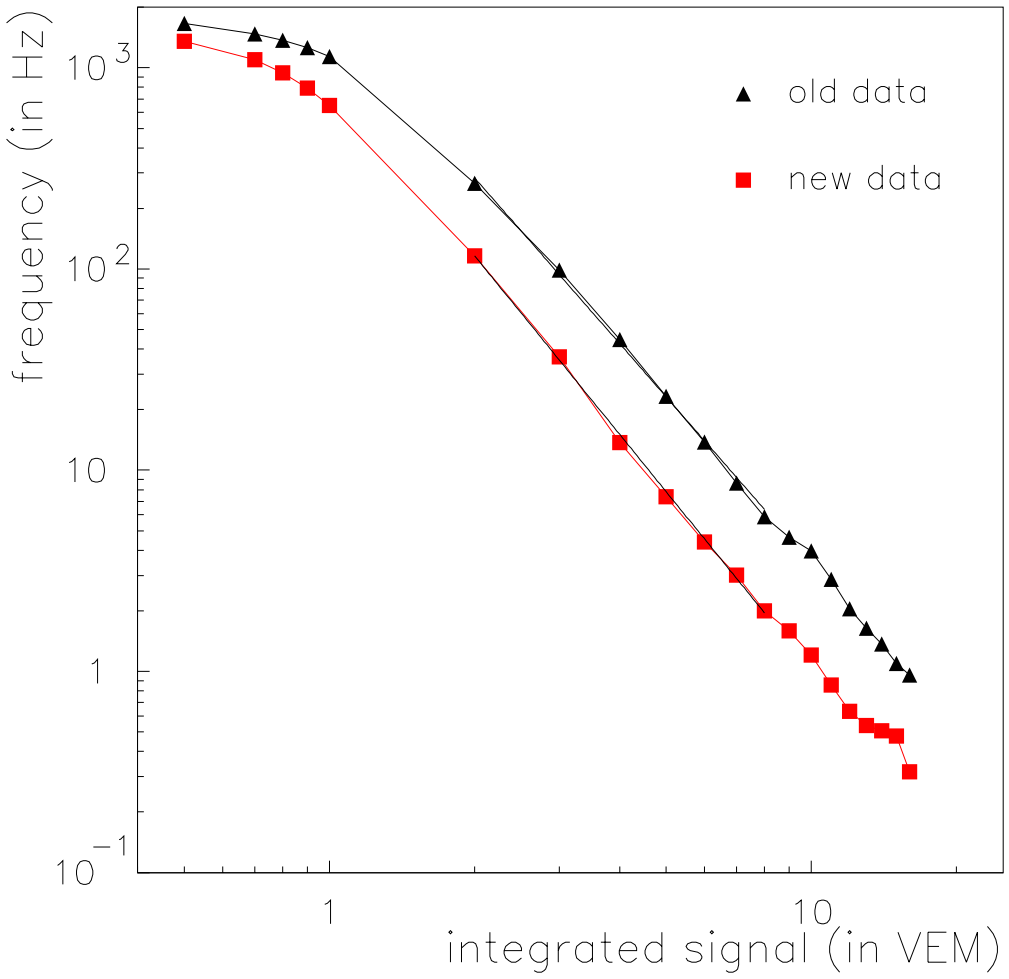

Figure B.2: *Integral frequency spectrum of background events recorded with the first water Cherenkov detector at AGASA. Squares correspond to the data set described here. Triangles originate from an older data set described in [106].*

muons (VEM) as function of the rise time $t_{10\%-90\%}$. From these data an integral pulse charge spectrum has been compiled which is shown in figure B.2. The slopes of the integral spectra, fitted between threshold values of 2 and 8 VEM were found to be -2.74 and -2.95 for the old and new data set respectively.

B.3 Frequency spectrum results

From figure B.2 it can be inferred that a threshold value of about 3.5 VEM is necessary to reduce the accidental event rate to 20 Hz, the required limit at the post level 2 trigger stage.
As the presented results have been derived for an observation level of 920 g/cm^2 the results need to be corrected for the atmospheric depth at the site of the Auger Observatory — 870 g/cm^2. The accidental signals found in randomly recorded FADC traces are mostly due to muons and small air showers. The latter consist, especially at low energies mainly of muons. It is therefore a reasonable approximation to use the attenuation of muons in the atmosphere as a guide to estimate the signal rate at 870 g/cm^2. Based on the atmospheric attenuation curve for muons with energies above 1 GeV ([109] figure 20.3) the event rate is expected to be higher by about 10%. Thus the post level 2 trigger requirement for an event rate of 20 Hz can be fulfilled for a threshold of 4 VEM on signal size if no further constraints are applied.

Bibliography

[1] D.J.Bird et al.
Phys.Rev.Lett. **71** (1993) 3401

[2] N.Hayashida et al.
Phys.Rev.Lett. **73** (1994) 3491

[3] C.D. Anderson
Phys. Rev. **43** (1933) 368

[4] C.D. Anderson and S.H. Neddermeyer
Phys. Rev. **50** (1936) 263

[5] G.P.S. Occialini and C.F. Powell
Nature **159** (1947) 186

[6] The Auger Collaboration
"The Pierre Auger Observatory Design Report", Second Edition, February 1997

[7] M. Nagano et al.
J. Phys. G: Nucl. Phys. **18** (1992) 423

[8] M. Takeda et al.
Phys. Rev. Lett., **81** (1998) 1163

[9] S. Yoshida et al.
Astrop. Phys., **3** (1995) 105 - 123

[10] M.A. Lawrence et al.
J. Phys. G: Nucl. Part. Phys., **17** (1991) 733 - 757

[11] B.N. Afanasiev et al.
Proc. 24th Int. Cosmic Ray Conf. (Rome), **2** (1995) 756

[12] D.J.Bird et al.
Astrophys.J. **424** (1994) 491 - 502

[13] J. Linsley
Phys. Rev. Lett. **10** (1963) 146

[14] A.A. Penzias and R.W. Wilson
Astrophys. J. **142** (1965) 419

[15] K. Greisen
Phys. Rev. Letters **16** (1966) 748

[16] G.T. Zatsepin and V.A. Kuzmin
JETP Letters **4** (1966) 78

[17] J.W. Cronin
Nucl. Phys. B (Proc. Suppl.) **28B** (1992) 213

[18] E. Loh
Proc. of the Tokyo Workshop on Techniques for the Study of EHECRs ed. by M. Nagano (ICRR, Univ. of Tokyo), (1993) 105

[19] M. Al-Seady et al.
Proc. of ICRR Int. Sympos. on "EHECRs: Astrophysics and Future Observatories" ed. by M. Nagano (ICRR, Univ. of Tokyo), (1996) 191

[20] M. Teshima et al.
Nucl. Phys. B (Proc. Suppl.) **28B** (1992) 169

[21] M. Teshima
Proc. of the Tokyo Workshop on Techniques for the Study of EHECRs ed. by M. Nagano (ICRR, Univ. of Tokyo), (1993) 109

[22] N. Chiba et al.
Nucl. Instr. and Meth. A **311** (1992) 338 - 349

[23] H. Ohoka et al.
Nucl. Instr. and Meth. A **385** (1997) 268 - 276

[24] S.C. Lillicrap et al.
Proc. Phys. Soc. **82** (1963) 95

[25] R.M. Tennant
Proc. Phys. Soc. **92** (1967) 622

[26] D.M. Edge et al.
Proc. 15th Int. Cosmic Ray Conf. (Plovdiv), **9** (1977) 137

[27] T.C.Weekes et al.
The Astrophys.J. **342** (1989) 379

[28] Vocanti et al.
Astrop.J. **377** (1991) 467

[29] D.Lewis et al.
Proc. 23rd Int. Cosmic Ray Conf. (Calgary), **1** (1993) 279

[30] A.Konopelko et al.
Astroparticle Phys. **4** (1996) 199

[31] Meintjes et al.
Ap.J. **401** (1992) 325

[32] Meintjes et al.
Ap.J. **434** (1994) 292

[33] Bowden et al.
Astroparticle Phys. **1** (1992) 47

[34] Punch et al.
Nature **358** (1992) 477

[35] G.Mohanty et al.
Proc. 23rd Int. Cosmic Ray Conf. (Calgary), **1** (1993) 440

[36] M.S.Longair
"High Energy Astrophysics", Cambridge Univ. Press (1981)

[37] A.M. Hillas
Ann. Rev. Astron. Astrophys. **22** (1984) 425

[38] C.A. Norman et al.
Astrophys. J. **454** (1995) 60

[39] H. Kang et al.
Astrophys. J. **456** (1996) 422

[40] C.J. Cesarsky et al.
Proc. 23rd Int. Cosmic Ray Conf. (Calgary), **2** (1993) 341

[41] P.L. Biermann et al.
Astrophys. J. **322** (1987) 643

[42] D. Hartmann et al.
Astrophys. J. **464** (1996) 226 - 232

[43] T. Stanev et al.
Phys. Rev. Lett. **75** (1995) 3056

[44] E. Waxman et al.
Astrophys. J. **462** (1996) L59

[45] N. Hayashida et al.
Phys. Rev. Lett. **77** (1996) 1000 - 1003

[46] E. Waxman
Phys. Rev. Lett. **75** (1995) 386

[47] M. Vietri
Astrophys. J. **453** (1995) 883

[48] S. Colgate
Talk at the opening workshop of the Auger Study, Fermilab (January 31, 1995)

[49] M. Milgrom et al.
Astrophys. J. **449** (1995) L37

[50] P. Bhattacharjee and G. Sigl
E-Print astro-ph/9811011 (1998), submitted to Physics Reports

[51] J.W. Cronin
Nucl. Phys. (Proc. Supp.) **28B** (1992) 213

[52] F.A. Aharonian and J.W. Cronin
Phys. Rev. **D50** (1994) 1892

[53] R.W. Clay et al.
Proc. Adelaide Design Workshop on Techniques for the Study of Cosmic Rays above 10^{19} eV (January 1993) 1

[54] M. Hillas
Nature **395** (1998) 15

[55] P. Auger, Raymond Maze, Therese Grivet-Meyer
Academie des Sciences, Seance du 8 juin (1938)

[56] P. Auger et al.
"Comptes rendus", **206** (1938) 1721

[57] P. Auger, Roland Maze
Academie des Sciences, Seance du 18 juillet (1938)

[58] A.M. Hillas
Nuclear Physics B (Proc. Suppl.) **28B** (1992) 67 - 73

[59] T.K. Gaisser
"Cosmic Rays and Particle Physics", Cambridge University Press 1990

[60] N. Hayashida et al.
J. Phys. G: Nucl. Part. Phys **21** (1995) 1101 - 1119

[61] R. Walker and A.A. Watson
J. Phys. G: Nucl. Phys. **7** (1981) 1297 - 1309

[62] R. Walker and A.A. Watson
J. Phys. G: Nucl. Phys. **8** (1982) 1131 - 1140

[63] D. Ravignani et al.
"Cosmic Ray Shower Simulations with MOCCA: Artificial Fluctuations due to Thinning"
Auger project technical note, GAP-96-020* (1996)

[64] D. Ravignani and C. Hojvat
"Fluctuations in the Lateral Distribution from MOCCA Simulations at 10^{-7} Thinning Level"
Auger project technical note, GAP-96-032* (1996)

[65] J.W. Cronin
"Consideration of Fluctuations at Large Distances from the Shower Core"
Auger project technical note, GAP-95-018* (1995)

[66] A.M. Hillas et al.
Proc. 12^{th} Int. Cosmic Ray Conf. (Hobart), **3** (1971) 1001 - 1006
also p. 135

[67] D.J. Bird *et al.*,
Proc. 23^{rd} Int. Cosmic Ray Conf. (Calgary), **2** (1993) 450

[68] T.K. Gaisser & A.M. Hillas
Proc. 15^{th} Int. Cosmic Ray Conf. (Plovdiv), **8** (1977) 353

[69] F. Kakimoto et al.
Nucl. Instr. and Meth. A **372** (1996) 527 - 533

[70] P. Sommers
"Three Eyes with Dual Mirrors"
Auger project technical note, GAP-1996-010* (1996)

[71] P. Sommers
"Trigger Sensitivity with Dual Mirrors"
Auger project technical note, GAP-1996-035* (1996)

[72] A. Cordero, J. Castro, J. Cuautle, et al.
"Proposal for the Optical System of the Fluorescence Detector of the Auger Project"
Auger project technical note, GAP-1997-045* (1997)

[73] G. Matthiae and P. Privetera
"The Schmidt Telescope with Corrector Plate"
Auger project technical note, GAP-1998-039* (1998)

[74] B.R. Dawson, B.E. Fick, K.H. Kampert and P. Sommers
Proc. 25th Int. Cosmic Ray Conf. (Durban), **5** (1997) 377

[75] R.N. Coy et al.
Astrop. Phys., **6** (1997) 263 - 270

[76] A.M. Hillas et al
Acta Physica Academiae Scientarium Hungaricae, Suppl. **3** (1970) 533

[77] D.M. Edge et al.
J. Phys. A: Math., Nucl. Gen., **6** (1973) 1612

[78] N. Sakaki and M. Nagano
Proc. of ICRR Int. Sympos. on "EHECRs: Astrophysics and Future Observatories" ed. by M. Nagano (ICRR, Univ. of Tokyo), (1996) 402

[79] Hamamatsu Technical Data Sheet
"8 inch hemispherical photomultiplier tube R1408" (1985)

[80] T.Kutter et al.
"Self calibration of the water Cherenkov tanks: Experimental results"
Auger project technical note, GAP-1997-025* (1997)

[81] C.L. Pryke
"Instrumentation development and experimental design for a next generation detector of the highest energy cosmic rays"
PhD Thesis, University of Leeds (1996)

[82] GEANT, *"Detector Description and Simulation Tool"*
CERN Program Library Long Writeup W5013 (1993)

[83] R. Smith and K. Baker
App. Optics, **20** (1981) 177

[84] Surface Optics Corporation
Report SOC-R950-001-0195

[85] C. Pryke
Proc. of ICRR Int. Sympos. on "EHECRs: Astrophysics and Future Observatories" ed. by M. Nagano (ICRR, Univ. of Tokyo), (1996) 407

[86] J. Krider and H. Nguyen
"Instructions for using the Photomultiplier Tube Testing Facility"
FNAL Physics Section internal report (1996)

[87] C. Pryke and T. Kutter
"Measurements of R1408 photomultiplier performance"
Auger project technical note, GAP-96-041* (1996)

[88] C. Pryke
Internal note, (1997)

[89] C. Pryke
"Self calibration of the water Cherenkov tanks: Simulation"
Auger project technical note, GAP-1997-026* (1997)

[90] P. Mazur
private communication (1999)

[91] C. Pryke
"Simulations of the Proposed Auger Water Cerenkov Ground Array"
Auger project technical note, GAP-1997-005* (1997)

[92] C. Pryke
"Chemical Composition Studies with a Hybrid Detector"
Auger project technical note, GAP-1997-022* (1997)
(presented at the XXXII Rencontres de Moriond)

[93] H. Dong Phuong
"Shower Simulation Report"
Auger project technical note, GAP-1995-026* (1995)

[94] J.W. Cronin
"Extraction of Muon Information from the Water Tank" Auger project technical note, GAP-1995-015* (1995)

[95] D. Nitz
Oral presentation at the Auger collaboration meeting in Itacuruca, Brazil (1998)

[96] T. Kutter
"Simulation Study of a Muon Detector underneath a Water Cherenkov Prototype Detector at AGASA"
Auger project technical note, GAP-1998-048* (1998)

[97] R.S. Fletcher et al.
Phys. Rev. D, **50** (1994) 5710

[98] J. Engel et al.
Phys. Rev. D, **46** (1992) 5013

[99] J. Linsley
Proc. 15th Int. Cosmic Ray Conf. (Plovdiv), **12** (1977) 56

[100] R.N. Coy et al.
Proc. 17th Int. Cosmic Ray Conf. (Paris), **6** (1981) 43

[101] R.N. Coy
"A Study of the Development of Extensive Air Showers Produced by 10^{17} eV Cosmic Ray Particles"
PhD Thesis, University of Leeds (1984)

[102] G. Cunningham
"The cosmic ray spectrum above 10^{17} eV"
PhD Thesis, University of Leeds (1982)

[103] S. Yoshida et al.
J. Phys. G: Nucl. Part. Phys., **20** (1994) 651 - 664

[104] H.Y. Dai et al.
J. Phys. G: Nucl. Part. Phys., **14** (1988) 793 - 805

[105] M. Takeda, *private communication* (1999)

[106] T.Kutter
"Measurement of the background rate using a water Cherenkov prototype detector at the Akeno Giant Air Shower Array (AGASA)"
Auger project technical note, GAP-1999-008* (1999)

[107] A.A.Watson, presentation at the Auger collaboration meeting in Morelia, Mexico, January 1999

[108] P.Billoir, "*Estimation of the Acceptance of the Auger Ground Detector to Quasi-horizontal Showers Induced Deeply in the Atmosphere*",
GAP 1997-049

[109] The European Physical Journal C, Review of Particle Physics, 1998

* "GAP technical notes" are internal collaboration papers and are published on the web site of the Pierre Auger Collaboration at
(*http://www.auger.org/admin-cgi-bin/woda/gap_notes.pl*)

Acknowledgment

This work has been carried out within the framework of the Auger collaboration and has been supported by the "German Academic Exchange Service" (DAAD) in form of a scholarship in the scope of the "Hochschulsonderprogramm III von Bund und Ländern".
I thank Prof. H. Rebel from the "Institut für Kernphysik" of the "Forschungszentrum Karlsruhe" for his open-mindedness to support my work on research and development for the Auger Project, and for his willingness to represent it as thesis at the University of Heidelberg. I also appreciate his valuable comments during the preparation of this manuscript.
I would like to thank Prof. J.W. Cronin to enable my stay at the Enrico Fermi Institute in Chicago, his advice during the course of this work and the supply of means for parts of this study.
I would like to express my thanks to Prof. M. Nagano for fruitful discussions, being my host in Japan and most importantly for giving us the unique opportunity to place two prototype detectors within the Akeno Giant Air Shower Array (AGASA). This work would not have been possible without the support of the entire AGASA collaboration and their devotion to maintain and operate their observatory. In particular, many thanks to N. Sakaki who took well care of the water Cherenkov prototype detectors.
I greatly appreciate Prof. A. Watson's expert advice on the topic and also would like to thank him for being my host at Leeds. Many thanks also to Dr. K. Gibbs who helped me to improve my written English on several occasions by making valuable remarks and Dr. C. Pryke for useful discussions during the early stages of this work. Furthermore, I would like to mention Prof. G. Schatz for directing me towards Prof. H. Rebel during the initial process of organizing my stay abroad. J. Geddes receives my thanks for proof-reading parts of this manuscript.
Last but not least I would like to thank numerous individuals within and outside of the Auger collaboration for interesting discussions, intellectual stimulation as well as new insights and ideas.